Effects of pore structure on velocity and permeability in carbonate rocks

Dissertation
der Mathematisch-Naturwissenschaftlichen Fakultät
der Eberhard Karls Universität Tübingen
zur Erlangung des Grades eines
Doktors der Naturwissenschaften
(Dr. rer. nat.)

vorgelegt von
Gregor T. Bächle
aus Zell am Harmersbach

Tübingen
2009

Tag der mündlichen Qualifikation: 13 Juli, 2009

Dekan: Prof. Dr. Peter Grathwohl

1. Berichterstatter: Prof. Dr. Thomas Aigner

2. Berichterstatter: Prof. Dr. Gregor P. Eberli

Effects of pore structure on velocity and permeability in carbonate rocks

Dissertation
der Mathematisch-Naturwissenschaftlichen Fakultät
der Eberhard Karls Universität Tübingen
zur Erlangung des Grades eines
Doktors der Naturwissenschaften
(Dr. rer. nat.)

vorgelegt von
Gregor T. Bächle
aus Zell am Harmersbach

Tübingen
2009

Tag der mündlichen Qualifikation: 13 Juli, 2009

Dekan: Prof. Dr. Peter Grathwohl

1. Berichterstatter: Prof. Dr. Thomas Aigner

2. Berichterstatter: Prof. Dr. Gregor P. Eberli

CONTENTS

CHAPTER 1:

QUANTIFYING PORE STRUCTURES OF CARBONATES WITH 2D IMAGE ANALYSIS

CHAPTER 2:

ROLE OF MICRO-POROSITY FOR THE ACOUSTIC BEHAVIOR OF CARBONATES – IMPLICATIONS FOR PERMEABILITY PREDICTION

CHAPTER 3:

PREDICTION OF SONIC VELOCITY FROM THIN SECTIONS

CHAPTER 4:

CHANGES IN DYNAMIC SHEAR MODULI OF CARBONATE ROCKS WITH FLUID SUBSTITUTION

ZUSAMMENFASSUNG

Gesteinsphysikalische Modelle verringern die komplexen Porenstrukturen zu idealisierten Porengeometrien. Gesteinsphysikalische Modelle sind in der Lage Schallgeschwindigkeiten in Gesteinen vorherzusagen, wenn man idealisierte Porengeometrien untern bestimmten Konzentrationen benutzt. Gesteinsphysikalische Modelle können nützlich sein zur analogen, elastischen Darstellung von Karbonatgesteinen. Eine wichtige Herausforderung in der Gesteinphysik ist die Verknüpfung der Modelparameter zur Beschreibung der Porengeometrie idealisierter Poren mit den komplexen Porengeometrien in einem Gestein. Um dieser Herausforderung zu begegnen, habe ich die Schallgeschwindigkeit von Karbonaten mit einer breiten Variation von Porentypen und Gesteinarten gemessen. Desweiteren wird eine quantitative digitale Bildanalyse von Duennschliffen verwendet, um die strukturellen Merkmale der Poren in einer zuverlässige und wiederholbare Weise zu messen. Darüber hinaus zeige ich, wie die Schallgeschwindigkeit mit der Permeabilität in Verbindung gesetzt werden kann, durch die Porosität, Porengröße und Poren-Form. Es wird auch ein empirischen Zusammenhang zwischen gesteinsphysikalischen Parametern und der Mikroporosität hergestellt.

Kapitel 1 umfasst die Auswirkung von Porengeometrien auf die Permeabilität von Gesteinen. Die Porenrundheit in Karbonatgestein, gemessen an Mikroskopbildern der Porenstrukur, hat sich als Indikator der Permeabilität erwiesen, in Bohrkernen Analysen von der Bahama Plattform (Anselmetti et al. 1998). Die Porenrundheit γ, gemessen an Mikroskopbildern von Dünnschliffen, ist auch ein zuverlässiger Parameter zur Vorhersage der Permeabilität in unserem Datensatz von 3 verschiedenen Karbonatfomationen.

In Kapitel 2 wird gezeigt, dass sich vier Parameter zur Karakterisierung der Porenstruktur als relevant erweisen für die Schallgeschwindigkeit Streuung in Bezug auf Porosität. Porosität allein zeigte eine schwache Korrelation (r^2=0,54) mit der Schallgeschwindigkeit. Multiregressionsanalyse unter Nutzung der Porenrundheit, der dominanten Porengröße, dem Quotienten zwischen Durchmesser und Porenfläche, und der Mikroporosität zeigt einen sehr guten Korrelationskoeffizienten (r^2=0,87).

Kapitel 2 und 3 beurteilen die Wirkung von Mikroporen auf die Schallgeschwindigkeit und Permeabilität. Mikroporosität zeigt eine gute Korrelation mit der Schallgeschwindigkeit (r^2=0,83), während die Makroporosität nicht besonders effektiv für die Schallgeschwindigkeitsreduzierung ist. Dies bedeutet, dass mit einer wachsenden Makroporosität, eine zunehmende Abweichung von der „Wyllie's time average“ Schallgeschwindigkeit beobachtet wird. Mikroporosität erweisst sich als eine nützlicher Parameter zur Vorhersage der Schallgeschwindigkeit unter Nutzung von Dünnenschliffen.

Eine meiner Annahmen, in Kapitel 3, zur Modellierung der Schallgeschwindigkeit ist, dass die Mikroporen sich sehr elastisch-nachgiebig verhalten und deshalb im Zusammenhang stehen mit der geringen Schallgeschwindigkeit bei einer gegebenen Porosität. Ich benutzte Mikroporosität als Eingabe Parameter in das „Differentiale Effektive Medium“ (DEM)-Modell. Ich entwickle eine empirische Beziehung zwischen der Mikroporosität und der elastischen Steifheit des Porenraums. Eine Regressionsanalyse zeigt die Beziehung zwischen der Mikroporosität und des Quotienten von Porosität und der Steifheit des Porenraums (r^2=0,88).

Die Gassmann Gleichung (Gassmann, 1951) wird im Allgemeinen verwendet um die Auswirkungen einer Änderungen der Porenflüssigkeit auf die akustische Wellengeschwindigkeit im Gestein vorherzusagen. In Kapitel 4 zeige ich, dass in 66% der Proben eine Vorhersage der gemessenen Schallgeschwindigkeit unter Nutzung der Gassmann Beziehung, nach der Wassersaettigung der Probe, nicht moeglich ist. Die Schermodul Veränderungen korrelieren mit der fehlerhaften Gassmann Vorhersage der Schallgeschwindigkeit der gesättigten Proben. Aufgrund der Veränderungen der Porenfüllung von trockenen zu Wasser gesättigten Poren, nimmt das Schermodul bis zu 2GPa ab und steigt in andere Proben bis zu 3GPa an. Ich zeige, dass „grainstones' mit einem hohen Anteil an Mikroporosität zur Verminderung des Scher-Moduls neigen, mit Wassersättigung.

Die Ergebnisse dieser Dissertation zeigen, dass (a) die Vorhersage der akustischen Eigenschaften wird verbessert wenn die Porosität in Kombination mit Porenparametern einer digitalen Bildanalyse genutzt wird (b) Mikroporosität kann dazu verwendet werden gesteins-physikalische Modelle zu kalibrieren, und (c) elastische Eigenschaften aus gesteinsphysikalischen Modellen bieten eine Verbindung zwischen akustischen Eigenschaften und Permeabilität.

ABSTRACT

Rock physics models are known to reduce complex pores structure into idealized pore geometries. Using idealized pore geometries at a specific concentration, rock physics models, like differential effective medium (DEM) models, are able to predict velocities. Rock physic models can be useful as elastic analogues of carbonate rocks. One important challenge in carbonate rock physics is to link model parameters describing the idealized pore geometry to observable pore geometry in the real rocks. To address this challenge, I have measured ultrasonic velocity on carbonate rocks with a wide variation of pore and rock types. Quantitative digital image analysis (DIA) is used to extract the pore structural characteristics in a reliable and repeatable way. Further, I show how the acoustic velocity is linked to permeability by porosity, pore size and pore shape which affects both, permeability and acoustic velocity. Furthermore, an empirical link between rock physics models and the micro-porosity is established.

Chapter 1 covers the effect of pore geometry on permeability. The pore circularity in carbonate rocks, derived from optical light micrographs, has been shown to be a permeability indicator in Bahamas carbonate platform core and log analysis (Anselmetti et al. 1998). The pore shape factor γ is found to be a reliable parameter to improve the permeability prediction from optical light microscopy images.

Chapter 2: Four pore structure parameters derived from thin section analysis proved to be relevant for velocity scatter in relation to porosity. Porosity alone showed a weak correlation (r^2=0.54) to velocity. Multiple regression analysis using pore shape parameter γ, dominant pore size and ratio of perimeter over area of the pores, and micro-porosity shows in a very good correlation coefficient (r^2=0.87).

Chapter 2 & 3 assess the effect of micro-porosity on acoustic velocity and permeability. Micro-porosity shows a good correlation with velocity (r^2=0.83), whereas macro-porosity is apparently “ineffective” to velocity. This signifies that with an increasing amount of macro-porosity, we observe an increasing deviation from the Wyllie’s time average velocity. Micro-porosity proved to be a useful parameter to predict velocity from thin sections.

In Chapter 3, one of our assumptions in modeling sonic velocity is that the micro-porosity is related to rocks of relative slow acoustic velocity at a given porosity and pores which behave compliant. I use micro-porosity as an input parameter in the differential effective medium (DEM) model. I develop an empirical relationship that enables a link between micro-porosity and the pore space stiffness. A regression analysis shows a relationship between micro-porosity and the ratio of porosity over the pore space stiffness (r^2=0.88).

The Gassmann equation (Gassmann, 1951) is commonly used to predict the effect of changes in the fluid type on the acoustic property of a rock. In chapter 4, I show that 66% of the samples show a misfit between measured and Gassmann predicted saturated velocity. Shear moduli changes correlate with the Gassmann-prediction misfit of the saturated P-wave velocity. The shear modulus decreases up to 2 GPa and increases up to 3 GPa due to changes in fluid type from dry to fully water-saturated conditions. I show that grainstones with a high amount of microporosity are prone to show shear moduli decrease with water saturation.

The findings of this dissertation imply that (a) using porosity in combination with digital image analysis (DIA) parameters improves the prediction of acoustic properties, (b) micro-porosity can be used to calibrate a DEM model, and (c) elastic attributes derived from rock physics models provide a link between acoustic properties and permeability.

NOMENCLATUR

Permeability	Standard Klinkenberg corrected core permeability (mD)
Probe permeability	Minipermeameter permeability (mD)
Vp	Compressional P-wave velocity (m/s)
Vp_{Min}	Mineral compressional wave velocity (m/s)
Vp_{Fluid}	Fluid compressional wave velocity (m/s)
Vp_{Gass}	Gassmann-predicted P-wave velocity (m/s)
Vp_{wet}	P-wave velocity measured under water saturated conditions (m/s)
Vp_{dry}	P-wave velocity measured under dry conditions (m/s)
RMSE	Root mean square error (m/s)
Vs	Shear wave velocity (m/s)
Vs_{wet}; Vs_{w}	S-wave velocity measured under water saturated conditions(m/s)
Vs_{dry}; Vs_{d}	S-wave velocity measured under dry conditions (m/s)
K	Bulk modulus (GPa)
K_{Min}; K_g	Mineral bulk modulus (GPa)
$K_{Ø,}$ K_{por}	Pore space stiffness (GPa)
K_f	Fluid modulus (GPa)
K_{Gass}	Gassmann-predicted bulk modulus (GPa)
Knorm	Bulk modulus normalized by the mineral modulus (-)
Kmeasured	Measured bulk modulus (GPa)
Kmodeled	Predicted bulk modulus using a rock physics model (GPa)
µmeasured	Measured shear modulus (GPa)
µmodeled	Predicted shear modulus using a rock physics model (GPa)
μ	Shear modulus (GPa)
μ_d; μ_{dry}	Shear modulus (GPa) measured under dry conditions
μ_w; μ_{wet}	Shear modulus (GPa) measured under water-saturated conditions
γ_{por}	Pore shape factor of a single pore (-)
γ	Pore shape factor of the entire pore population on a thin section (-)
ρ	Bulk density (g/cm^3)
ρ_{Grain}	Mineral density (g/cm^3)
ρ_{Fluid}	Fluid density (g/cm^3)
microporosity	Microporosity dominant pore type (qualitative determined)
micro-porosity	Fraction of micro-porosity derived from digital image analysis (%)
macro-porosity	Fraction of macro-porosity derived from digital image analysis (%)
porosity; Ø	Effective helium porosity, measured on core plug (%)
P	Pore perimeter (µm)
A	Pore area (µm^2)
π	Phi = 3.14159
Pressure	Differential pressure between confining and pore pressure (MPa)
OLM	Optical light microscopy
ESEM	Environmental scanning electron microscopy
DEM	Differential effective medium
STDDEV	Standard deviation

AR; α	Aspect ratio of pores
ARmicro	Aspect ratio of micropores
ARmacro	Aspect ratio of macropores
XRD	X-ray diffraction
p	Geometrical coefficient of the bulk modulus
q	Geometrical coefficient of the shear modulus
υ	Poisson ratio (-)
PoA	Perimeter over area (μm^{-1})
DOMsize	Dominant pore size (μm^2)

Rock types

G	Grainstone	P	Packstone	W	Wackestone
M	Mudstone	FL	Floatstone	Rdol	Dolostone (recrystallized)

Pore types

IP	Inter-particle porosity	IX	Inter-crystalline porosity
MO	Moldic porosity	VUG	Vuggy porosity
WP	Intra-particle porosity	WF	Intra-frame porosity
μG	Micro-moldic porosity		

ACKNOWLEDGMENT

I am truly indebted and grateful to my advisor, Gregor Eberli, to take me on as one of his PhD students. I am most thankful for his ability to teach me the spirit of giving a presentation “short and sweet” and for his help in distilling my dissertation to the most important contributions. I would also like to thank my advisor at the University of Tuebingen, Tom Aigner, for his guidance and support. This dissertation would not exist unless Paul Glover and Lutz Riepe spurred early on my interest in a rock’s microstructure and it’s petrophysical properties while I was studying at the University of Aberdeen.

I would like to acknowledge the financial support of my research by the DAAD, the financial support by the CSL Industrial Associates and the project funding provided by Jose-Luis Massaferro/Shell. The later project lead to innumerable discussions with Jose-Luis, Gregor Eberli, Ralf Weger and Y-F Sun which I am all grateful for forging valuable intellectual dissent to stimulate my research. Equally, I would like to thank Austin Boyd/Schlumberger, Ivar Brevik/Statoil and Mark Knackstedt/ANU for their interest and inspiring discussions as a result of my early experimental results. I am obliged to many colleagues who shared the sometimes painful, sometimes fun periods during our days as RSMAS students: Nick, Dave, Matt, Kelley, Miriam, Tiina, Brigitte, Thiago and Ashwanth. Ursula Bausenwein is thanked for her support during the early days of my PhD. I would like to thank especially Layaan Al-Kharusi for her support on/off work at all times, and for helping me in the lab for chapter four. Karl Coyner is thanked for his remote assistance especially when the system frequently broke down during the course of usage. I owe sincere and earnest thankfulness to Arnout Colpaert for the stimulating discussions and his help in providing code for the DEM analysis in chapter three.

Finally, I would like to thank my parents and family for their financial and moral support of this never ending endeavor. Last but not least, I would like to thank my wife Grace for her love, her patience and her trust that there exists life after finishing this PhD.

INTRODUCTION

Quantitative seismic interpretation is an important technology in the hydrocarbon industry to predict reservoir properties in the subsurface. Fundamentals of rock physics are used to transform seismic derived acoustic attributes to reservoir properties, for example, the pore volume, the pore fluids type or the lithology. An overview of several empirical and theoretical rock physics models are given by Mavko et al. (1998). In sandstones, velocity can be predicted by using rock physics models which incorporate factors, such as, porosity, shale volume, fluid types or mineralogy (Mavko et al., 1998). Carbonate rocks also exhibit a wide range in mineralogy, ranging from calcite, dolomite, aragonite to evaporate minerals (anhydrite and gypsum) with a minor percentage of organic material, clay and quartz. Elastic properties in carbonate rocks, however, are not primarily affected by the mineralogy but by the mineral's propensity to diagenetic alterations of the depositional rock texture and pore structure. The nature of carbonate pore system, with complicated pore shapes and pore sizes ranging from micro to macro scale, is formed by cementation, dissolution and/or recrystallization processes. These modifications cause very dynamic cross-property relationships, e.g. complex velocity-porosity or porosity-permeability transforms (Eberli et al. 2003). In addition to the diagenetic alterations, the depositional environment can lead to lateral rapid changes in porosity and pore types, which can as well affect the physical properties of carbonates. One consequence is that applying known rock physics models to predict carbonate reservoir properties, like pore fluid and porosity, still proves to be a challenge in reservoir studies and is often prone to failure.

Effects of carbonate pore types on sonic velocity and permeability

The importance of pore texture on the physical properties in carbonates was first realized by Archie (1952) and Wyllie et al. (1956). Archie (1952) first classified carbonate rocks by their pore size to get an approximation on the permeability. Porosity is subdivided into visible macro-porosity and matrix micro-porosity. The visible macro-porosity is divided in pore size classes; pore size is increasing from class A with no visible macro-porosity up to class D with pore sizes larger than cutting size (Archie, 1952). Further, the matrix microporosity is divided as being in between sucrosic crystals (>50 µm crystals), in chalky matrix (<50 µm crystals) or in compact matrix. Wyllie et al. (1956) proposed the Wyllie's time average equation, based on a heuristic approach to explain experimental sandstone measurements. Wyllie et al. (1956) derive the total travel time of a wave in a rock composed of pore fluid and rock frame to be the sum of the travel times in those two components. Wyllie et al. (1958) noticed that velocity in vuggy carbonates is higher than predicted by the porosity using Wyllie's time average equation. They proposed that the velocity in a vuggy rock "depends upon the velocity of the rock matrix material with its attendant intercrystalline porosity". Schlumberger (1974) introduced the term "primary porosity" to describe porosity calculated by using Wyllie's time average equation and the term "secondary porosity" which is derived by subtracting the "primary porosity" from the total measured porosity. It is assumed that the measured porosity deviates from the Wyllie times average "primary porosity" as a result of the first P-wave arrival bypassing the "secondary porosity" (Schlumberger, 1974). Schlumberger (1974), Wyllie et al. (1958) and Archie (1952), however, do not provide a genetic classification indicating the depositional environment of the carbonates or their diagenetic history.

Choquette and Pray (1970) established a classification of carbonate porosity based on the genesis of the pore space. It aims at the understanding of the evolution of the pore system. They subdivide porosity into three groups: fabric selective, non-fabric selective and porosity which can be fabric selective or not (Fig. 1). Fabric selective porosity means pore space between original depositional skeletal and non-skeletal grains, or fragments or crystals or cements. Further, fabric selective porosity is pore space which outlines are reminiscent of dissolved fragments or grains. Fabric selective porosity is interparticle, intraparticle, intercrystaline, moldic, fenestral, shelter, and growth framework porosity. Fabric non-selective pore types are fracture, channel, vuggy, and cavern porosity.

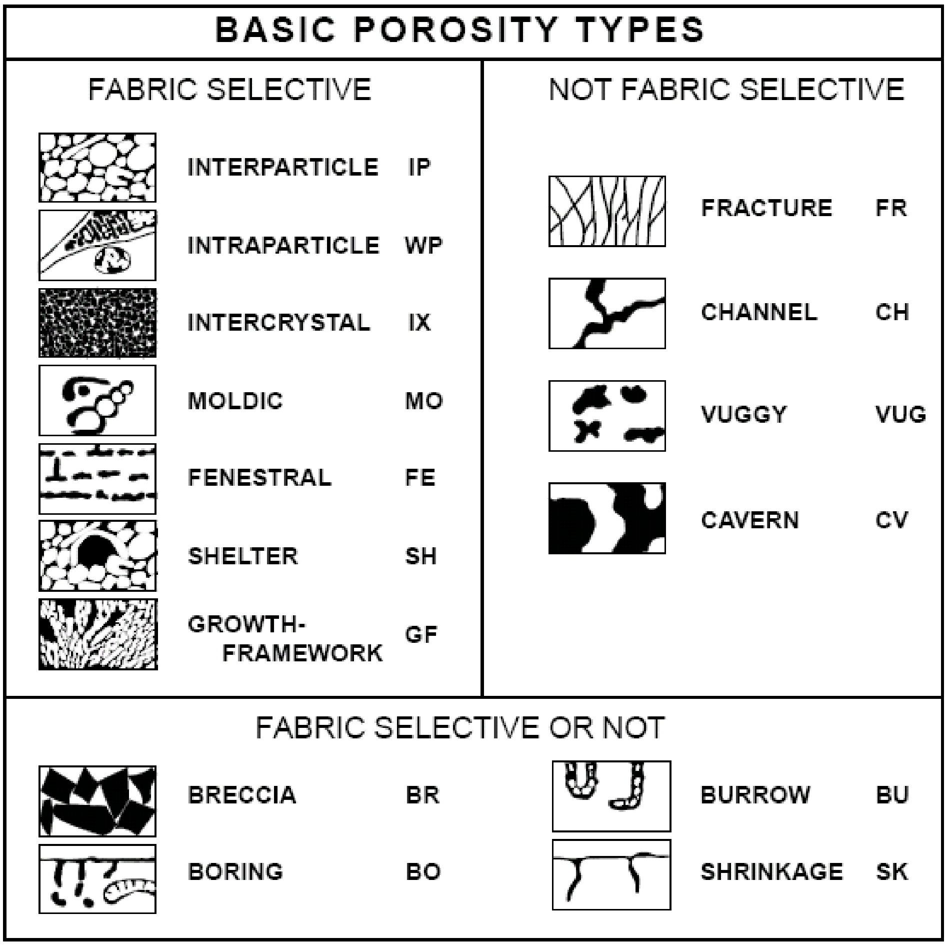

Fig. 1: Pore type classification in carbonate rocks based on fabric selectivity (after Choquette and Pray, 1970)

Lucia (1983) introduced a qualitative carbonate pore type classification which is based on the present day pore size and pore connectivity and it’s effect on the petrophysical properties. For example, moldic and interparticle porosity fall both in the same fabric selective pore classification after Choquette and Pray’s (1970), but they show very different porosity-permeability trends (Lucia, 1983). Lucia (1983) subdivided porosity into touching vug porosity, separate vug porosity and interparticle pore space. All three groups have differences in the quality of connected pore volume. As a result, all three groups show distinct different porosity-permeability relationships.

In the case of porosity which is solely made up of interparticle pore space, Lucia (1993) showed that the grain size distribution has a dominant effect on the interparticle porosity – permeability relationship. Fine grained carbonates (<20 µm) with mud and crystal size controlling the small pore size distribution, display the lowest permeability at any given porosity. Grain dominated carbonates in which mud and grain size controls the pore size (20>100 μm) and subsequently coarse grained carbonates (>100 μm) have higher permeability at any given porosity.

The importance of porosity, pore type, pore shape and the pore size for acoustic velocity is confirmed by experimental data using ultrasonic measurements under controlled laboratory conditions (Wang, 1997; Anselmetti and Eberli, 1993; Marion and Jizba, 1997). An overview of the dominant factors controlling elastic properties in carbonate rocks is given by Eberli et al. (2003). Anselmetti and Eberli (1993) established the importance of dominant pore types when relating the porosity to the P-wave velocity in carbonate rocks. A difference in velocity of over 2500 m/s at the same porosity has been attributed to changes in pore type in carbonate rocks (Eberli et al., 2003). Anselmetti and Eberli (1997) also described for the first time how the different diagenetic processes affect the acoustic velocity in carbonates by process-specific velocity-porosity evolutionary paths. Anselmetti and Eberli (1993) measured ultrasonic velocity on core plugs from two Great Bahama Bank drill sites (Unda and Clino) and on outcrop samples from the Maiella carbonate platform (Italy). They classified the samples into five dominant pore types: (1) interparticle and intercrystalline porosity, (2) microporosity, (3) moldic porosity, (4) intraframe porosity and (5) densely cemented carbonates. Each pore type has a distinct effect on the velocity due to the different shape and size of the pores which affect their relationship with the rock frame (Anselmetti and Eberli, 1993):

Intrafossil porosity is porosity embedded in a biogenetic grown framework, e.g. a coralline rock. These framestones display a positive departure from the exponential best fit regression curve in a velocity-porosity plot (Fig. 2). **Interparticle and intercrystalline porosity** is the pore space between grains and between crystals. In this grain dominated texture, there is no or only small amounts of cement or matrix. This pore type is characterized by a negative deviation from the best fit regression curve in a velocity-porosity plot (Fig. 2). **Microporosity** is a pore type defined by pore size and image resolution. Microporosity can not be resolved using an optical microscope and by definition, microporosity is therefore smaller than pores of 10-20 μm in diameter. This pore type is also characterized by a negative departure from the best fit regression curve in a velocity-porosity plot (Fig. 2). Pore size has also a strong relationship to permeability in carbonates; as pore size is reduced, permeability is also reduced (Lucia, 1999). **Moldic porosity** develops by dissolution of grains which have mineralogical meta-stable grains, e.g. aragonite. The rock frame is consisting of cement, micritic matrix or rims. Carbonates with coarse moldic pores show a strong positive departure from the best fit regression curve in a velocity-porosity plot, whereas samples with fine moldic pores are relatively slow and plot close to the best fit curve in Figure 2. Such separate-vug pore systems, in which the vugs are connected through the matrix, often show distinct different porosity-permeability relationship compared to rocks dominated by interparticle porosity (Lucia, 1999; Melim et al., 2001). **Densely cemented** carbonates show an intense cementation of the pore-space leaving less porosity than 10%. An understanding of the specific effects of pore types on P-wave velocity has the potential to improve velocity-porosity transform and the prediction of porosity. Further, quantification of the velocity scatter at a given porosity in relation to a reference curve in the velocity-porosity space, has shown to be useful to predict permeability trends (Anselmetti and Eberli, 1999).

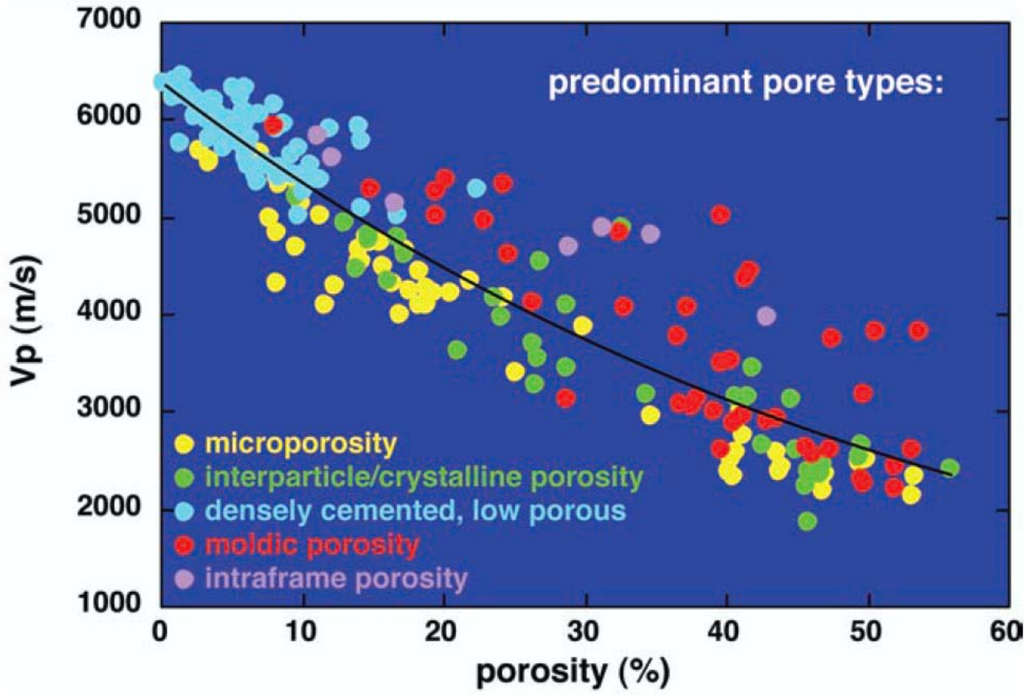

Fig. 2: P-wave velocity versus porosity plot of various carbonate samples. An exponential best fit curve through the data for reference shows scatter of velocity at any given porosity. Samples of specific pore type cluster below and above the reference line (after Anselmetti and Eberli, 1993).

Quantification of carbonate pore structure

Quantitative image analysis on 2D images is a well established method. Many authors have focused on finding relationships between the parameterized pore structure and reservoir rock properties, e.g. permeability (Ehrlich et al., 1984; Katz and Thompson 1985). There exist, however, only a few studies in carbonate rocks which provide quantitative parameters to describe the pore structure, the pore geometry and the pore size distribution (Anselmetti et al., 1998; Movers and Budd, 1996; Etris et al., 1988; Ehrlich et al., 1991 and Ferm et al., 1993). Several studies found that a quantification of the shape of macro-pores (pore perimeter over area ratio) using digital image analysis improves the understanding of variations in permeability and/or velocity at given porosity in carbonates (Anselmetti et al., 1998; Weger et al., 2004; Baechle et al., 2004). The authors emphasize the importance of using digital image analysis as a method of characterizing pore geometry in a repeatable, objective and quantitative manner.

The importance of pore shape for acoustic velocity is recognized and well established in various theoretical rock physics models (Eshelby, 1957; Berryman, 1980; Zimmerman, 1986, Mukerji et al., 1995; Kuster and Toksoz, 1974; Sun 2004). All effective medium models (Berryman, 1980; Kuster and Toksoz, 1974) are physically realizable, which means that the velocity predictions are always within the Hashin-Shtrikman bounds. The Hashin-Shrikman bounds are the upper and lower limit of velocity at a given porosity, mineral composition and fluid saturation. The models are useful as elastic analogues to describe the elastic behavior of materials with specific pore structures (Berge et al., 1995). For example, the self-consistent theory (Berryman, 1980) provides a good prediction of the elastic properties of granular and high porosity rocks (Berge et al., 1995). In contrast, the differential effective medium models predict the elastic properties of glass foams and oceanic basalts (Berge, 1993). Ellipsoidal inclusion models are successfully used as an elastic analogue for elastic experimental data of carbonate rocks (Brie et al., 1985; Kumar and Han, 2005; Rossebø et al., 2005; Saleh and Castagna, 2004). Interpretation of carbonate pore type and pore shape from modeling by use of ellipsoidal inclusion models, however, are characteristically suffering from two main hurdles: (a) an extreme idealizations and reductions of variability in the pore shape, (b) many assumptions about the manner in which the pores elastically interact (Mavko et al., 1998).

Apart from ultrasonic local flow phenomena and attenuation, there is no direct theoretical link between acoustic velocity and permeability of the rock. The large scatter of permeability and velocity at a given porosity increases the uncertainty in the prediction of physical properties. On the other hand, the lack of correlation with porosity and the resulting scatter of permeability and velocity at given porosity can not only be a curse, but also a blessing. If the cause for the scatter can be determined, the gained knowledge can lead to improved predictions. We know that porosity, pore type, pore size and pore geometry are the dominant factors affecting both permeability and velocity (Archie, 1952; Lucia, 1993; Anselmetti und Eberli, 1993; Wang et al., 1991). Furthermore, Anselmetti and Eberli (1999) established a semi-quantitative relationship between velocity and permeability. Their approach is based on the "velocity deviation", which quantifies the effect of the pore type on the acoustic velocity in reference to the Wyllie times average velocity at a given porosity. Anselmetti and Eberli (1999) successfully applied their method to predict permeability trends at well log scale.

This dissertation tackles the challenge to find a relationship between quantitative pore structure parameters, porosity and their effects on velocity at ultrasonic frequencies in core plugs. I investigate how the quantification of the scatter in velocity-porosity space can be used to understand the relationship between porosity and permeability. Further, I show how to calibrate theoretical rock physics models with quantitative image pore structure parameter. Finally, since the rock physics models are proposed to be elastic analogues to the effects of pore types on the elastic properties of a carbonate rock, I use rock physics model parameters to link acoustic velocity and reservoir properties (e.g. porosity and permeability). For these tasks, I measured 250+ core plugs and thin sections and input all measured data into a comprehensive rock physics database composed of: (a) acoustic properties (Vp, Vs, density) measured under controlled pressure and saturation conditions, (b) quantitative measurements of the percentage of minerals, (c) a qualitative description of the carbonate rock and pore type, and (d) quantitative digital image analysis parameters which describe the pore structure, the pore size and pore shape.

HYPOTHESIS

The fundamental working hypothesis of this dissertation is that porosity and pore structure of carbonate rocks do affect acoustic velocities as well as permeability. A second important hypothesis of this dissertation is that the scatter in an acoustic velocity-porosity transform can be related to variations in permeability-porosity transform, since the combination of porosity and pore structure affects both acoustic and fluid flow properties.

In order to test these hypotheses, I verify several other related hypotheses: (a) The quantitative digital image analysis (DIA) parameters describing the pore structure relate to data scatter often observed in the velocity-porosity space, as well as, to the data scatter in the permeability-porosity space. (b) The acoustic parameters derived from rock physics models describing the elastic stiffness variation relate to DIA parameters which describe the pore structure. (c) The velocity of carbonate rocks saturated with different fluid types can be predicted using Gassmann's theory (Gassmann, 1951).

APPROACH

In order to test the main hypotheses, I subdivide the thesis into four chapters. In the following, I describe the specific objectives and approaches for each chapter:

Chapter 1

The objectives are to assess whether the pore shape factor γ as defined by Anselmetti et al. (1998) can be used to predict permeability in reservoir rocks. Another objective is to test the sensitivity of the pore shape factor γ as a function of resolution and to evaluate to which degree a thin section image is statistically representative of the whole core plug.

Approach: I calculate γ on thin section images from samples of known permeability and porosity and across a wide range of carbonate rock and pore types. I use three different techniques to image the pore population on which γ is calculated: environmental scatter electron microscopy (ESEM), optical light microscopy (OLM) and computer tomography scans (CT-scans). The spatial variability of the pore shape factor γ within the core samples is tested by analyzing OLM images of orthogonal orientated thin section orientations and 2D sections of a CT-scan at 3 different spatial orientations.

Chapter 2

The objectives are to determine digital image analysis parameters that characterize the pore structure, which affect velocity variations, as well as, permeability variation at a given porosity. Further, I provide an empirical link between micro-porosity and a rock physics model parameter. Finally, I quantify the effects of pore structure on permeability and ultrasonic velocity in carbonate rocks using a rock physics model.

Approach: I measure ultrasonic velocity, permeability and porosity of samples across a wide range of carbonate rock and pore types. Then, I use thin sections digital image analysis (DIA) parameters of macro-pores and micro-pores to characterize the pore texture, and cut-off values for permeability. I develop a workflow to provide a quantitative link between DIA parameter derived from thin section analysis and a rock physics model parameter, which is derived from elastic properties of the rock.

Chapter 3

The objectives are to assess the feasibility of predicting velocity from thin section observations of the sample’s pore structure. Further, I determine whether a dual porosity differential effective medium model can be used as an elastic analogue to predict the effects of pore structure on the acoustic properties of carbonates.

Approach: On binarized thin section images, I measure the percentage of macro-porosity and calculate the percentage of micro-porosity as input parameter for a dual-porosity differential effective medium model (DEM). Based on the empirical data collected, I assume that micro-pores are elastically compliant, whereas, macro-pores are stiff. The modeling results are compared to the sonic P-wave and S-wave velocity measurement of the core plug represented by the thin section.

Chapter 4

The objective is to assess the effects of pressure and saturation on sonic P-wave and S-wave velocity. Further, I assess the feasibility of predicting the change in acoustic velocity caused by pore fluid changes, from dry conditions to fully water saturated conditions. Finally, I explore the possibility to explain potential velocity prediction misfits by observing changes in the dominant pore type of the samples.

Approach: I compare the measured sonic velocity under saturated and dry conditions with theoretical velocity predictions using Gassmann's theory (Gassmann, 1951). The samples are initially measured under dry conditions and at differential pressures from 2MPa up to 80MPa. In the second run, the samples are measured under fully water-saturated conditions. On the cut-off thin sections, the rock and pore types are qualitatively described.

Chapter 1

QUANTIFYING PORE STRUCTURES OF CARBONATES WITH 2D IMAGE ANALYSIS

Abstract

I quantify the pore structure of carbonate rocks, using digital image analysis of thin section images acquired with an optical light microscope (OLM) and environmental scanning electron microscope (ESEM). Prior to digital image analysis, the image is binarized by segmenting the macro-porosity from the area of grains, cement and micro-porosity. I evaluate the best workflow to measure the shape of the macro-pores and its implication for improved permeability prediction. This process requires to evaluate the sensitivity of the macro-pore shape analysis as a function of the image resolution and of different techniques used for image acquisition (OLM, ESEM). Further, I assess the variability of the shape of macro-pores as a function of image orientation and location using OLM images and computer tomography scans. The results are threefold:

(a) The macro-pore shape calculated by the combination of macro-pore perimeter and macro-pore area is strongly affected by the image resolution and the pore population imaged, which in turn is linked to the image magnification. Smaller macro-pores show a higher degree of circularity than larger macro-pores. (b) The shape of macro-pores is generally a reliable parameter in 2D and 3-D space, but areas with higher heterogeneity are reflected in more irregular macro-pore shapes. (c) The permeability is mainly controlled by the macro-pore shape, in carbonates with higher permeability (>1mD). Macro-pore shapes of high permeability carbonates display a low degree of circularity. Shapes of the macro-pore population measured on OLM images show the best correlation with permeability.

In summary: 1) The variation of the shape of macro-pores within a core plug is small. 2) The knowledge of the shape of macro-pores, derived from quantitative image analysis of thin sections, reduces permeability uncertainty compared to the standard porosity-permeability correlation.

Introduction

In sandstones, simple exponential relationships exist between porosity and permeability (Nelson, 1994). In contrast, carbonate rocks often show a lack of correlation between porosity and permeability (Lucia, 1995; Lønøy, 2006). The mixed bio-physical origin of carbonates as well as their high potential of diagenetic alteration (dissolution, recrystallization and cementation of grains) causes complex rock textures and pore geometries in carbonate rocks. These complex pore geometries are one of the main reasons for data scatter in the porosity-permeability space (Eberli et al., 2003).

Carbonate pore space is traditionally classified into pore types based on their genesis (Choquette and Pray, 1970). For example, fenestral pores can be similar in size and shape to channel pores, but fenestral porosity is fabric selective whereas channel porosity is a non-fabric selective porosity. This established and widely used carbonate pore classification scheme for geologists is intended for understanding the origin and evolution of the pore system.

In contrast, petrophysicists are more interested in the size and shape of pores, which is important for fluid flow. Qualitative classification schemes of pore and rock types are used to capture the effect of pore structure on permeability (Archie, 1952; Lucia, 1983; Lønøy, 2006). One of the earliest petrophysical carbonate pore structure classification is based on pore sizes alone (Archie, 1952). Lucia (1983) classified the carbonate pore space into three main groups: interparticle porosity, touching vug porosity and separate vug porosity. Separate vug porosity, typically moldic or intraparticle porosity, is thought to increase the porosity but not the permeability of the rock (Lucia, 1983). Lucia (1995) separated interparticle porosity into three different classes based on grain size, with two end member pore networks: (a) pore networks in which grain size controls the connected porosity and (b) textures in which mudsize controls the pore network effective for fluid flow. Lucia's petrophysical classes show increasing permeability with increasing grain size, at a given porosity interval. Enos and Sawatsky (1981) have shown a similar relationship between depositional texture, grain size and permeability in carbonate sediments. Fine grained sediments whose depositional texture corresponds to wackestones show lowest permeabilities (0.6 mD to 1.37 mD) whereas mud-free sediments (associated with grainstone texture) exhibit high permeabilities (15.8 D to 56.6 D). Melim et al. (2001)

related traditional pore types and the associated diagenetic processes to the porosity-permeability space. Hereby, intercrystalline porosity showed the highest permeability, moldic porosity the second highest and intergranular porosity the lowest permeability.

Quantitative classification schemes of carbonate pore types are rare in literature. However, pixel resolution of digital image acquiring techniques have massively improved over the last decade, allowing the acquisition of very low magnification images at high pixel resolution with OLM. For a high pixel resolution of 5µm/pixel the maximum field of view jumped from mm-scale to cm-scale over the last decade. Simple classification of pore space and grain space have been carried out by converting true color image into an indexed image and selecting proper indices for pore and grain/matrix space manually (Keehm, 2003; Van der Berg et al., 2002; Anselmetti et al., 1998) or thresholding RGB and/or HSV grey level bands (Fens, 2000; Ehrlich et al., 1991; Cabtree et al., 1984). The problem of characterizing microporosity has been tackled by combining measurements of different scales (Cerepi et al., 2002; Anselmetti et al., 1998).

One of the goals is to access the quantitative relationships between pore shape and connectivity in non-oomoldic reservoir rocks based on images acquired with optical light microscope, scatter electron microscopy and computer tomography scans. I also examine the variability of the pore shape at different scales and orientations.

Method

Physical properties

The porosity is measured on 52 plugs in a helium picnometer. The Klinkenberg corrected permeability is measured with a standard permeameter at TerraTek, under 3 MPa confining pressure.

On a sub-dataset of 31 samples, a probe permeameter is used to obtain point permeability readings. The probe permeameter was provided by the Exxon Production Research Company, it consists of a 12.7 mm outer diameter and a 6.35 inner diameter probe with a flat neoprene washer-tip seal. The instrument produces a constant nitrogen injection flow rate over a range of 0.2 to 2000 mD. A maximum of seven spot measurements per sample along a diagonal line across the plug end surfaces have been measured (Fig. 1). Probe permeability measurements are ideal to assess small scale heterogeneities and relate them to pore structure heterogeneity (Aplin and Sapru, 2001).

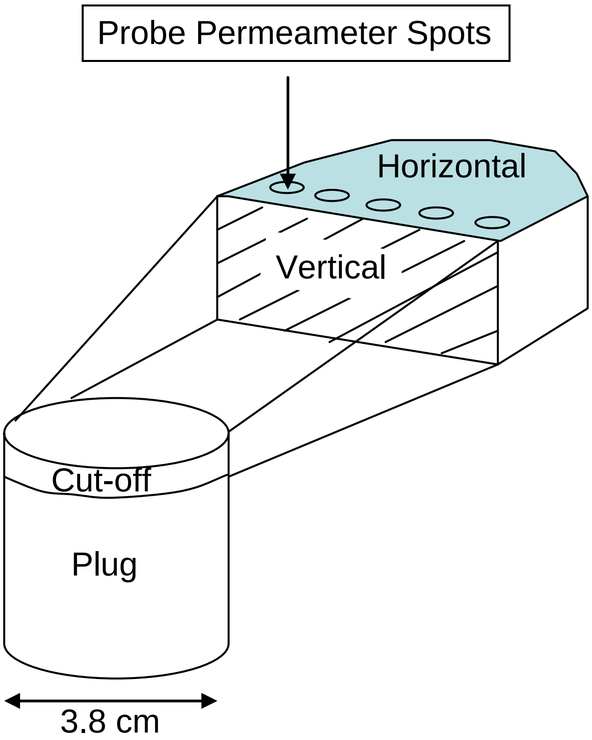

Fig. 1: Sketch showing thin section preparation and mini-perm measurement points

Qualitative pore type classification

If the macro-porosity is the dominant porosity, then I classify the pore type after Choquette and Pray (1970). On the other hand, if the qualitatively characterized microporosity is the dominant porosity, then I classify the pore type as "microporosity".

Quantitative digital image analysis methodology

Quantitative image analysis is an objective procedure to capture the wide range of pore structure variations. Quantitative image analysis of the pore structure in relation to permeability is an established method in sandstones. High resolution, digital images of thin sections acquired with scanning electron microscopy (SEM) are frequently used (Schlueter et al., 1997; Solymar et al., 1999; Blair et al., 1996; Fens, 2000; Aharonov, 1997; Ioannidis et al., 1996; Cerepi, 2002; Anguy et al., 1998).

Fewer studies exist in using quantitative image analysis to characterize the pore structure-permeability relationship in carbonates. All of them incorporated digital images from optical light microscopy (OLM) images at various field of views:

- 0.23 mm^2 x 25 images (Movers and Budd, 1996),
- 3 mm^2 x 3 images (Anselmetti et al., 1998),
- 5 mm^2 x 12 images (Etris et al., 1988),
- 0.25-1 mm^2 x 15-30 images (Ehrlich et. al., 1991) and
- 1 mm^2 of a single image (Ferm et al., 1993).

Anselmetti et al. (1998) showed that “permeability is mainly controlled by the macro-pore shape, which controls the connectivity of the macro-pores, and by the amount of intrinsic microporosity”. For example, spherical pores are characteristic for unconnected moldic pores, generally seen as low permeability rocks. Branching, complex pores are characteristic for connected interparticle pores, generally seen as fairly permeable rocks. Macro-pore shape relates to permeability indirectly through a geological frame work.

Thin sections, on which the image analysis are performed in this chapter, are prepared from dry core plug cut-offs. The macro-pore shapes of the samples are imaged under different resolution: a) high resolution images of 52 samples are acquired with an environmental scanning electron microscope (ESEM) images; b) I acquired also optical light (OLM) images of 62 samples (Table 1). Prior to thin section preparation, the rock is saturated by a blue colored resin under vacuum. In order to be able to acquire OLM and ESEM images, I prepared the thin sections without glass cover plate. In order to assess the variability of the macro-pore structure as a function of slice orientation, I cut a vertical and a horizontal thin section of 31 core plugs (Fig. 1) and I acquired computer tomography scans of two plugs with a diameter of 50.8mm.

Table 1: Description of image acquisition and processing of three different techniques applied in this study.

Acquisition Technique	**Pixel Resolution**	**Area Analysed**	**Binarization**	**Pitfalls**	**Age and Location**
ESEM	1.05 µm/pixel	(1.5mm x 1.17mm), five images	Gray scale thresholding (software: ImageJ)	Imaged area does not allow to cover and analyze large macro-pores, area picked might not be representative of the of the entire thin section	Australia ODP Leg194, Miocene (8) Middle East (Asab) Cretaceous, (21) Far East (Malampaya), Miocene (23)
OLM	2.13 µm/pixel	Full 1” and 1.5” thin section, rectangular roi	Indexed 256 8-bit color image in HSV space, manual palette editing (Software: Paint Shop and ImageJ) , manual brushing for air bubbles and impurities	- Time consuming manual editing of pixels -Thin section thickness (30 microns) is limiting factor for resolution	Middle East (Asab), Cretaceous (20) Middle East (Buhasa), Cretaceous (13) Far East (Malampaya), Miocene (29)
CT-scan	27 µm/pixel	Full 1” plug area, sliced into 187 individual 2D images, slices thickness: 27 µm	Gray scale thresholding (software: ImageJ)	Not the entire plugs are imaged	Australia ODP Leg194, Miocene (2)

The following paragraphs give a detailed overview over image acquisition, binarization procedure and the method of quantitative image parameter calculation.

Image Acquisition

Environmental scatter electron microscopy (ESEM)

Images are acquired using a Philips XL30 ESEM-FEG electron microscope at the Center of Advanced Microscopy at the University of Miami. This instrument is capable of obtaining images from standard blue epoxy-impregnated, polished thin sections in an uncoated state.

For image acquisition the ESEM is set to the solid-state backscattered electron detector mode. The degree of contrast of an image is dependant on the density contrast of the imaged surface. Calcite and dolomite grains appear much brighter than the pore space, which is filled with blue epoxy, because the reflection coefficient increases as the atomic number increases. Operational settings are set to obtain the maximum field of view of 1.5 mm x 1.17 mm. The magnification to obtain such an area of view is set to 80x, the working distance is 20.0 mm, chamber pressure is between 0.4 to 0.5 mBar. The aperture is 50 µm has and the voltage is around 20 kV and the spot-size is 3 or 4. The contrast is adjusted to a value of 90.8 and the brightness is set to a value of 42.9. Images of similar field of views have been used in the past for quantitative image analysis (Ehrlich et al., 1991; Anselmetti et al., 1998).

The acquired high-resolution ESEM images are saved as 1424x1064 8-bit gray-scale TIFF images, which translates to ~ 1 μm^2/pixel. The "depth-resolution" is negligible, since the ESEM beam penetrates the thin section only a few micrometers, allowing a real two dimensional image of the rock specimen.

In order to minimize the bias introduced by measuring an unrepresentative field of view, 5 different images from one thin section Ire processed. The views have been chosen along a predefined-grid, to avoid any subjective biased selection.

Optical light microscopy (OLM)

High-resolution images of polished thin sections are acquired using an Olympus C-4040 digital camera attached to an Olympus BH2 transmitted light microscope. A 2x magnification objective together with a 2.5x projection eyepiece in the extension tube enables coverage of an entire thin section of 25.4 mm with approximately 80 images when using 50% image overlap. To move the thin section in a predefined grid, a stage, mover and trigger mechanism of a conventional point counter is used. The images, which have a dimension of 1280x960 pixels Ire combined into mosaics using Photostitch$^{©}$.

The camera was set manually to an aperture of 2.3 and a shutter closing time between 1/500 and 1/800 seconds. The smallest possible aperture value was chosen to minimize optical distortion and to avoid shadows in the corner of the image. Maintaining constant light intensity during acquisition is important to ensure uniform intensity throughout a set of images. Since the feature of interest is the macro-pore space, the images are taken slightly overexposed (+0.7) to brighten all color of the blue epoxy.

Pixel resolution of digital images has massively improved over the last decade, allowing very low magnification images at high pixel resolution with the OLM. Our images have a very high digital resolution of approximately 2 µm/pixel. This high resolution creates very large image file sizes. Therefore, the original TIFF-images are converted into JPEG formats to reduce file size and to reduce analysis time.

Computed tomography imaging (CT-imaging)

Two plugs are scanned with x-rays at the High-Resolution X-ray Computed Tomography Facility at the University of Texas at Austin (Fig. 2). Slice thicknesses of 500 µm, 27 µm and 12.5 µm have been acquired. The images acquired at 500 µm resolution show too little detail and the images acquired at 12.5 µm are distorted. Undistorted image at high resolution and at a reasonable acquiring time is reached at a setting where voxels have a unidirectional length of ~27 µm each side in core plugs with 2.5 cm diameter. This resolution is comparable to the resolution of a thin section, since the imaged volume is obtained from transmitted light and the pore structure is averaged over the total thickness of the thin section, usually about 30 µm.

Fig. 2: Photograph of the two limestone core plugs (2.5 cm diameter) which are imaged by CT-scans (sample 172 and 173).

Image Segmentation

The image segmentation process is the most important step in image analysis, because it selects the features in question and the size/shape of the features. The goal of the image classification procedure is to separate the macro-pores from the background, which is composed of grains and micro-porosity. The final product is a binary image, composed of black color representing macro-pores and white color representing the grains and micro-porosity. Whereas this segmentation is a simple greyscale thresholding procedure in the ESEM images, segmentation of a color image is more complex.

Environmental scatter electron microscopy (ESEM)

The grayscale ESEM images are related to density contrasts and, thus, the binarization process involves a simple picking of a grayscale threshold; which separates the grain space (bright) from the macro-pore space (dark). By comparing the ESEM image with the thin section image under optical light microscopy, a grayscale threshold value of 70 was ideal to classify macro-pores. A median filter was applied to reduce high frequency noise prior to applying a straight forward grayscale threshold. The software used for processing is the “Image Tool V.3.0” (by University of Texas Health Science Center).

Optical light microscopy (OLM)

In previous studies, the segmentation has been performed by converting the true color image into an indexed image. The indexed image has been generated by selecting proper indices for macro-pore and grain/matrix space manually (Keehm, 2003; Van der Berg et al., 2002; Anselmetti et al., 1998) or thresholding RGB and/or HSV gray level bands (Fens, 2000; Ehrlich et al., 1991; Cabtree et al., 1984).

Extracting macro-porosity on a color image acquired under transmitted light is not as straight forward as in a grayscale image. In our case, thin section images are a two dimensional projection of a three dimensional rock. The nonzero thickness of the rock slice inevitably causes the Holmes effect when examining pore structure with transmitted light. If the thin section is relative thick compared to the grain and macro-pore sizes which are analysed, the volume of the grains will be exaggerated and the volume of the macro-pores will be understated. For example, micro-porosity is characterized by small grain sizes and small pore sizes, smaller than the thickness of the thin section. The macro-porosity is defined as connected pore space along a straight line from top to bottom of the thin section, excluding all areas affected by the Holmes effect (Fig. 3). Macro-pores are characterized in the ideal case by the light blue colors of the epoxy under an optical light microscopy, in contrast to the zone which is affected by the Holmes effect, like the hidden pore space around larger grains and micro-pores which show a darker blue coloring (Fig. 3). This definition excludes all pores smaller than 30 µm in length perpendicular to the 2D thin section plane.

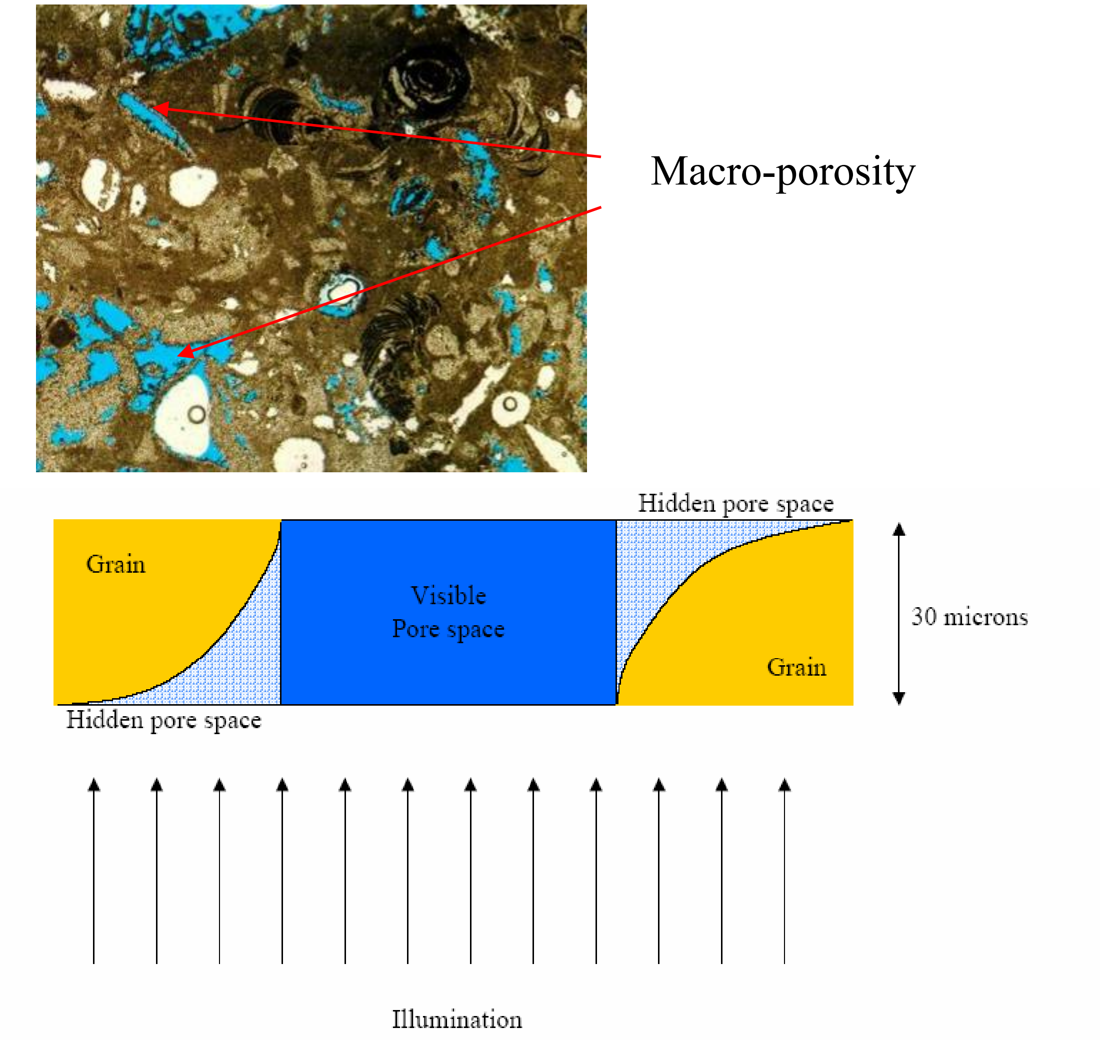

Fig. 3: Color plate of a thin section and a schematic definition of macro-porosity: Macro-porosity is the blue pore space excluding all hidden pore space affected by the Holmes effect (after Fens, 2000). The larger the grain size, the smaller the Holmes effect.

I reduce the colors to a 256 indexed RGB color palette using the nearest color method (Paint Shop Pro$^{©}$) which replaces the original color of a pixel with the color in the newly generated palette that is closest to its RGB value. The palette uses occurrence of colors as weighting, and ranks accordingly.

The palette is edited by hand on a pixel basis. Light color pixels, which have been proved under cross-polarized light to be part of the macro-pore space, are changed to blue in the color palette manually. The color pixels of bright-brown to white air-bubbles and unconnected macro-pores are changed in the indexed color palette to blue pixels. Editing 3-5 colors, a grayscale threshold is applied with ImageJ$^{©}$. A median filter is used on the binary image to reduce noise.

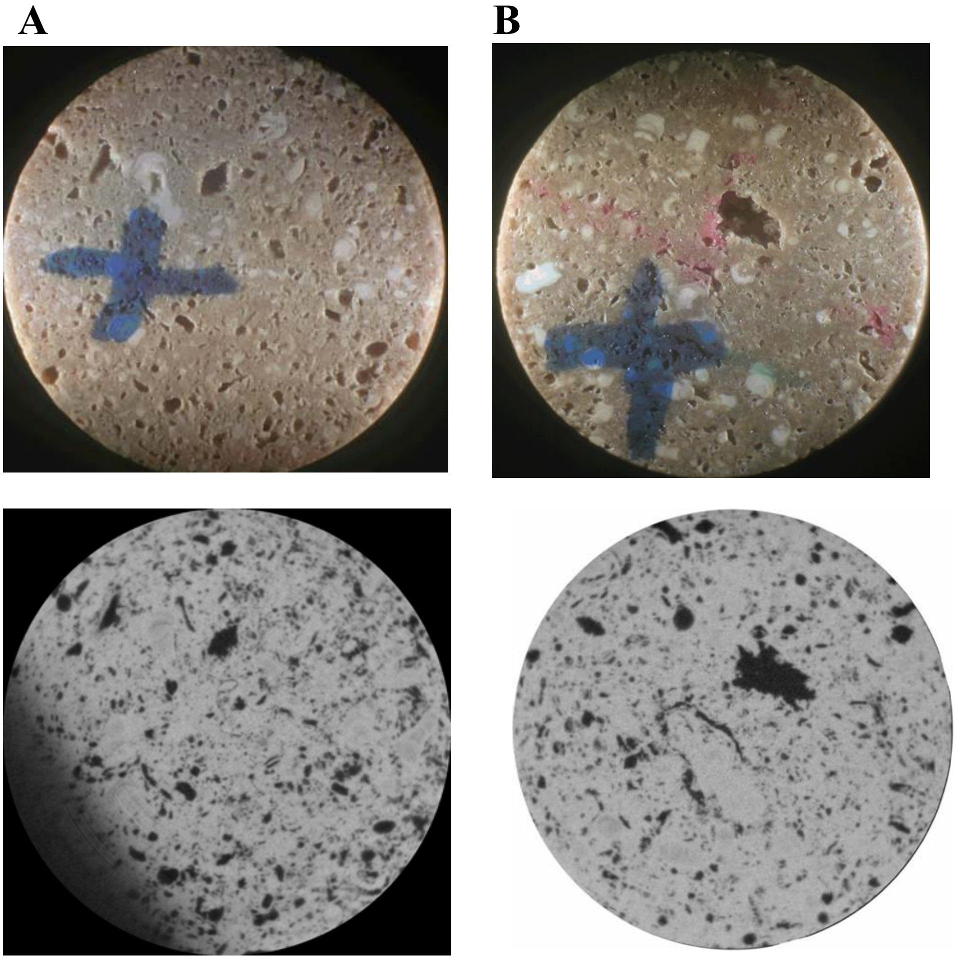

Fig 4: Top of core plugs of the two samples used for CT scans and corresponding CT-scan grayscale image (below). The image field of view is 25.4 mm (sample 172 on the left and sample 173 on the right).

Computed tomography imaging (CT-imaging)

The CT-scans are imported as 8-bit jpg-files into ImageJ and analyzed in a batch sequence. A basic 256 color grayscale classification is applied to the images to obtain a binary image with white color representing the grain space and black color representing the macro-pore space. The grayscale value that separate the grain from the macro-pore space is based on best-fit visual comparison with the end surfaces of the core plugs (Fig. 4). The threshold grey values vary between a value of 70 and 100, resulting from different rock microstructures and subsequent varying scan settings.

Image parameter – Pore shape factor γ

Anselmetti et al. (1998) defined the pore shape factor (γ) of a single pore is

$$\gamma_{\text{por}} = \frac{P}{2\sqrt{\pi A}} \qquad (1)$$

whereas

P = Perimeter [μm], A = Area [μm^2] and π = 3.14159265.

By using the square root of the area, the γ_{por} value becomes a dimensionless parameter. For a perfectly circular shape, γ_{por} becomes one and any deviation from this spherical pore shape will result in an increase of the γ_{por} -value (Fig. 5).

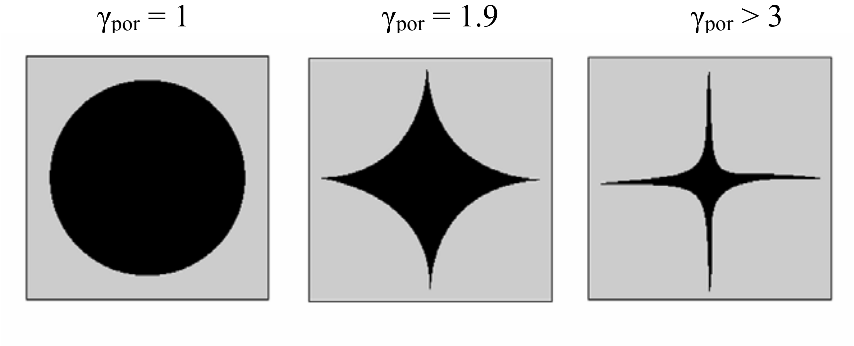

Fig. 5: The pore shape factor (γ_{por}) increases from circular (γ_{por}=1) to complex branching pores (γ_{por}>3), adapted from Anselmetti et al. (1998).

To calculate the γ_{por} value of the entire macro-pore population on a thin section, γ_{por} is normalized by the macro-pore size:

$$\gamma = \frac{\sum_i (A_i \gamma_i)}{\sum_i A_i} \qquad (2)$$

This procedure puts the emphasis on the large macro-pores within a pore system, which are more likely, due to their size, to be important for fluid flow in the rock. All macro-pores smaller than 5 pixels are excluded for the calculation of γ.

Sensitivity analysis of pore shape factor γ

Prior to relating macro-pore shapes to permeability, I assessed the sensibility of γ to image magnification, representative area and pixel resolution. Magnification, representative area and pixel resolution are interlinked. By changing the magnification, the imaged area will change as well. The pixel resolution will also change, since the camera setting with which the image is acquired is independent of magnification, is a constant setting of 1424 x 1064 pixels per image. Under the ESEM γ sensitivity is evaluated for magnification from 80x to 240x and then to 725x (Fig. 6). These changes result in changes in γ from 2.67, to 2.11 and 2.58 at the highest magnification. Comparing the γ values of the 5 acquired images per thin section, I observe a γ difference of up to 20% due to different pore populations analyzed. The γ_{por} value of a single macro-pore analyzed at low magnification (80x) up to very high magnification (1900x) increases consistently from a γ_{por} of 2.4 to a γ_{por} of 5 at the highest magnification (Fig. 7). This effect can be explained by an increase of the perimeter/area ratio due to better pixel resolution of the pore to grain boundary at higher magnification.

Increasing the grain-pore segmentation threshold within interpretative boundaries, from grey-level value of 70 (restricted pick) to 135 (open pick), increases γ by 16% on average in the 52 thin section images. Increasing the number of macro-pores analyzed from 50 to 5000, resulted in an average decrease of 18% in γ-values.

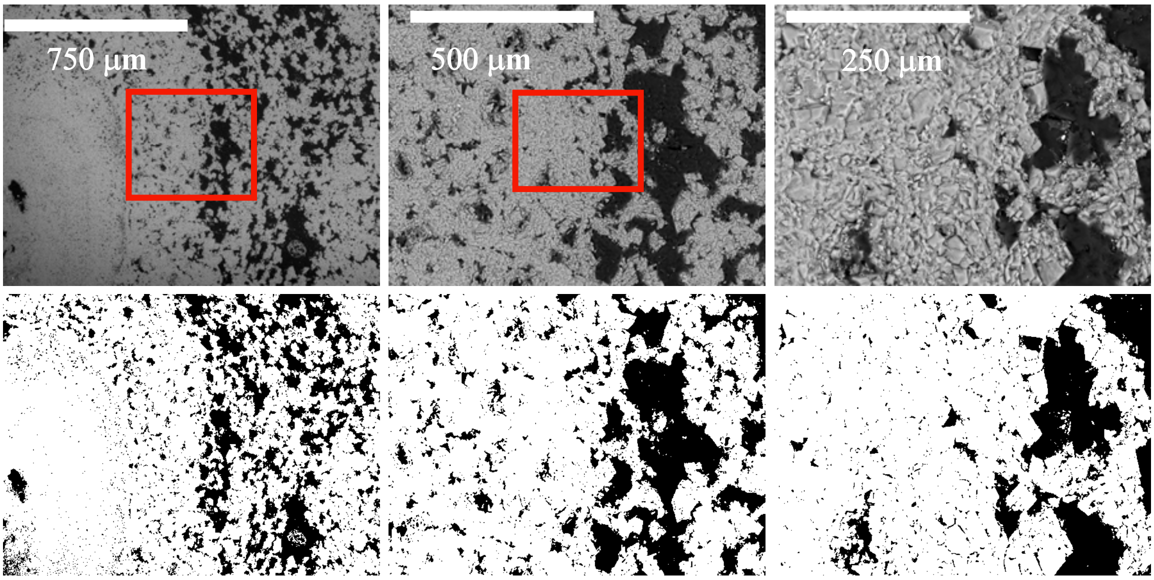

Fig. 6: The upper row shows unprocessed ESEM images of one sample at different magnifications, while the lower row shows the corresponding binary images. The pore shape factor γ varies due to differences in the resolution and the pore population analyzed (right to left): 80x = γ 2.67; 240x = γ 2.11; 725x = γ 2.58.

Using images acquired by the optical light microscope, I investigate further the effect of macro-pore size on the γ-values. Plotting γ_{por} of each single macro-pore versus the size of the macro-pore in two grainstones with interparticle porosity shows a general trend of decreasing maximum γ_{por} values with decreasing pore size (Fig. 8). This trend most likely reflects the "smoothing" effect of the grain-pore boundary with decreasing size of the macro-pores. In comparison to sample 45, sample 91 has larger macro-pores with more complex pore shapes, as indicated by the larger spread of γ_{por} values of the large macro-pores (Fig. 8).

Figure 9 shows a plot of γ versus the lower cut of values of macro-pore sizes included to calculate γ, using equation 2. In all samples analyzed, there is a steady trend of decreasing γ with using smaller macro-pore size cut-off values for the calculation of γ. For sample 91 this trend starts when including macro-pore size smaller than 10,000 square pixels in the calculation, whereas for sample 45 the trend can be observed by including macro-pore sizes smaller than 2000 square pixels. Using all macro-pores detected in the thin sections, the calculation of γ using Equation 2 yields to a γ value of 2.34 for sample 91 and a lower γ value of 2.07 for sample 45.

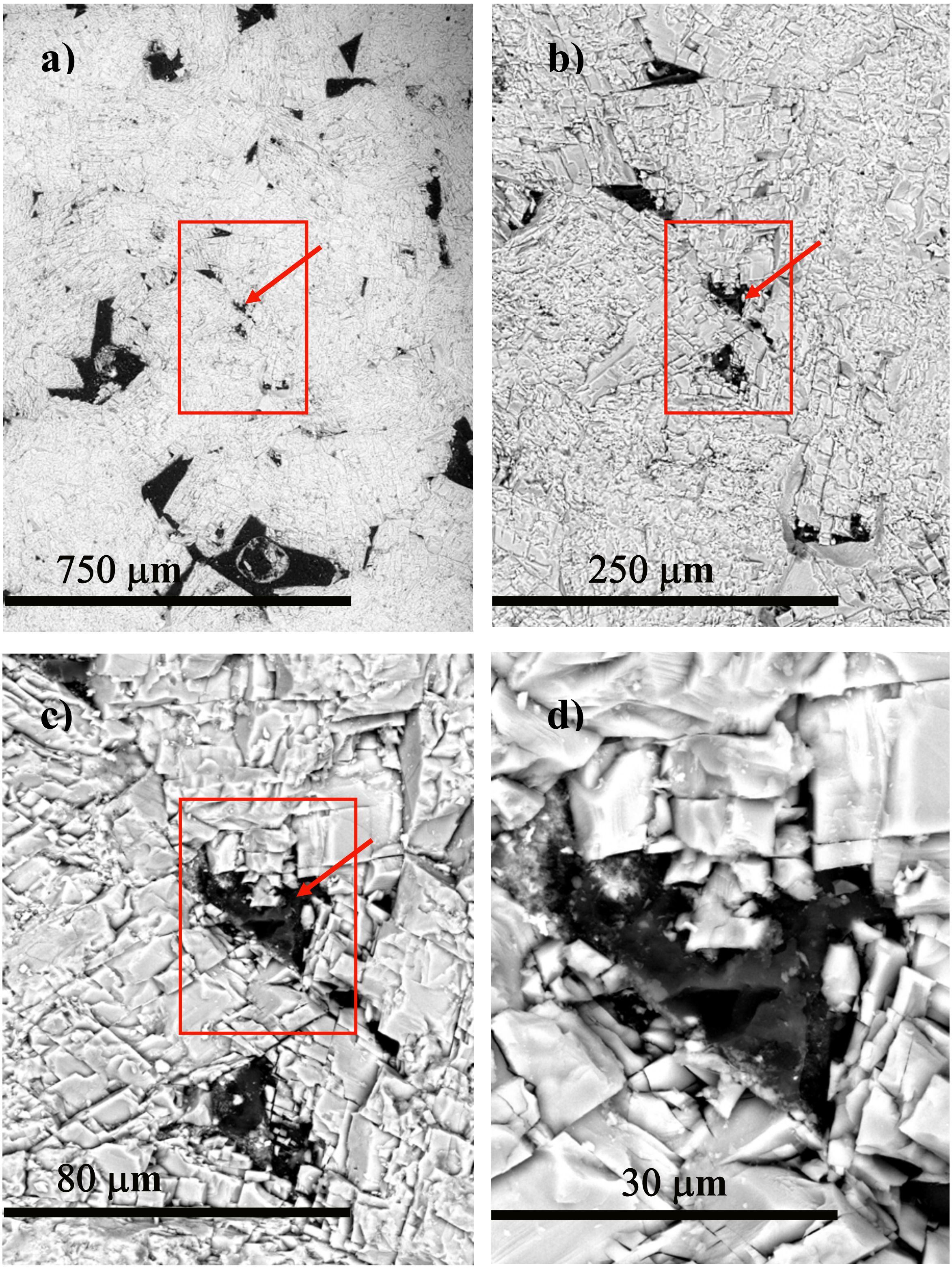

Fig. 7: Pore shape factor γ is strongly dependant on resolution. The higher the resolution, the higher the γ_{por} -value: a.) (80x) $\gamma_{por} = 2.4$, b.) (725x) $\gamma_{por} = 3.8$, c.) (1500x) $\gamma_{por} = 4.2$, d.) (1900x) $\gamma_{por} = 5$.

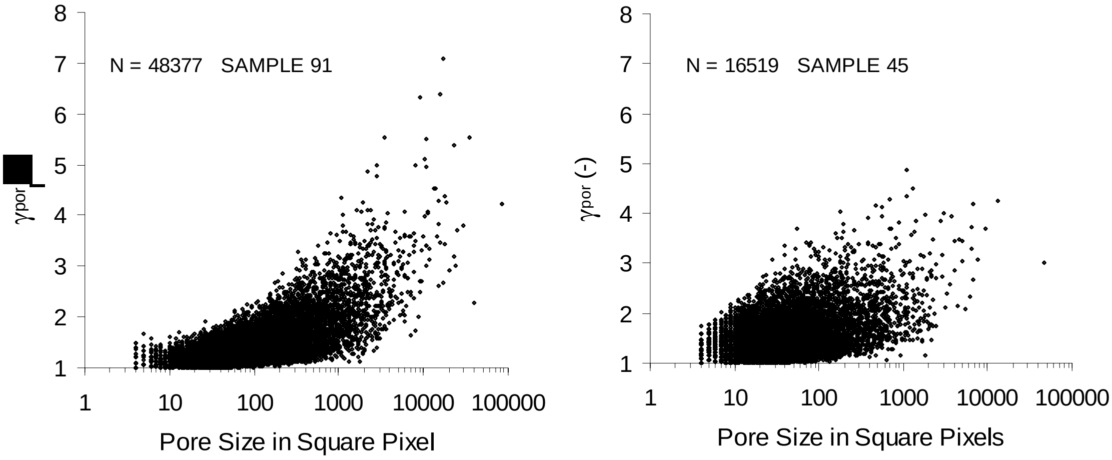

Fig. 8: Pore shape factor γ_{por} of a single macro-pore versus the macro-pore size. Both samples, 91 and 45, are dominated by a few large and many small macro-pores. γ_{por} tend to become smaller with decreasing macro-pore size.

The correlation coefficient between pore shape factor γ and permeability decreases, if the analysis is restricted to the 500 largest macro-pores from $r^2=0.49$ to $r^2=0.41$ (Fig. 10). Further reduction of the pore population analyzed, excluding all macro-pores but the 50 largest macro-pores, leads to an even less significant correlation ($r^2=0.34$). These results contrast to the weak γ - permeability correlations on pore populations from thin section images acquired by ESEM. If the analysis is restricted to the 50 or the 500 largest macro-pores, the γ - permeability correlation coefficient is low with correlation coefficients of $r^2=0.2$ and respectively $r^2=0.04$. Even if I use all detected macro-pores in our analysis, the γ - permeability correlation does not improve significantly ($r^2=0.12$).

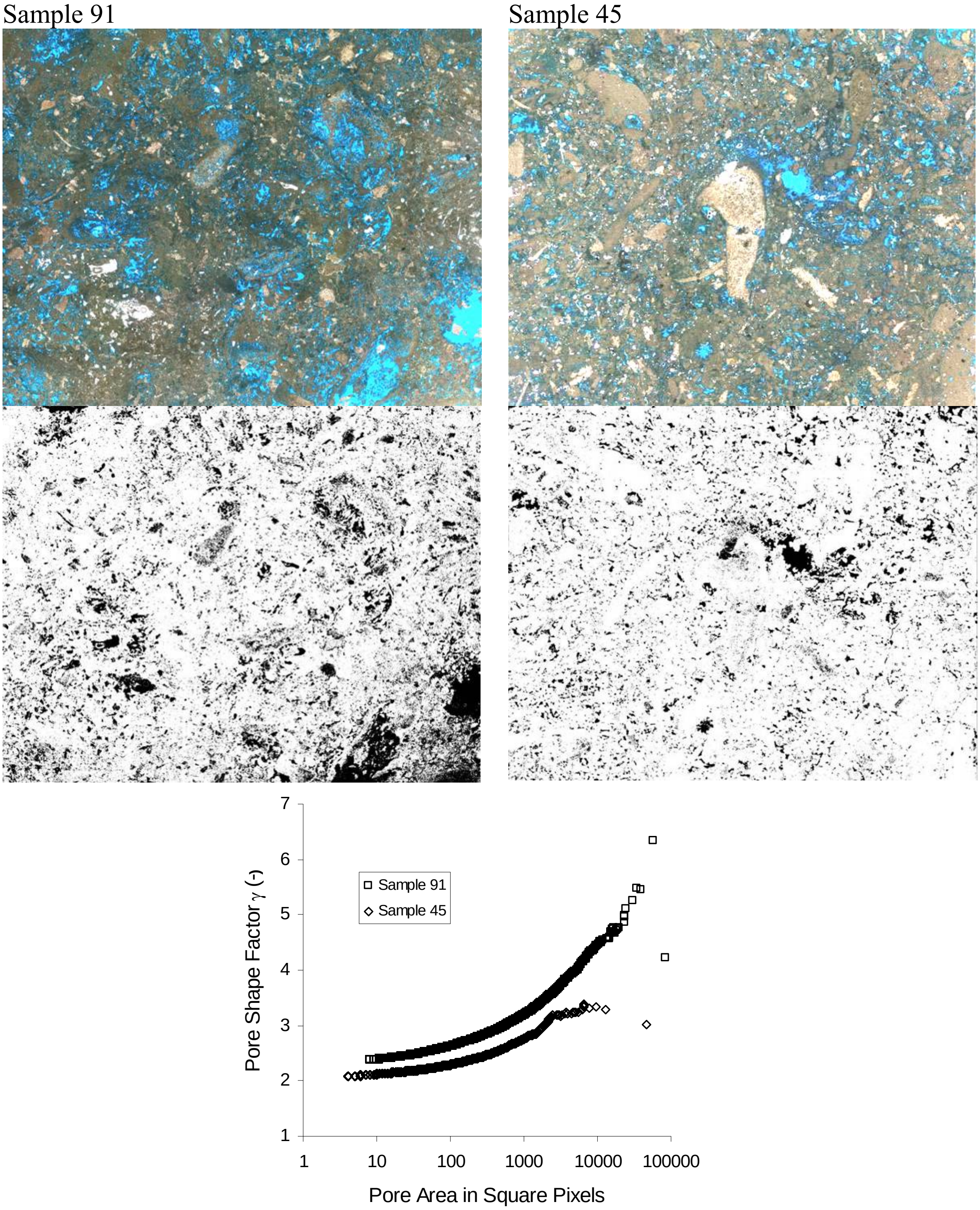

Fig. 9: Pore shape factor γ versus the lower macro-pore size cut off used for the analysis. Both samples, 91 and 45, show a trend of decreasing γ values with subsequent increments of smaller macro-pores for analysis.

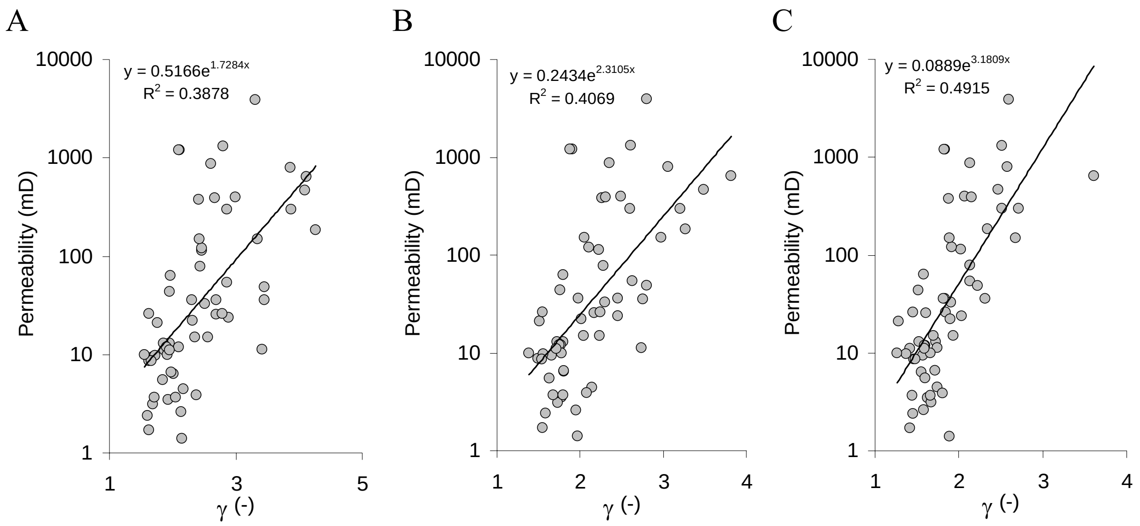

Fig. 10: Calculated pore shape factor γ with (A) 50 largest macro-pores, (B) 500 largest macro-pores and (C) entire pore population. The correlation coefficient between permeability and γ increases when smaller macro-pores are incorporated in the calculations.

Correlation of γ and permeability

For the evaluation of the γ – permeability correlation, first I analyze γ on environmental electron scatter microscope (ESEM) images taken at the lowest possible magnification of 80x, in order to obtain the largest representative field of view. Second, I analyzed γ of the entire macro-pore population of full thin section images acquired by an optical light microscope (OLM). The selected samples have porosities from 7% to 35% (Fig. 11 and 13). A large permeability variation of several orders of magnitude is observed in the samples analyzed using the (ESEM) and the (OLM) (Fig. 11 and 13). Over the entire porosity range, the γ values vary between 1.1 and 4.2 for macro-pores imaged by using ESEM and between 1.25 and 2.75 for macro-pores imaged by using OLM (Fig. 14).

An exponential regression analysis of permeability and γ is performed by analyzing the entire macro-pore population of each thin section ESEM image. As seen in Figure 11, the correlation coefficient between permeability and γ ($r^2 = 0.12$) is as low as the correlation coefficient between porosity and permeability ($r^2 = 0.2$). The scatter of datapoints in Figure 11 shows, both γ and porosity, is not very useful to predict permeability.

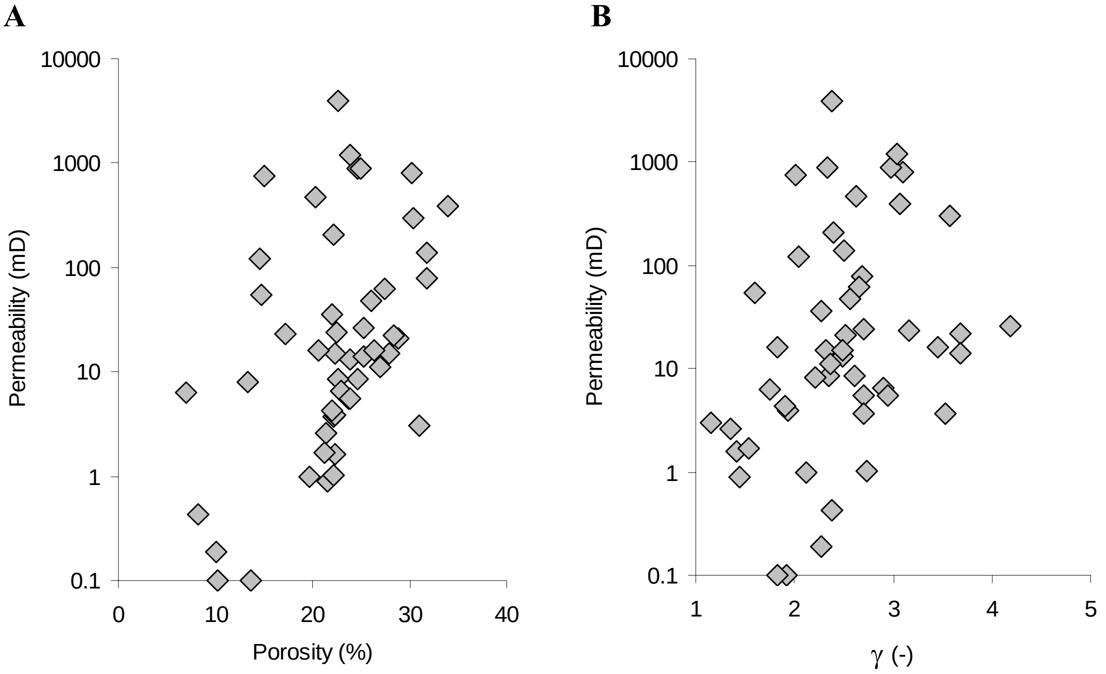

Fig. 11: (A) Porosity vs. permeability plot shows a large scatter of permeability and (B) pore shape factor γ vs. permeability plot shows also large scatter of permeability. The γ values are calculated from macro-pore population on ESEM thin section images.

In contrast, γ values analyzed on macro-pores from OLM images show a much better correlation to permeability (r^2=0.46) (Fig. 13b). The porosity of the same dataset shows a very weak porosity – permeability correlation (r^2=0.07) (Fig 13a).

There appears to be a γ cut-off value for maximum permeabilities. In the permeability-gamma plots (Fig. 11b and 13b), all samples with γ values below 1.9 are restricted to low permeabilities (below 100mD). This observation holds true for quantitative image analysis performed on images acquired by both, ESEM and OLM.

Examination of the pore texture of the high resolution ESEM images lead to the following observations: Whereas for some cases the γ value represented the expectations from qualitative visual estimation of the macro-pore shape in the thin sections, in other cases the γ value did not represent the visual estimation of the macro-pore shape. For example, thin section micrograph 12a shows a sample with dominant interparticle porosity and branching macro-pores display a high γ value of 3, as expected from the simplified pore shape cartoon in Figure 5. The assumption of a high permeability value in the case of branching pores is also confirmed by the high permeability of this sample. A recrystallized dolomite with intercrystalline-vuggy porosity shows a lower γ value (1.9) as expected from the more simple, isolated pores (Fig. 12b). The permeability of this rock much lower (15mD) as indicated by the lower γ.

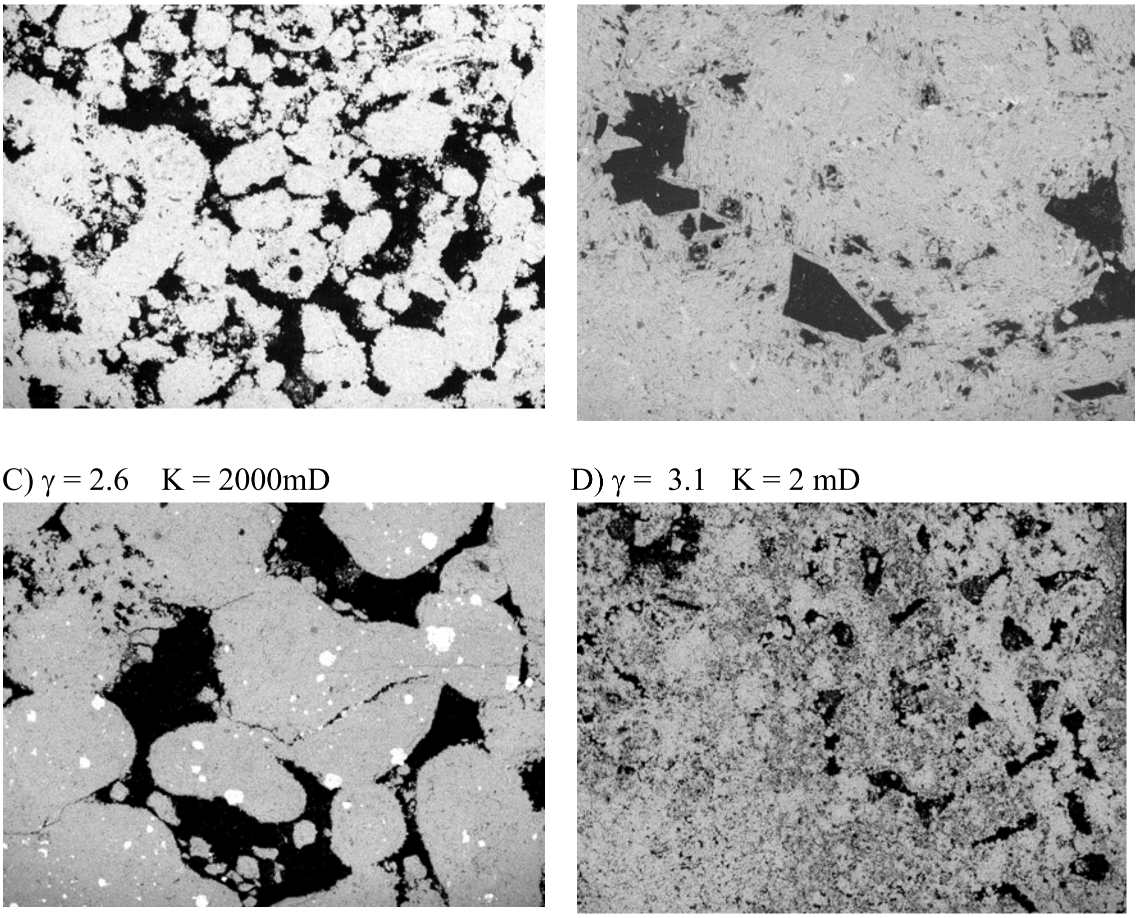

A) $\gamma = 3$ K = 1000 mD

B) $\gamma = 1.9$ K = 15 mD

C) $\gamma = 2.6$ K = 2000mD

D) $\gamma = 3.1$ K = 2 mD

Fig. 12: ESEM images of specific pore types and corresponding γ values.

Samples in which the visual estimation of the macro-pore space was different from the quantitatively measured pore shape factor γ can be classified into two categories: (a) samples with extreme large macro-pores and (b) samples with many small macro-pores. A grainstone with large interparticle macro-pores shows a very low γ value (2.6) for the measured permeability of 2000mD (Fig. 12c). A coralline rock with large and small intraframe pores (Fig. 12d) shows a high pore shape factor γ value of 3.1, despite its very low permeability of 2mD and the visual estimation of relative round pore shapes. The samples which show relative high γ values (> 3) but low permeabilities (between 2 and 20mD) are dominated by small pores (dominated by microporosity).

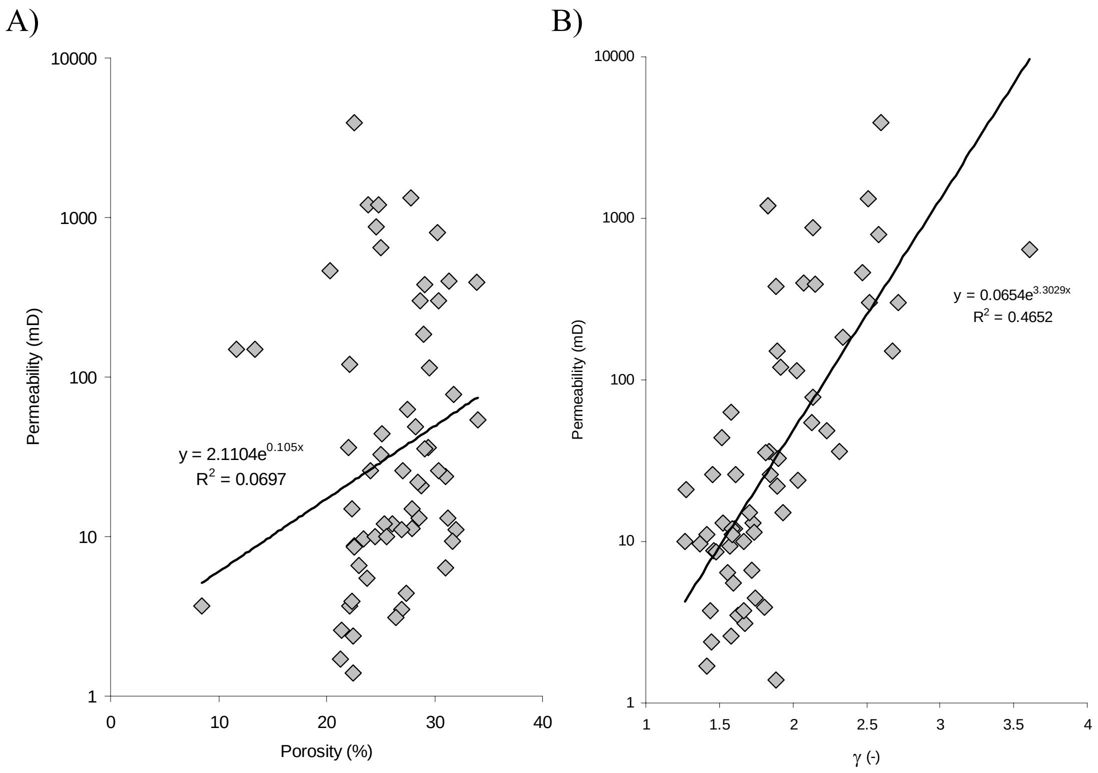

Fig. 13: (A) plot of porosity vs permeability and (B) γ vs permeability. Exponential regression analysis shows a much better correlation between the pore shape factor γ and permeability compared to the weak porosity – permeability correlation (γ analyzed on macro-pores from thin section photographs acquired by OLM).

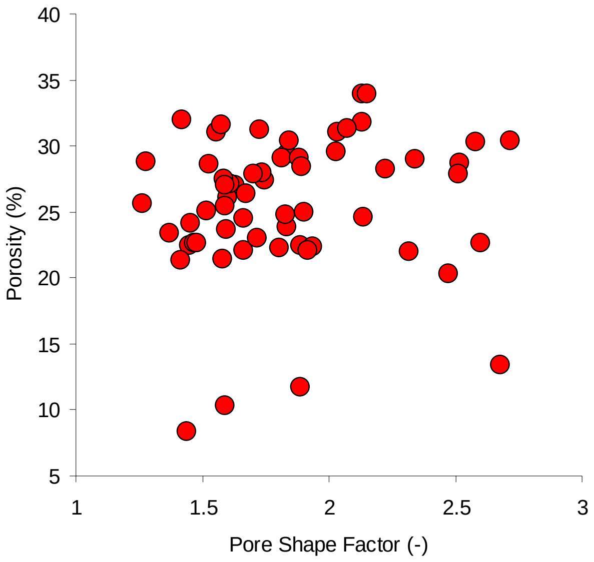

Fig. 14: Porosity vs. pore shape factor γ. The plot shows large variety of γ, unrelated to porosity. The γ values are calculated from binarized thin section images acquired by optical light microscopy (OLM).

Variability of permeability and γ within a plug

A cross plot of the pore shape factor γ calculated on the horizontal orientated thin section image versus γ calculated on the vertical orientated thin section image shows orientation independent γ values (Fig. 15). The γ values of the vertical and horizontal slice orientation correlate with a r^2 of 0.37. The correlations between γ calculated on horizontal and vertical orientated slices is better at γ values below 2.5 (most are within a range of +/- 0.25) than at higher γ values.

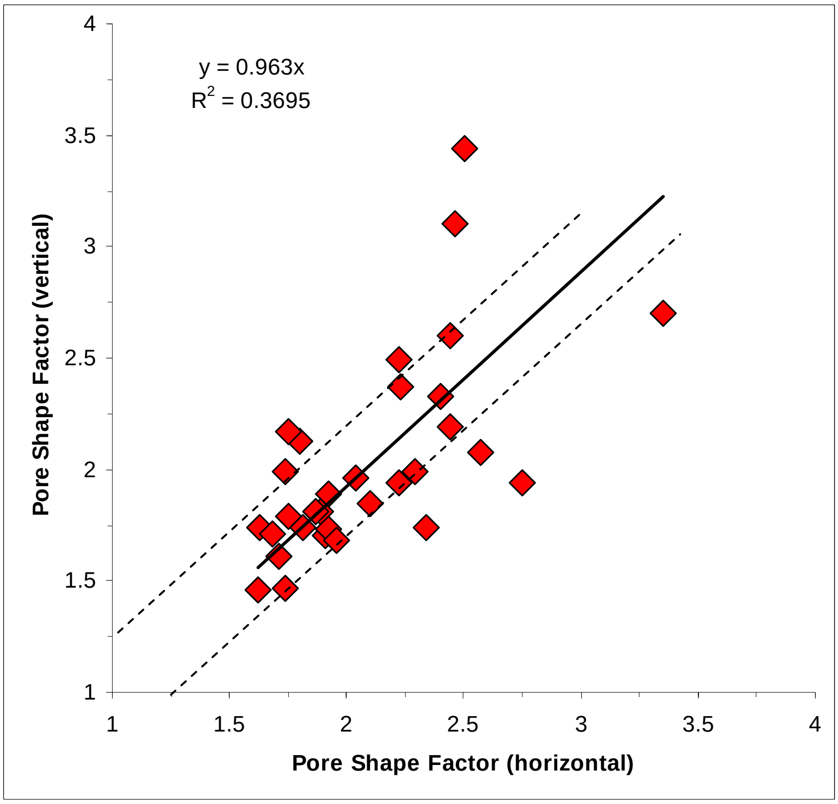

Fig. 15: Crossplot of pore shape factor γ calculated on an image of the horizontal orientated thin section versus pore shape factor γ derived from the vertical orientated thin section image. Most pore shape factor γ values correlate well at low gamma values within a range of +/- 0.25.

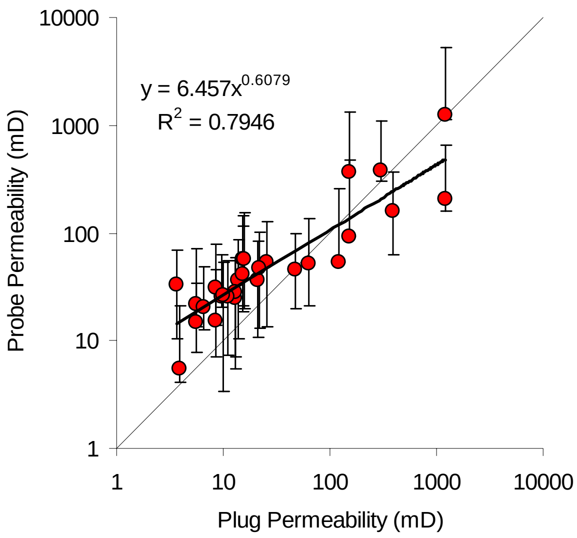

Fig. 16: A reasonable good correlation exists between the average probe permeability and plug Klinkenberg permeability. The minimum/maximum values, shown by the error bars, indicate that the permeability variation of each sample at the thin section scale is within one order of magnitude in permeability.

In order to evaluate he permeability variations within a plug, I used 3 to 7 spot point probe permeability measurements along a line across the plugs end surface. The dataset shows averaged probe permeabilities range from below 10 mD up to 1000 mD (Fig. 16). The probe permeability variation of the up to 7 spot measurements is maximum one order of magnitude in permeability within one sample, as indicated by the error bars in Figure 16. The averaged probe permeameter measurement is within one order of magnitude of the permeability of the plug permeability (Fig. 16). In the low permeability range, probe permeability appears to measure higher permeabilities than the permeabilities measured on the plug scale (Fig. 16). A power law regression analysis leads to a correlation coefficient of $r^2 = 0.79$ between probe permeability and plug permeability (Fig 16). Three samples show deviation from the larger scale core plug permeability of more than one order of magnitude. For example, a coral carbonate rock (sample 45) shows exceedingly higher probe permeameter readings of permeability (Fig. 17b), the intraframe pore type results in good pore connectivity at small scale but bad pore connectivity at core plug scale.

Two other samples show also much higher probe permeameter readings compared to the plug permeability, caused by large well connected vuggy porosity and not well connected microporosity with patchy cementation. Specific pore types like intraframe porosity and vuggy pore types apparently cause the probe permeability to be higher at pore scale compared to plug scale permeability. Thus these three samples are excluded from the analysis to allow meaningful correlation.

Variations in probe permeability documents that permeability is mostly homogeneous but can also be very heterogeneous at the plug scale. For example, sample 27 shows re-crystallization and alteration of its original texture, creating vuggy and intercystalline porosity (Fig. 17a). The spatial distribution of the vugs apparently causes the permeability to be heterogeneous along the line of measurements. In contrast, very homogeneous pore structures, like a coralline rock with intraframe porosity show relatively homogeneous permeability distribution (Fig. 17b). Similarly, a skeletal grainstone-packstone with benthic foraminifers and dissolution features with patchy distribution of interparticle porosity and vuggy porosity (Fig. 17c) and a very heterogeneous skeletal packstone which is heavily bioturbated, differentially leached with moldic, vuggy and interparticle porosity (Fig. 17d) show homogeneous permeability distribution despite their heterogeneity in pore types and patchy cementation.

A) Plug Perm: 150 mD / Porosity: 13%

B) Plug Perm: 4 mD / Porosity: 8%

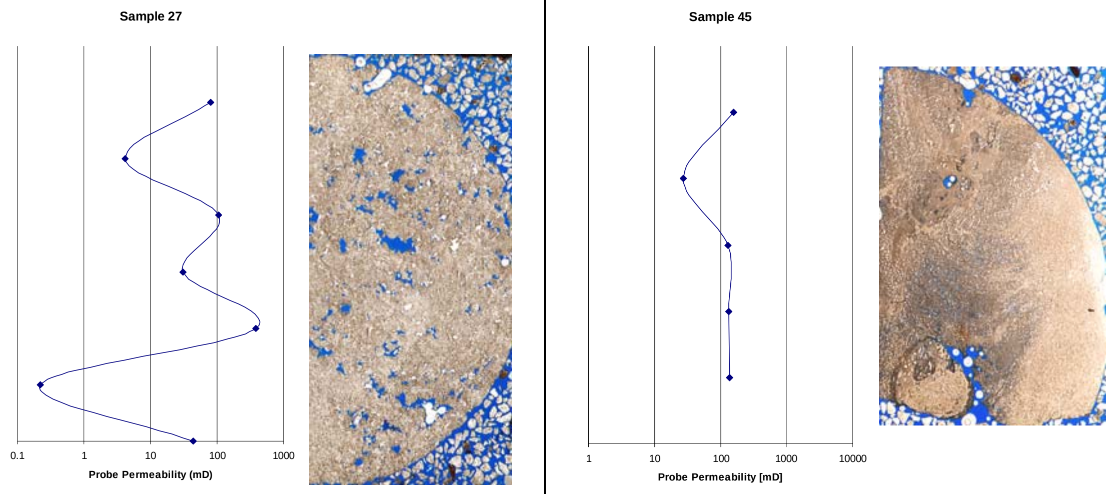

C) Plug Perm: 22 mD / Porosity 28%

D) Plug Perm: 63mD / Porosity: 27%

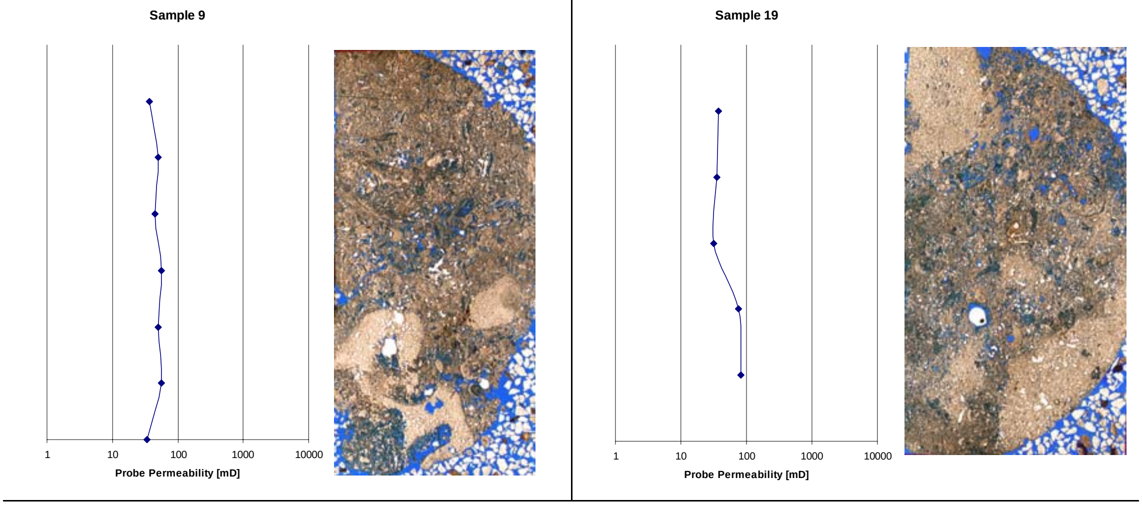

Fig. 17: Probe permeability variations across a sampling line of core plug end surface.

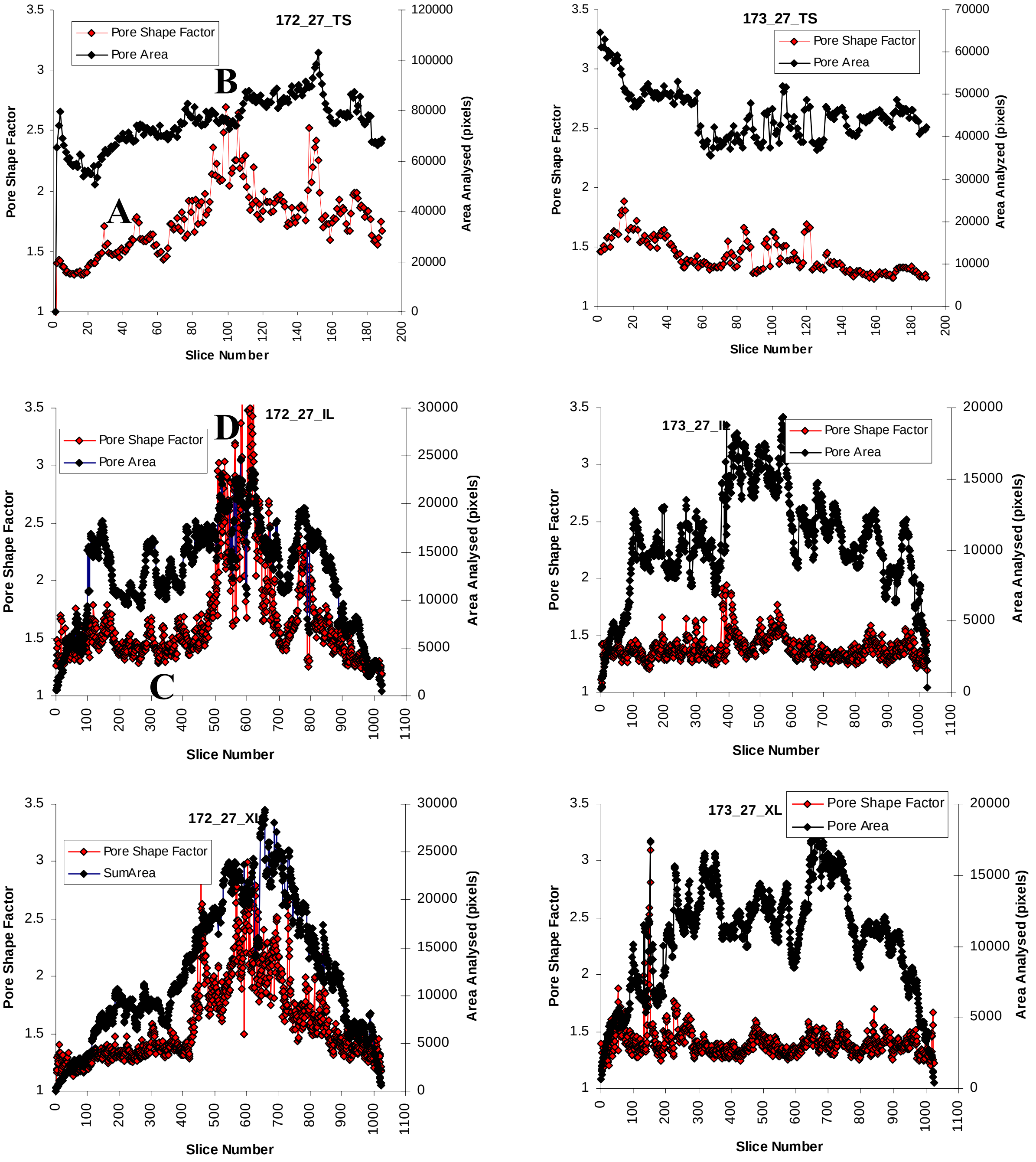

Fig. 18: Pore shape factor γ of two core CT-scans at 3 different orientations (sample 172 on the left, sample 173 on the right). Overall, the pore shape factor γ is very consistent over the scanned core length. The annotation (A) to (D) highlights positions of 2D micrographs seen in Figure 19.

Pore shapes factor γ values are also calculated from 2D images derived from CT-scans of the entire core plug (on two samples), at three different slice orientations: 1.) perpendicular to the long axes (TS) parallel to the long axis, 2.) Image sets parallel to the long axis of the core (IL), and 3.) in a 90 degree angle (XL). Overall, the pore shape factor γ is very consistent over the entire scanned core length (Fig. 18), despite the macroscopically heterogenic appearance with frequent residual algae (Fig. 2, 4 and 19).

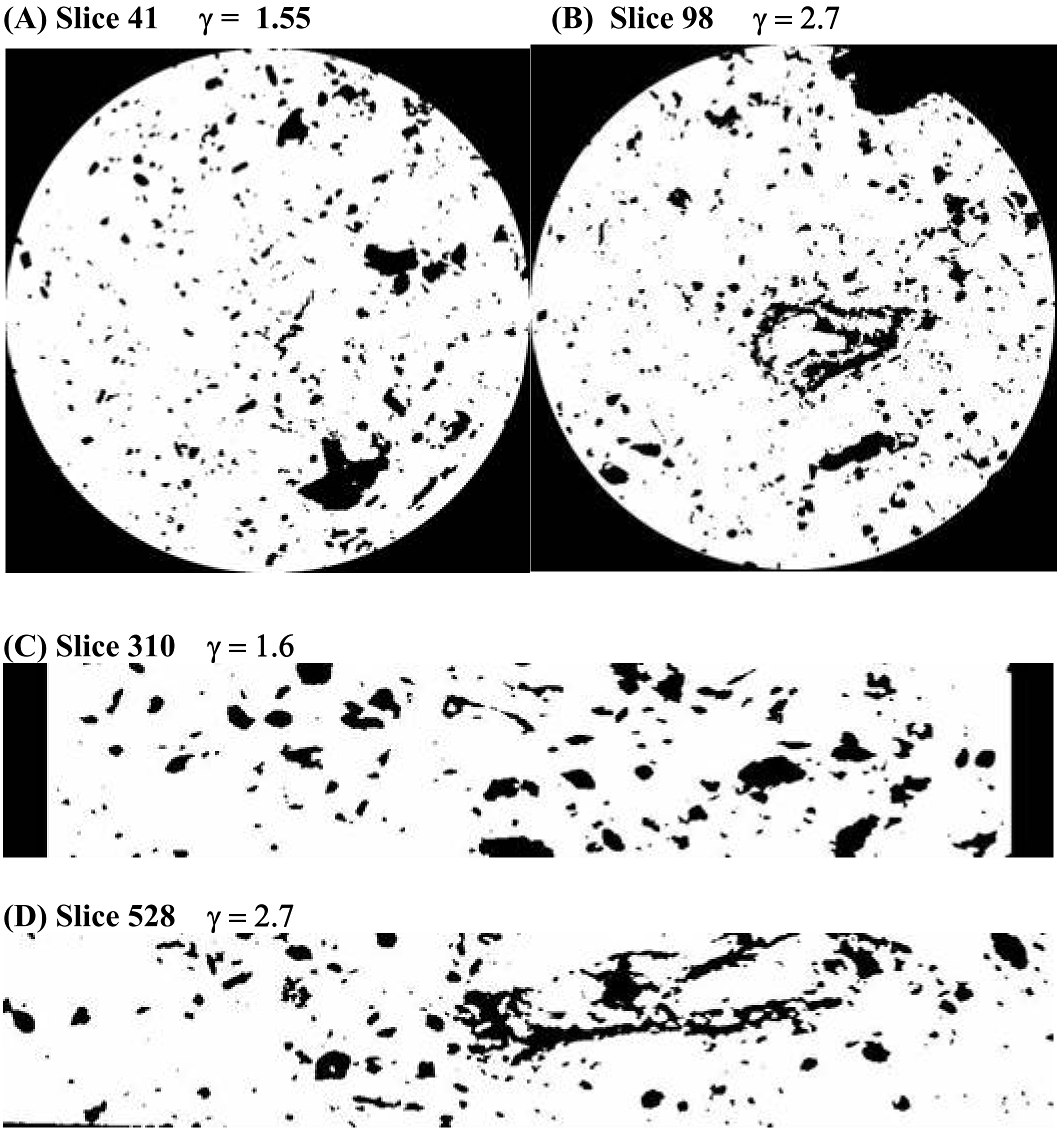

(A) Slice 41 $\gamma =$ **1.55**

(B) Slice 98 $\gamma = 2.7$

(C) Slice 310 $\gamma = 1.6$

(D) Slice 528 $\gamma = 2.7$

Fig. 19: Selected 2D slices to highlight variations in pore shape factor γ value caused by heterogeneities in the rock and pore texture. The letters correspond to annotations in previous Figure 17.

Heterogeneities contribute to an increase in pore shape γ factor from values of 1.5 to >3.5, whereas the γ value appears to be widely unrelated to the imaged pore area. The core plugs with the higher permeability (sample 172) has a slightly higher pore shape factor γ than the low permeability sample (sample 173), which could be an indication of more complex, branching and connected macro-pores.

The binary image of the sections in which a large rhodolith-algae structure causes pore structure heterogeneity is shown in Figure 19. Figure 18a and 18c show the relatively homogeneous pore structure and γ values of 1.55-1.6 at vertical and horizontal slice orientations. In the contrast binary images of the sample in Figure 18b and 18d show heterogeneities caused by rhodolith-algae. These heterogeneities cause γ to increase to a value of 2.7.

Discussion

γ derived from ESEM and OLM technique

I compare the pore shape factor γ calculated from the pore population imaged by the ESEM to. γ derived from OLM. The γ values derived from macro-pore analysis on ESEM images are less well correlated to permeability than the γ values calculated on the macro-pore population derived from OLM images. The main reason appears to be twofold: (a) the ESEM image acquiring technique has a higher image resolution of the pore texture since the depth of imaging is limited to the first few microns of a thin section; and (b) even at the lowest ESEM magnification, the images show a very small field of view of the sample (~ 1.5 mm).

Our ESEM technique is able to detect macro-pores in the pore size spectrum from 1 µm to 200 µm in diameter whereas the OLM image analysis technique detects macro-pores in the range of 30 µm to over 1000 µm in diameter. The high resolution of the ESEM images result in calculating γ values on a pore population which incorporates micro-pores whose pore shapes apparently do not control the permeability. The high resolution of ESEM images leads to uncharacteristically high γ values in samples dominated by microporosity which have a relative low permeability at a given porosity. Apparently, the ESEM technique resolves the very small complex pore system which lead to high pore perimeter at a given pore area and subsequently γ values which are too high compared to the permeability of the sample. Further, the SEM image analysis covers a very small area of the thin section compared to the OLM full thin section images. The γ values calculated on a pore population derived from a small field of view in ESEM images are less likely to be a statistically reliable representation of the pore structure of the entire core sample. As shown, larger branching macro-pores are excluded from the analysis, since those macro-pores intersect with the boundaries of the image. The digital image analysis of the resulting pore population lead to γ values which are too low, which do not consider the shape of large macro-pores that contribute most to fluid flow.

On the other hand, γ calculated on macro-pores from OLM images captures the characteristic of rounder moldic-vuggy pores of rocks with lower permeability (<100mD) and low γ (<2), microporosity rocks with lower permeability (<100mD) and low γ (<2), versus branching interparticle pores of rocks which show higher permeability and higher γ (>2.5). With decreasing macro-pore size of the pore population analyzed, the pore shape factor γ decreases (pores are described as being more circular) due to a smoothing effect on the macro-pore to grain boundary; the OLM image resolution limits our ability to resolve the macro-pore to grain boundary of small macro-pores which results in a decrease in the macro-pore perimeter and the perimeter over area ratio decreases too. Therefore, low permeability samples (<100mD) with many small macro-pores have a tendency to result in pore shape factor γ values below 2.

Conclusion

Using digital image analysis to characterize the macro-pores in carbonates is a powerful tool for permeability prediction. This study shows that the macro-pore shape and the macro-pore size measured on OLM images control the permeability in carbonates.

The pore shape factor γ captured by digital image analysis is related to macro-pore shape and macro-pore size. Compared to the weak porosity-permeability correlation in our carbonate rocks, the pore shape factor γ reduces uncertainty in permeability prediction by two orders of magnitude in permeability. An OLM image resolution of 2.13 microns/pixel and a field of view of the entire thin section (1” to 1.5”) proves to be a good statistical representation of the whole plug, given the good correlation of γ with permeability. Samples with low pore shape factor γ values (< 2) reflect samples with low permeability (<100mD) at a given porosity.

The macro-pore population of an entire thin section needs to be analyzed in order to obtain a representative field of view. Due to heterogeneities and wide ranges of pore sizes from microns to centimeters, a small area of the thin section would not be representative of the entire sample. The pore shape factor γ, derived from macro-pore area and macro-pore perimeter, is strongly dependant on the chosen pixel resolution and field of view. γ values calculated on low magnification optical light microscopy (OLM) images show a much better correlation to permeability than γ values derived from low magnification environmental scatter electron microscopy (ESEM) images. It is therefore recommended to use OLM images for γ calculation instead of the higher resolution ESEM images.

CT-scans of two plugs show that the pore shape factor γ is a relatively constant measure of the macro-pore shape ($\gamma = \pm 0.2$) at different CT-scan slice orientations but is limited by the heterogeneity of the sample. Sample sections which show a high degree of heterogeneity have the potential of showing higher γ values than the homogeneous part of the sample. Overall, γ values show very little statistical variation in the shape of macro-pores over the entire plug.

Chapter 2

ROLE OF MICRO-POROSITY FOR THE ACOUSTIC BEHAVIOR OF CARBONATES – *IMPLICATIONS FOR PERMEABILITY PREDICTION*

Abstract

The hypothesis of this study is that macro-porosity is largely ineffective for sonic velocity. To test the hypothesis ultrasonic velocity (1 MHz) on large variety of pore and rock types of 138 carbonate samples are measured as well as the size and shape of the pores for the examination of their relationship to the rock compressibility and sonic velocity. To quantify pore shapes on macro-pores, digital image analysis (DIA) on macro-pores (>30 µm in diameter) is performed on thin section images. Micro-porosity is calculated by subtracting macro-porosity from porosity measured on a plug. Micro-porosity displays a better correlation (r^2=0.83) with compressional wave velocity than total porosity (r^2=0.54), confirming the hypothesis that macro-porosity is mostly ineffective for acoustic velocity. Multiple linear regression analysis between velocity, porosity and four quantitative DIA parameters of the rock's pore structure results in a very good correlation coefficient (r^2=0.87), indicating that the knowledge of pore structure reduces velocity uncertainty. Carbonate rocks dominated by micro-porosity are characterized by low velocity at a given porosity, whereas carbonate rocks dominated by vuggy-intercrystalline macro-porosity shows higher velocity than predicted by Wyllie's time average equation.

The pore space stiffness K_{por} is a good descriptor of the rock's compressibility variations at a given porosity (Mavko and Mulerji, 1995). I show that the pore space stiffness K_{por} does uniquely quantify the velocity variations of carbonates at a given porosity. Recrystallized dolostones with vuggy-intercrystalline macro-porosity show a normalized (K_{por}/K_{min})-value of 0.2 while carbonate rocks dominated by microporosity have a normalized pore space stiffness K_{por}/K_{min} -value of around 0.1. Furthermore, low pore space stiffness K_{por} indicates carbonate rocks with low permeability at a given porosity when correlating permeability with porosity.

This study shows that two-dimensional DIA pore structure information derived from thin sections relates to velocity and permeability at a given porosity. The knowledge of the pore structure has the potential to reduce uncertainty in permeability and velocity prediction from porosity.

Introduction

Carbonate rocks show often a lack of correlation among porosity, permeability and velocity (Rafavich et al., 1984; Anselmetti and Eberli, 1993, Lucia, 1995; Kenter et al., 1995, 1997; Wang, 1997; Sun et al., 2001; Assefa et al., 2003; Eberli et al., 2003; Baechle et al., 2004; Saleh and Castagna, 2004; Weger et al., 2004; Agersborg et al., 2005; Kumar and Han, 2005; Rossebø et al., 2005; Fabricius, et al., 2007; Lønøy, A. 2006; Ehrenberg, et al., 2006). The high diagenetic potential of carbonates results in intense alteration of the pore structure which can lead to a decrease of "effective" porosity for fluid flow and wave propagation (Schlumberger, 1972, Wang, 1997; Anselmetti and Eberli; 1997; Anselmetti et al., 1998,). Permeability and elastic properties are strongly related to the rock's pore structure. As a result, samples of equal total porosity can exhibit a wide variation of permeability and sonic velocity. The scope of this study is to establish a relationship between p-wave velocity and permeability in relation to the rock's porosity and pore structure under controlled laboratory conditions. The knowledge of the effects of the pore structure on rock properties bears the potential to reduce uncertainty in velocity and permeability prediction also at lower frequency log and seismic scale. For example, permeability appears not to be correlated to the amount of micro-porosity, the so called "ineffective" porosity with respect to fluid flow for some carbonate datasets (Lucia, 1995). Macro-porosity on the other hand appears to be the "ineffective" porosity for acoustic properties (Baechle et al., 2004).

Choquette and Pray (1970) is commonly used to qualitatively describe the carbonate pore types from thin sections. It is a genetic description which can be used for porosity evolution studies; however, it is also used for studies that examine the dominant factors controlling acoustic properties (Wang, 1997; Anselmetti and Eberli, 1993). Both authors show that a qualitative characterization of pore types using Choquette and Pray (1970) enables us to characterize the variable acoustic velocity at a given porosity in carbonates. Qualitative characterizations of carbonate rocks with respect to fluid flow have been first established by Archie (1952), proposing a pore size classification. Lucia (1995) proposed a petrophysical classification of the pore space, separating carbonates in two major groups: those with vuggy pore space and one with interparticle pore space, and he sub-divided the latter into three rock fabric classes with specific porosity-permeability trends: grainstones (class 1), grain-dominated packstones (class 2) and mud-dominated fabric (class 3).

Anselmetti and Eberli (1993) showed in a laboratory study significant velocity deviations in carbonate rocks from the Wyllie's time-average velocity (Wyllie et al., 1956) and they attributed the velocity deviations to rocks with different dominant pore types, which makes the rock either more stiff (faster) or less stiff (slower) than the Wyllie's time-average velocity. Furthermore, correlations between velocity deviation from Wyllie's time-average velocity log response provide permeability trends at log scale, due to pore type effects (Anselmetti and Eberli, 1999). Whereas rocks with dominant interparticle and micro-porosity follow Wyllie's time average velocity, rocks dominated by intraparticle and moldic pore types show positive deviations from Wyllie's time average velocity (Anselmetti and Eberli, 1993). Qualitative pore type descriptions, however, often lack exact relations between velocity and porosity due to either (a) the difficulty of defining a dominant pore type from a mixture of pore types or (b) the modifying effects of minor pore types. In contrast, quantitative digital image analysis has been successfully used to relate pore structure effects to fluid flow (Anselmetti et al., 1998), and acoustic properties (Weger et al., 2004), or to relate acoustic properties to permeability (Baechle et al., 2004).

One major unsolved problem in rock physics is to use acoustic data to predict permeability in a quantitative way. The aim of this study is to establish a quantitative link between velocity and permeability through porosity in combination with pore structure derived from digital images of thin sections. The goal is achieved by determining quantitative digital image analysis parameters, which characterize pore structure and hereby relate velocity to permeability at a given porosity.

Dataset and method

Ultrasonic velocity, permeability and porosity are measured on 138 carbonate samples of three locations: (a) Bioclastic limestones and dolomitized equivalents of Neogene age cored on the Marion Plateau, offshore northeastern Australia, during Ocean Drilling Program Leg 194 (Isern et al., 2002; Ehrenberg et al., 2006), (b) platform and reefal limestone of Early Cretaceous age from a hydrocarbon exploration well on-shore Middle East, and (c) shallow water platform and reefal limestone of Neogene age, offshore South-East Asia. In addition, I include samples from the CSL rock physics database for which porosity, velocity and thin sections are available. The physical properties of the selected 109 limestones and dolostones from the CSL rock physics database were measured by Flavio Anselmetti and Xavier Janson (Xavier, 2002; Anselmetti and Eberli, 1993). Prior to velocity measurements, the samples are fully saturated in water under vacuum (0.08 MPa) for 48h. The velocity measurements are carried out at effective confining pressures of 2 to 40 MPa and pore pressures of 2 MPa. The data plots in this chapter show velocity measured at 20 MPa effective confining pressure. The mineralogy is determined by XRD measurements and by grain density measurements. A representative thin section of each sample is prepared from a small core plug cut-off.

I qualitatively describe the thin sections using pore fabric classification of Lucia (1995) and the pore type classification of Choquette and Pray (1970). The investigated samples are dominated by microporosity, intercrystalline, interparticle, moldic or vuggy porosity.

Quantitative digital image analysis (DIA) is performed on digital images covering the entire thin section, 1" or 1.5" in diameter. DIA incorporate measurements of the pore size and the pore shape. The image acquiring procedure is described in detail by Weger (2007) and Weger et al. (in press). The images are processed in the HSV color bands. Binarization of the color image into a black and white image segments black color pixels characterizing macro-pores and white color pixels characterizing grains and micro pores.

Pore shape and pore size definitions

In previous studies, micro-porosity definition spans a wide range of pore sizes. The widely cited carbonate classification of Choquette and Pray (1970) define the size of micropores as 1/16 of a micrometer or smaller. Pittman (1971) defines micro-pores to be smaller than one micron in diameter. Cantrell and Hagerty (1999) use semi-quantitative image analysis and define micropores to be smaller than 10 microns in diameter. Anselmetti et al. (1998) define the boundary between macro-porosity and micro-porosity as ”pore area of 500 square microns, which translates to a pore length of approximately 20 microns”. With our microscope lens of 1x and the thin section thickness of around 30 microns, macro-porosity by default excludes all pores smaller than 30 microns in length (thin section thickness) and 6 microns (pixel resolution) in diameter perpendicular to the thin section orientation. Macro-pores are characterized by bright colors of the blue epoxy filling the pore space (Fig. 3, Chapter 1). I define micro-porosity as the image macro-porosity subtracted from the plug porosity.

Well-established parameters relevant for characterizing the pore network in porous media at different scales include tortuosity from resistivity data, specific surface from BET absorption data and/or hydraulic radius from mercury injection data. The DIA method described here quantifies the pore structure in digital images at scales relevant for fluid flow and elastic properties, from microns to cm-scale. I use three DIA parameters to characterize the macro-pores: (1) The dominant pore size of the macro-pores (DOMsize) defined by Weger (2007). It is the pore size (expressed in area) at the 50% exceedance probability in a cumulative pore area sum curve. (2) The pore shape factor γ that describes the roundness of individual pores. It is calculated using the definition of Anselmetti et al. (1998). (3) The perimeter over area (PoA), which is a measure of the complexity of the carbonate pore system, expressed as the 2D equivalent of the specific surface in 3D pore networks (Weger et al., 2004; Baechle et al., 2004). In a homogeneous, isotropic porous medium, the specific surface is related to the permeability variations at a given porosity (Schlumberger, 1972).

Theoretical equations

The Wyllie time average velocity is calculated using a P-wave mineral velocity; Vp_{min} of 7370 m/s and of 6540 m/s for dolomite and calcite, respectively. The heuristic Wyllie time average velocity is calculated using the following equation (Wyllie et al., 1956):

$$\frac{1}{Vp} = \frac{1-\phi}{Vp_{\min}} + \frac{\phi}{Vp_{fLuid}} \qquad (1)$$

The velocity deviation is calculated as a percentage difference between measured P-wave velocity and Wyllie's time average velocity.

I calculate the pore space stiffness K_{por} as a unique quantification of the stiffening and softening effect of the carbonate pore structure on velocity at any given porosity. I use the saturated rock compressibility, which is the reciprocal of the saturated rock bulk modulus (K_{sat}) and the mineral bulk modulus (K_{min}) and the porosity (Ø) to define the pore space stiffness (K_{por}) after Walsh (1965), Zimmerman (1991), and Mavko and Mukerji (1995):

$$\frac{1}{K_{dry}} = \frac{1}{K_{\min}} + \frac{\phi}{K_{por}} \qquad (2)$$

Since porosity and the mineral bulk modulus is known, the pore space stiffness can be calculated by deriving K_{dry} from sonic velocity:

$$K_{dry} = (Vp^2 - \frac{4}{3}Vs^2)\rho \qquad (3)$$

where,

Vp = compressional wave velocity, Vs= shear wave velocity and ρ = density.

K_{por} has the same functional formulation in the saturated state and the dry state except that in the saturated state we have to include a fluid term "F" (Mavko and Mukerji, 1995):

$$F = \frac{K_{\min} K_{fluid}}{K_{\min} - K_{fluid}} \qquad (4)$$

$$K_{por(sat)} = K_{por(dry)} + F \qquad (5)$$

In the following, when I refer to K_{por}, I mean the saturated pore space stiffness. Solving Equation 1 for the pore space stiffness K_{por}:

$$K_{por} = \frac{\phi K_{\min} K_{sat}}{K_{\min} - K_{sat}} \qquad (6)$$

The pore space stiffness K_{por} uniquely defines velocity variation at a given porosity. However, constant pore shape is not equivalent to constant pore space stiffness K_{por} since all the pores elastically interact with each other (Mavko and Mukerji, 1995).

Effects of pore structure on permeability

Macro-porosity displays a much better correlation to permeability than total plug porosity. A plot of measured porosity versus permeability shows a weak correlation ($r^2=0.14$) (Fig. 1a). The permeability shows a large scatter of up to 4 orders of magnitude in permeability in the porosity range between 10% and 25%. Excluding micro-porosity from a correlation with permeability reduces permeability uncertainty to 2½ orders of magnitude in permeability (Fig. 1b), when compared to the porosity-permeability cross-correlation trend. The log-normal correlation increases significantly when permeability is plotted against the macro-porosity ($r^2=0.53$), compared to porosity-permeability correlation (Fig. 1a and 1B).

At a given porosity, I derive a wide spectrum of PoA values from 10 μm^{-1} to over 220 μm^{-1}, which is an indication of the wide range of pore structure variations over the entire porosity range (Fig. 2a). The dominant pore size also varies widely, ranging from a pore size of a few μm^2 to pore sizes over 1000 μm^2 at a given porosity (Fig. 2b). The PoA values range from 10 μm^{-1}, characteristic for relative "simple" pore structures, to PoA values of 200 μm^{-1}, indicative for highly tortuous and complex pore networks. PoA and DOMsize are porosity independent. At a given porosity of around 30%, a packstone dominated by microporosity shows a high PoA of 150 μm^{-1} (Fig. 2c) whereas at the same porosity are recrystallized dolostone with vuggy-intercrystalline porosity displays a PoA of 28 μm^{-1} (Fig. 2d)

Table 1: Description of the porosities used for correlation with velocity and permeability.

Property	**Measurement/Calculation**
Plug porosity or porosity	Standard laboratory measurement of porosity with helium porosimeter
Macro-porosity	Measured image macro-porosity, derived from digital image analysis on a thin section image
Micro-porosity	Macro-porosity subtracted from plug porosity

There exists no direct correlation between permeability and PoA (Fig. 3a). The ratio of PoA, a two dimensional equivalent of the specific surface, shows permeability cut-off values in a plot against permeability but no trend with permeability (Fig. 3a). An increasing PoA ratio decreases the maximum permeability of the samples. There exists an upper bound of permeability for a given PoA value. For example, all samples with a PoA value above 60 μm^{-1} have permeability below 100 mD. Furthermore, all samples with a PoA value above 110 μm^{-1} have a permeability below 15 mD. I attribute the lack of correlation trend describing the relationship between permeability and PoA ratio to the effects of disconnected pores and varying porosity. For example, a dolostone with vuggy and intercrystalline porosity and a dolostone with moldic and intercrystalline porosity have an apparent simple pore system but also a low permeability due to the vuggy and moldic pores present in the sample, which are less well connected to the pore network.

A plot of permeability versus DOMsize shows no clear trend (Fig. 3b). However, the permeability-DOMsize relationship displays a maximum permeability for a given DOMsize, the DOMsize forms a lower bound of permeability at any given DOMsize (Fig. 3b). For example, all samples which have smaller DOMsize than 200 μm^2 have permeabilities below

100mD. Most samples which show a PoA above 60 µm^{-1}, as indicated by the white dots in Figure 3, display a DOMsize below 200 µm^{2} (Fig. 3).

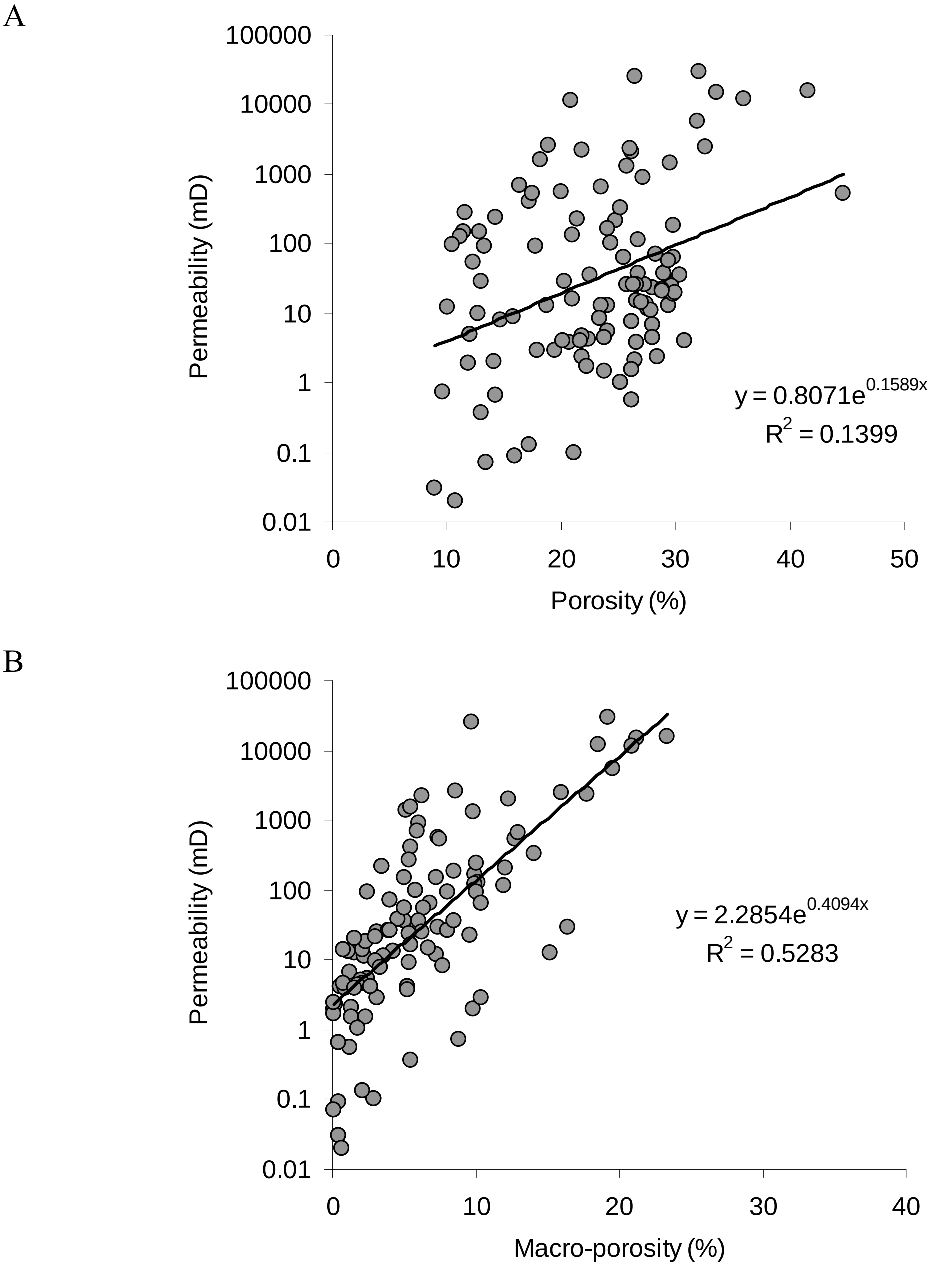

Fig. 1: (A) Porosity shows a weak correlation with permeability in our dataset (r^2=0.14). (B) Macro-porosity appears to control permeability in our dataset, given the higher correlation coefficient using an exponential regression trendline (r^2=0.53). Porosity and macro-porosity description in Table 1.

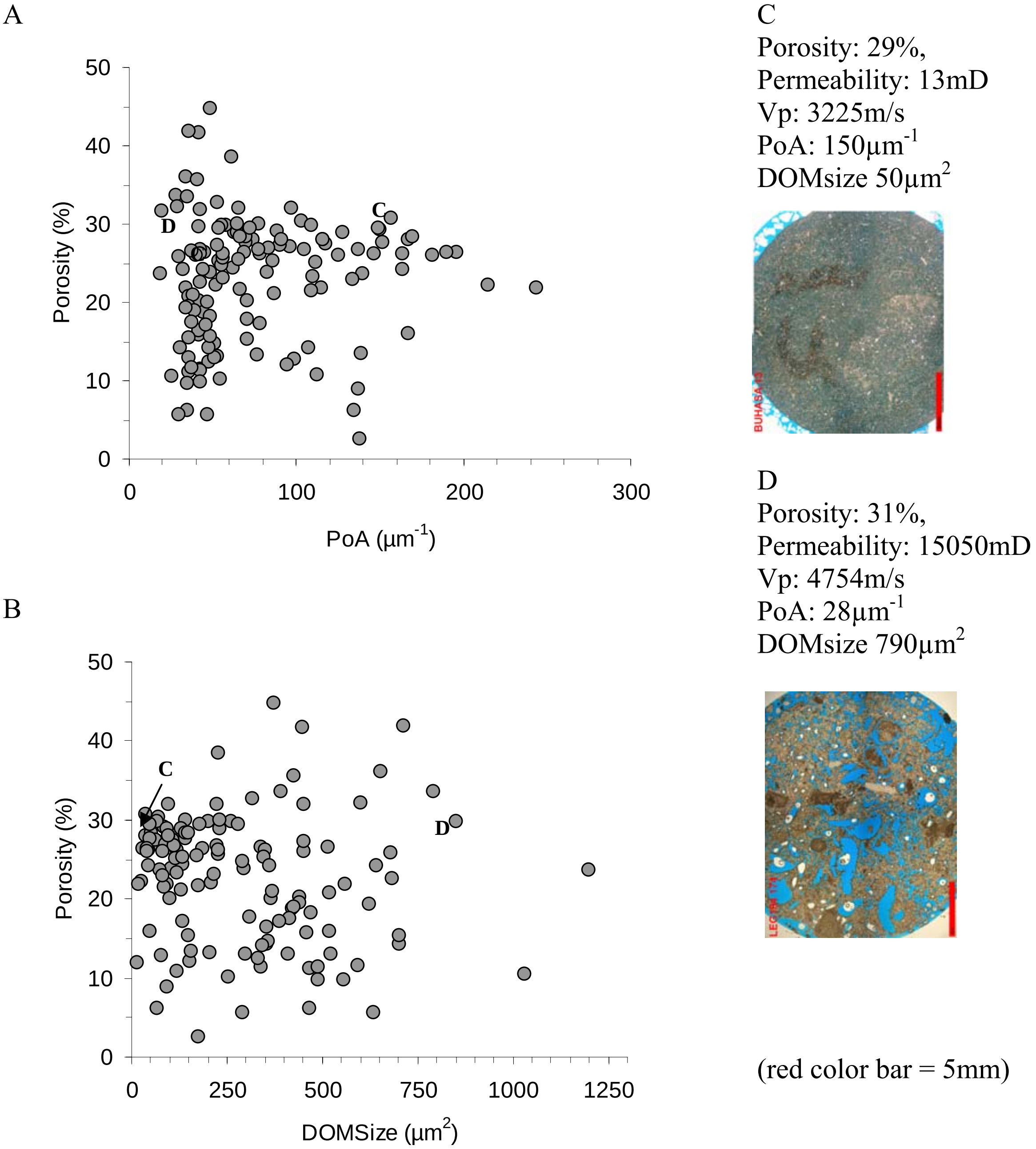

C
Porosity: 29%,
Permeability: 13mD
Vp: 3225m/s
PoA: 150μm^{-1}
DOMsize 50μm^2

D
Porosity: 31%,
Permeability: 15050mD
Vp: 4754m/s
PoA: 28μm^{-1}
DOMsize 790μm^2

(red color bar = 5mm)

Fig. 2: Plot of porosity versus PoA (A) and plot of porosity versus DOMsize (B). The complexity of the pore system (as indicated by PoA) and the dominant pore size (as indicated by DOMsize) are independent of porosity (seen in sample C and D).

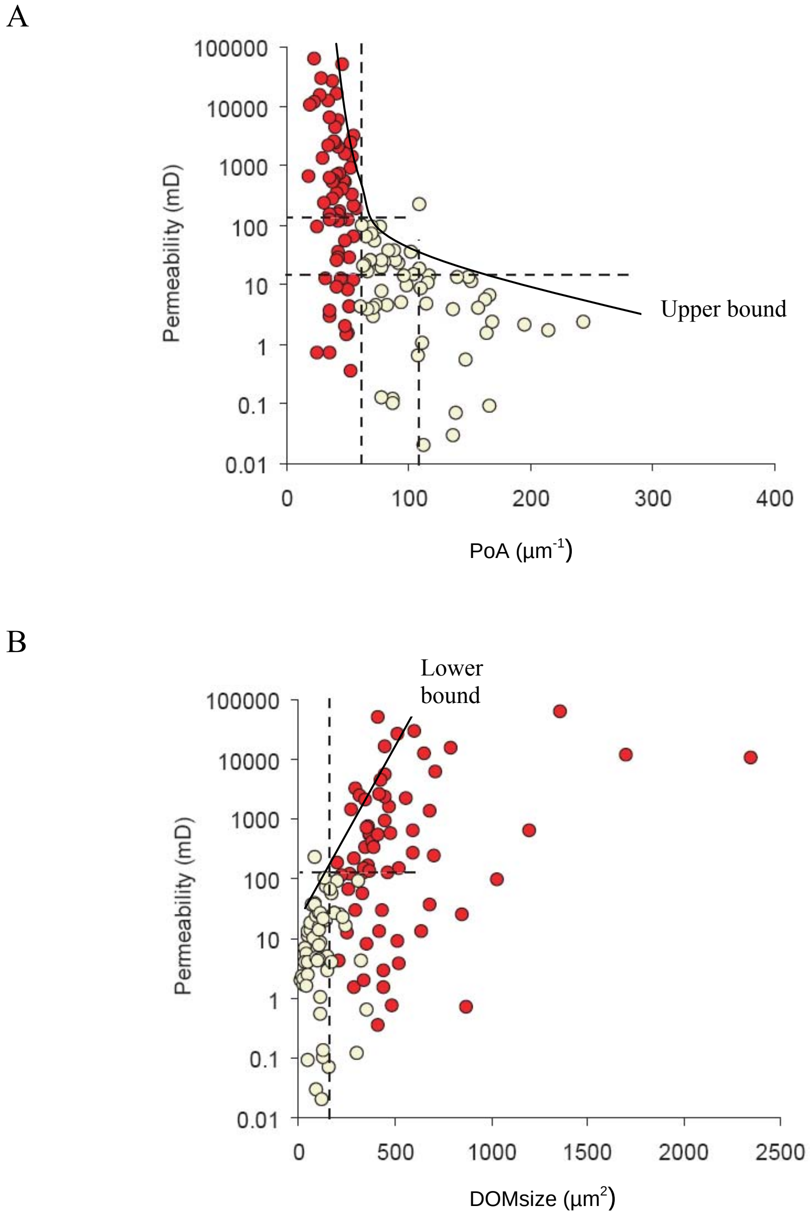

Fig. 3: (A) Plot of permeability versus PoA and (B) plot of permeability versus DOMsize. There is no good correlation between those two macro-pore DIA parameters and permeability. Samples marked by the white color have a PoA smaller than 60 microns. There appears to be an upper bound in the permeability-PoA relationship and lower bound in the permeability-DOMsize relationship.

A log-log plot of dominant pore size (DOMsize) and the 2D specific surface (PoA) displays a strong log-log linear relationship between the two measured macro-pore DIA parameters (Fig. 4). A power regression analysis shows good correlation between DOMsize and PoA with a correlation coefficient r^2=0.89 (Fig. 4). The samples with the maximum permeabilities have relative large dominant pores (DOMsize) and low PoA values (high permeability = warm colours).

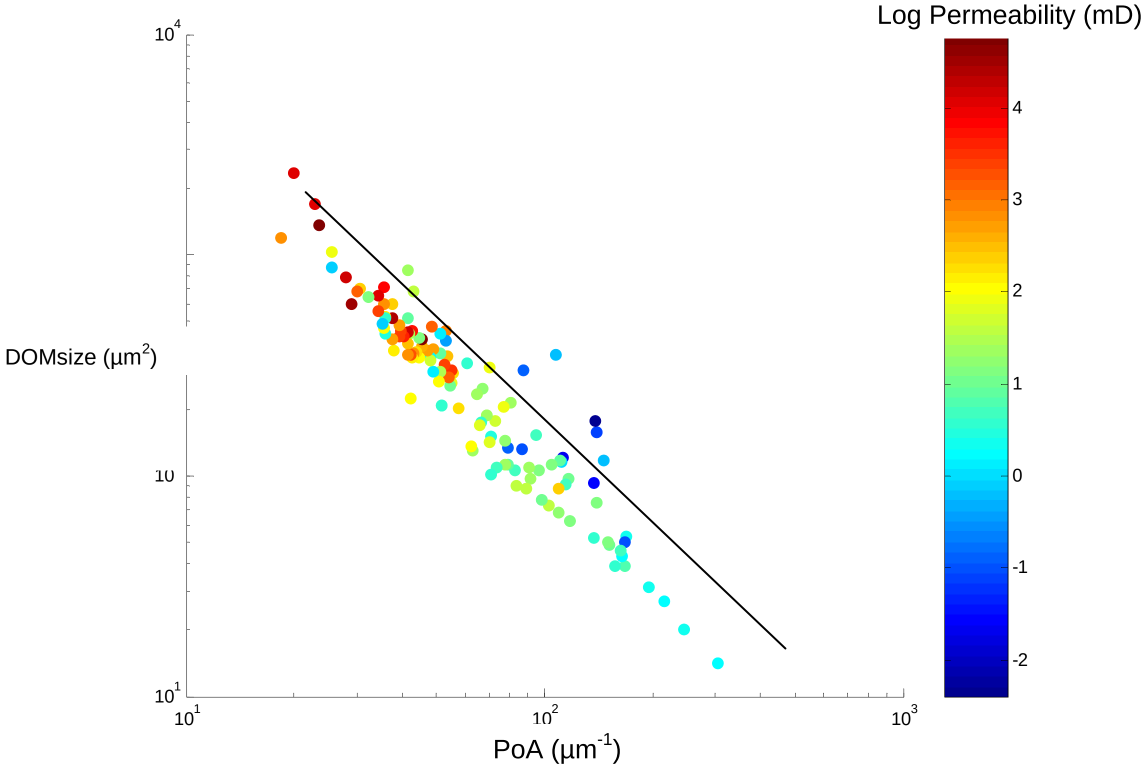

Fig. 4: A log-log regression trendline shows good correlation (r^2=0.89) between dominant pore size (DOMsize) and perimeter over area ratio (PoA). DOMsize versus PoA shows highest permeability in samples with large dominant pores & simple pore system (high DomSize and low PoA).

Effects of pore structure on velocity

The compressional velocity span from 2900 m/s to 6300 m/s and the porosity covers a range from 3% to 50%. The cross-plot of compressional velocity and porosity of pure carbonate samples show a large scatter of up to 2500 m/s at 26% porosity (Fig. 5a). Most of the samples fall slightly above the Wyllie time-average velocity trend. Incorporating the macro-pore shape information, we are able to separate the velocity-porosity scatter into two distinct different groups of samples: The white colored dots in Figure 5a indicating samples smaller than 60 μm^{-1} and P-wave velocity below the velocity-porosity best fit linear trendline, whereas the samples larger 60 μm^{-1} show velocities above the best fit linear porosity-velocity trendline (same color coding as in Figure 3). Using micro-porosity from DIA analysis, instead of plug porosity, significantly improves the correlation coefficient between porosity and velocity from r^2=0.54 to r^2=0.83 (Fig. 5a and 5b). The macro-porosity alone displays a poor correlation with velocity.

In order to evaluate which DIA parameter indicates best the pore texture effect on velocity variation at a given porosity, I cross-plot the same macro-pore parameters as used for permeability correlation (Fig. 6). Using a linear regression analysis, the dominant pore size (DOMsize) shows the weakest correlation (r^2=0.29) with the P-wave velocity deviation from Wyllie's time average velocity (Fig. 6a). The pore shape factor γ and 2D specific surface (PoA) show better correlation coefficients r^2=0.36 and r^2=0.44, respectively (Fig. 6b and 6c). The macro-porosity shows the best control on the P-wave velocity deviation from Wyllie's time average velocity, with a correlation coefficient of r^2=0.57 (Fig. 6d).

Plotting the velocity deviation from Wyllie times average equations versus the macro-porosity at a velocity interval between 4000 and 5000 m/s, reveals that the amount of measured macro-porosity shows a good correlation (r^2=0.81) to the velocity deviation (Fig. 7).

Single parameter linear regression analysis equations and linear multiple regression analysis equations are applied to predict P-wave velocity. I use porosity and a range of DIA parameters (micro-porosity, PoA, pore shape factor γ and DOMsize) as input. The results of the velocity predictions are shown in Table 2 as root mean square error (RMSE) and correlations coefficient (r^2) between measured and predicted velocity.

Linear regression analysis shows that out of all DIA parameters used, only micro-porosity results in an improved prediction of P-wave velocities (r^2 = 0.83), in comparison to using porosity alone (r^2 = 0.54) (Table 2). Using an equation derived from a multiple regression analysis of velocity and porosity, micro-porosity, pore shape factor γ, PoA and DOMsize

A

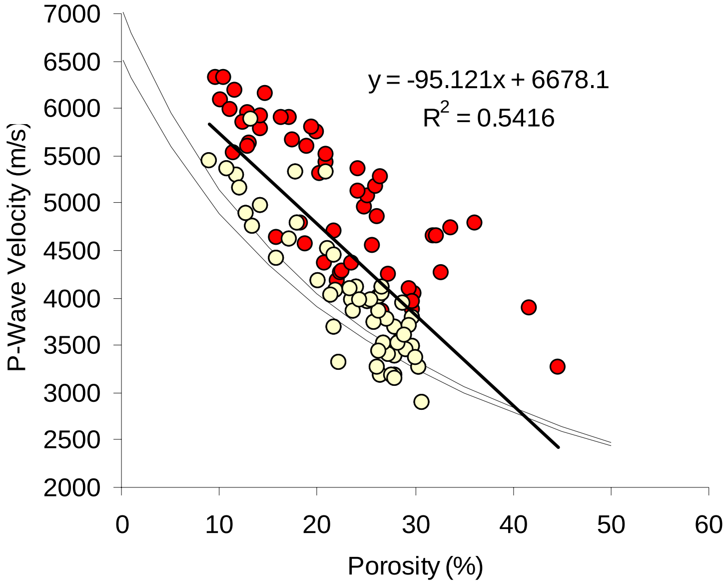

B

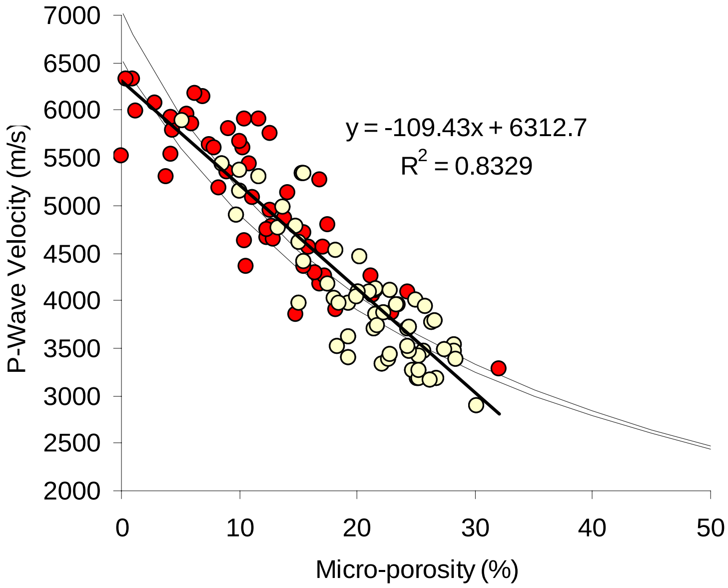

Fig. 5: (A) Plot of porosity versus P-wave velocity. The velocity shows a positive deviation from Wyllie time average velocity (calcite and dolomite velocity curves plotted). (B) Plot of micro-porosity versus velocity. The bold straight line is a line regression trendline. Micro-porosity appears to be a better control on velocity than porosity, the correlation coefficient increase from r^2=0.54 to r^2=0.83. The Wyllie time average velocity curve for dolostone and limestone follow the velocity versus micro-porosity data rend. Porosity and micro-porosity description in Table 1.

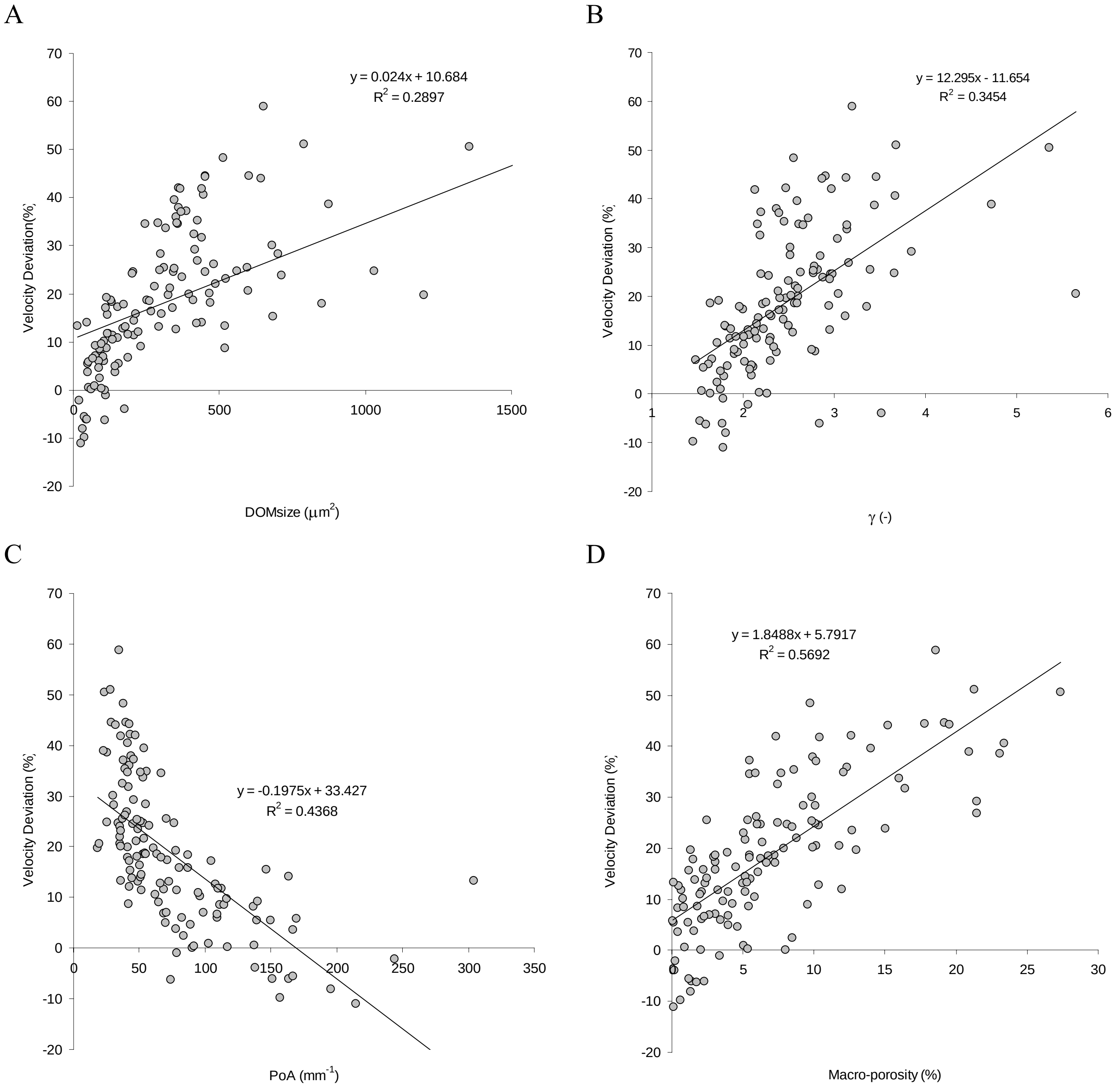

Fig. 6: The P-wave velocity deviation from Wyllie's time average velocity shows an increase in correlation when plotted against (A) DOMsize to (B) pore shape factor γ to (C) PoA and (D) macro-porosity. Macro-porosity description in Table 1.

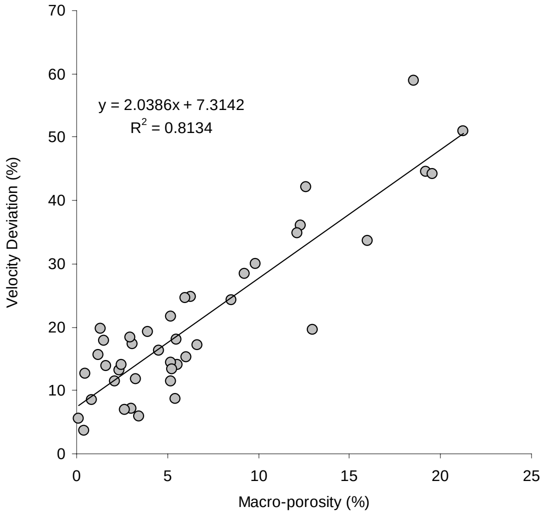

Fig. 7: The macro-porosity shows a good correlation with the P-wave velocity deviation from Wyllie's time average velocity. The plot displays only samples with velocities between 4000ms/ and 5000m/s.

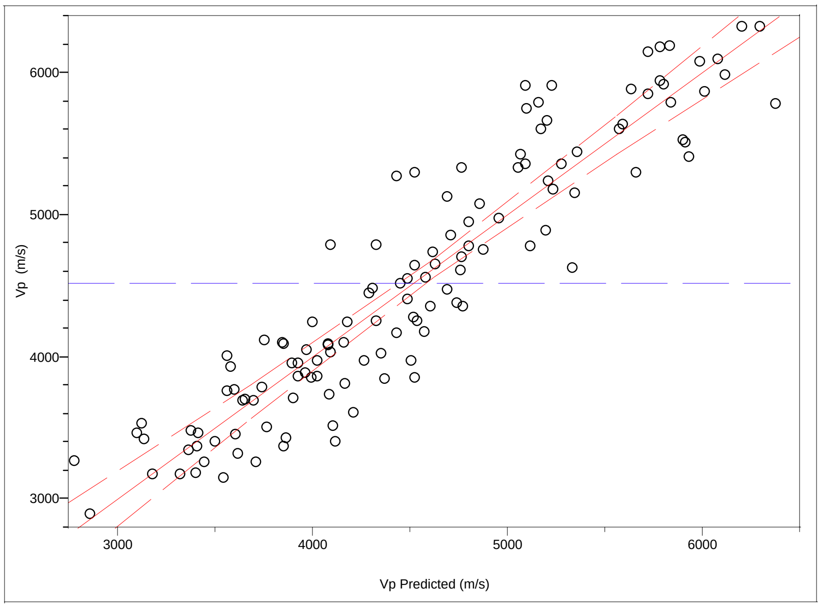

Figure 8: Plot of measured versus predicted P-wave velocity (Vp). The predicted velocity is derived from a multiple regression analysis using the following input parameters: (1) pore shape factor γ, (2) DOMsize and (3) PoA and (4) micro-porosity and (5) plug porosity.

yields a good correlation coefficient ($r^2 = 0.87$) and a good root mean square error (RMSE = 338 m/s**)** between measured and predicted velocity (Table 2, Figure 8). Using micro-porosity and porosity, in combination with macro-pore DIA parameters, strongly reduces the uncertainty in velocity prediction. It is important to recognize that porosity and the details of the pore structure do all influence the acoustic properties in carbonates.

Table 2: Root mean square errors and correlation coefficients between predicted p-wave velocity and measured p-wave velocity. The annotation "x" marks the physical properties used as linear regression analysis input parameters.

Vp RMSE	Vp r^2	Micro-porosity	Plug porosity	PoA	γ	DOMsize
338	**0.87**	X	X	X	X	X
342	0.86	X	X	X	X	
346	0.86	X	X	X		
364	0.84	X	X			
378	**0.83**	X				
617	0.54		X			
843	0.15			X		
883	0.07				X	
876	0.08					X

Relationship between microporosity, pore space stiffness and velocity

From all measured and calculated DIA parameters micro-porosity correlates best with velocity, Thus, I relate the amount of micro-porosity to the pore space stiffness K_{por}, which quantifies the bulk modulus-porosity scatter. To establish this relationship, I performed digital image analysis on 109 carbonate samples of two formations from the CSL database and added it to my analysis, in order to increase the range of physical properties to include samples with higher porosities and lower velocities and hereby reducing the database bias.

The porosity of the CSL database samples range from 2% up to 55% and the compressional velocity varies from 2200 m/s to 6200 m/s.

The pore space stiffness K_{por} is independent of porosity. However, our experimental data shows that the maximum K_{por}-value decreases with increasing porosity. There exists an upper bound of the pore space stiffness K_{por} at a given porosity (Fig. 9); the maximum pore space stiffness K_{por} ~ 36 at 10% porosity decreases to a K_{por} of ~ 15 at 50% porosity.

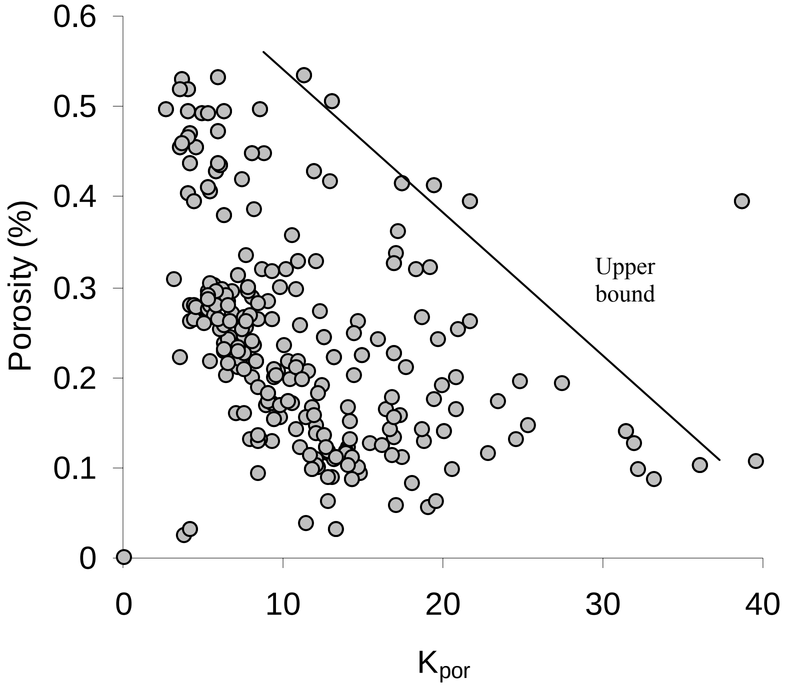

Fig. 9: Pore space stiffness (K_{por}) shows a large scatter at any given porosity. The upper bound of the pore space stiffness appears to decrease with increasing porosity.

The large scatter and resulting low correlation of a velocity-porosity cross-plot in Figure 5a can be improved by introducing another parameter, apart from porosity, which captures the pore texture. The P-wave velocity shows a good straight line log-normal regression trend with a correlation coefficient of r^2=97 when plotted against the porosity over the pore space stiffness (ϕ/K_{por}), which is the 2nd term in Equation 2 (Fig. 10). At higher P-wave velocities we see a misfit between the best fit line and the measured data. Further, in Figure 11, I observe also a good correlation between the squared P-wave velocity (Vp^2) and squared S-wave velocity (Vs^2) for our dataset (r^2=0.95). The average Vs^2/Vp^2 ratio from the straight line linear regression shows a value of r^2=0.28 (Fig. 11). The strong correlation between ϕ/K_{por} and Vp in Figure 10 can be attributed to the low variability in the Vs^2/Vp^2 ratio.

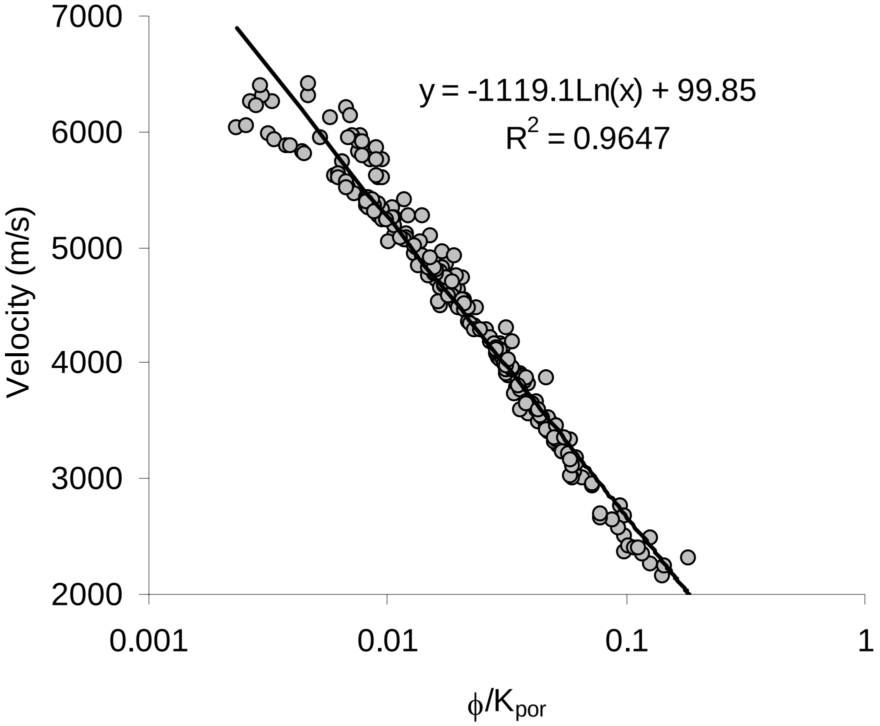

Fig. 10: Plot of P-wave velocity versus porosity over pore space stiffness (ϕ/K_{por}) shows a very good logarithmic regression trend with a correlation coefficient of r^2 = 0.97.

Contours of two normalized pore space stiffness (K_{por}/K_{min}) trends are graphically presented in a normalized bulk modulus versus porosity cross plot (Fig. 12). The pore space stiffness and the bulk modulus are normalized by the mineral modulus (K_{min}). In Figure 12, red dots show normalized bulk moduli of recrystallized dolostones dominated by intercrystalline-vuggy porosity, whereas the blue dots mark limestones dominated by microporosity. Limestones dominated by microporosity show normalized bulk moduli grouping around the contour line of 0.1. In contrast, recrystallized dolostones with intercrystalline-vuggy porosity show higher normalized bulk moduli, grouping around the contour line of K_{por}/K_{min} = 0.1.

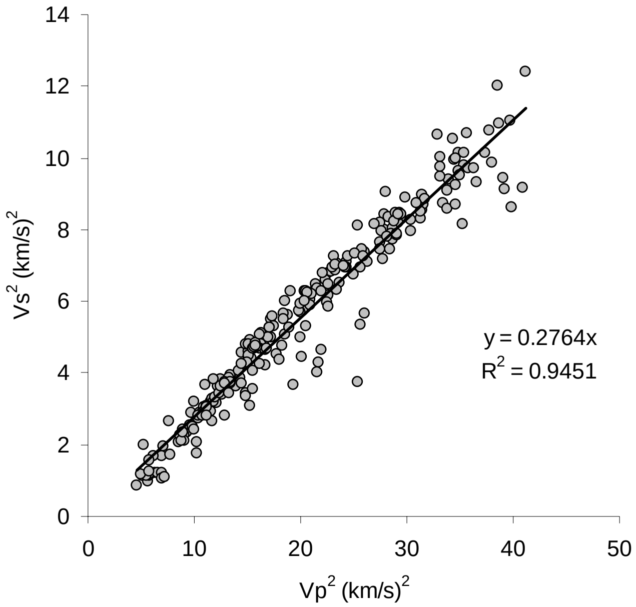

Fig. 11: Plot of squared P-wave velocity versus squared S-wave velocity shows a good correlation (r^2=0.95).

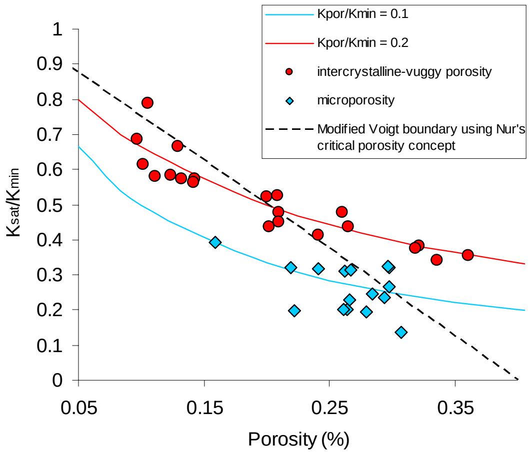

Fig. 12: (A) Plot of normalized bulk modulus (K_{sat}/K_{min}) versus porosity. Limestones dominated by micro-porosity show lower normalized pore space stiffness (K_{por}/K_{min}) than recrystallized dolostones with dominant intercrystalline-vuggy porosity.

Micro-porosity derived from DIA of thin sections shows a good correlation to the "porosity over pore space stiffness" (ϕ/K_{por}), the 2nd term in Equation 2 (Fig. 13). The 2nd order polynomial regression trend line is forced to zero and it shows a good correlation between the two parameters with r^2 = 0.88 (Fig. 13).

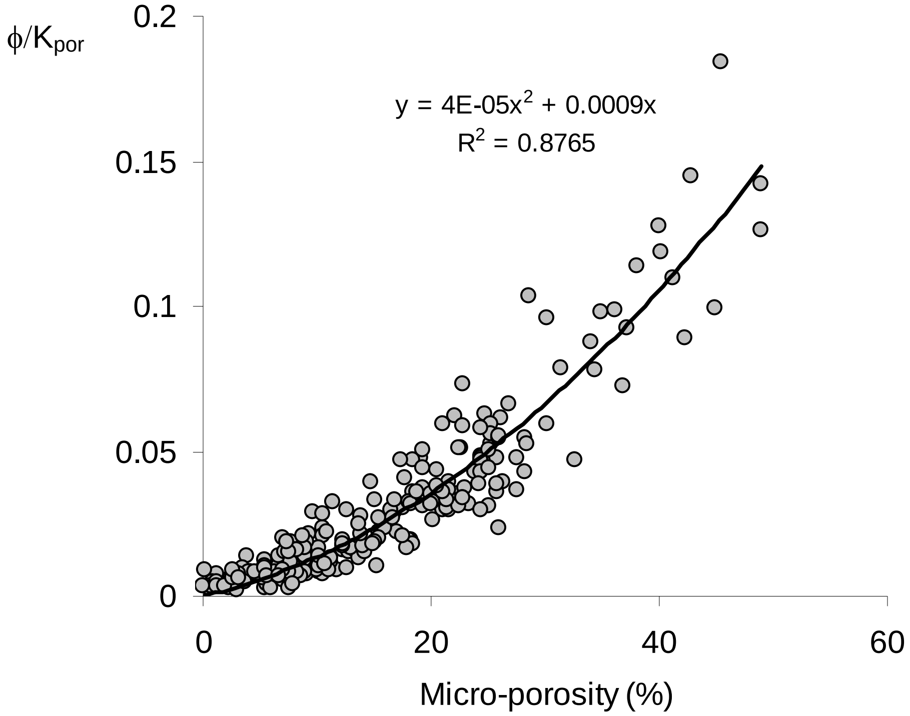

Fig. 13: Micro-porosity versus porosity over pore space stiffness (ϕ/K_{por}). The 2nd order polynomial regression trend is forced through zero and shows a good correlation between the two parameters with $r^2 = 0.88$. Micro-porosity description in Table 1.

The pore space stiffness (K_{por}) uniquely identifies compressibility variations at a given porosity as seen in the normalized bulk modulus versus porosity plot in Figure 14a. The bulk moduli with similar values of ϕ/K_{por} is shown by the background color zones (Fig. 14a). The pore space stiffness K_{por} of the entire dataset ranges from “softer” rocks having values below 0.1, to “stiffer” rocks with values of up to 0.4 (Fig. 14a). Low “porosity over pore space stiffness” (ϕ/K_{por}) is a good indicator to characterize samples with a high amount of micro-porosity and low permeability (Fig. 14b). Further, samples with stiff pores and high “porosity over pore space stiffness” (ϕ/K_{por}) values show high permeabilities (Fig. 14b).

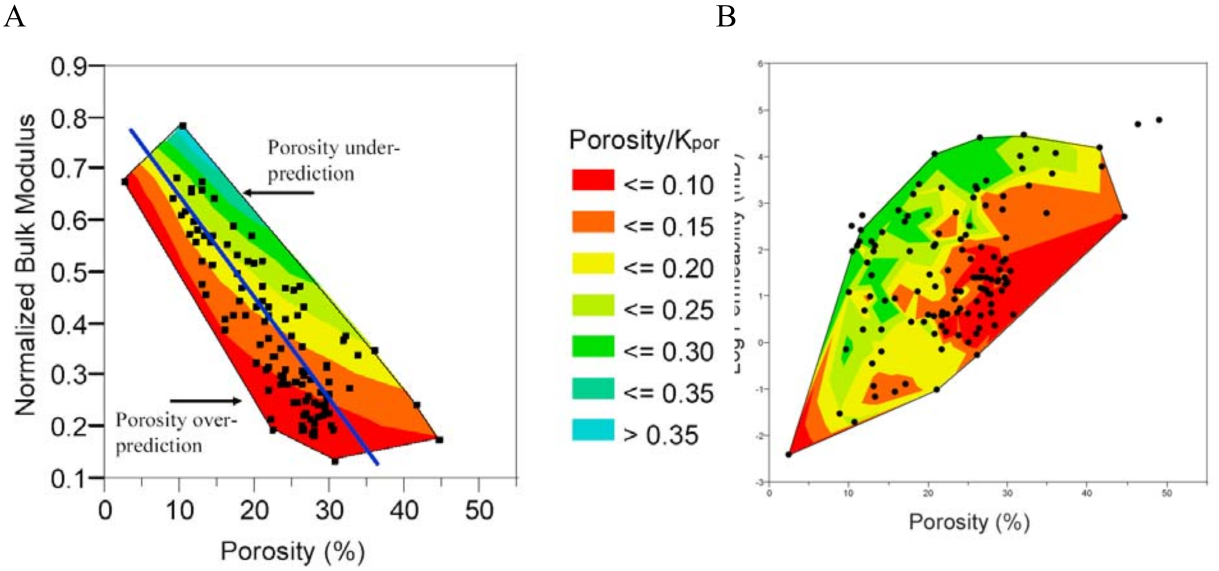

Fig. 14: (A) A plot of porosity versus normalized bulk modulus with color annotation of normalized pore space stiffness (K_{por}). K_{por} uniquely identifies different compressibility at a given porosity. (B) A plot of porosity versus permeability with color annotation of pore space stiffness (K_{por}) shows that K_{por} has the potential to separate low permeability samples from high permeability samples at a given porosity.

As seen in Figure 13 and Table 2, micro-porosity is one important factor for effectively reducing velocity at a given porosity, whereas, the macro-porosity is mostly ineffective for P-wave velocity and it is therefore relating well with velocity deviation from Wyllie's time average velocity (Fig. 6d). Furthermore, a porosity-permeability plot with color annotations of pore space stiffness shows that the "porosity over pore space stiffness" (ϕ/K_{por}) does not only quantify the velocity-porosity scatter but also the permeability-porosity scatter, hereby indicating the knowledge of the macro-porosity and micro-porosity in additional to porosity is an important factor to predict both properties, permeability and velocity (Fig. 14a and 14b).

Conclusions and implications

Micro-porosity, in combination with DIA parameters derived from macro-pores, reduces uncertainties in both velocity-porosity and permeability-porosity trends. Samples with high amounts of micro-porosity follow closely the Wyllie's time-average velocity-porosity trend line and they are related to low permeability rocks. It is important to separate the porosity into macro-porosity and micro-porosity in order to obtain better correlation coefficients for permeability and velocity prediction from porosity. The correlation between micro-porosity and velocity is much higher and better than the correlation between porosity and velocity. Correlation of permeability to image derived macro-porosity reduces the uncertainties in permeability prediction by at least one order of magnitude. Pore structure parameters, like DOMsize and PoA, calculated only from image macro-porosity without incorporating total plug porosity can be used as cutoff values to constrain maximum velocity and permeability values at given porosity ranges.

Furthermore, pore space stiffness at given porosity (ϕ/K_{por}) quantifies velocity deviation caused by pore texture changes. Contours of carbonate pore stiffness follow a non-linear path in the moduli-porosity space. Micro-porosity appears to have a dominant effect on reducing rock stiffness, whereas vuggy porosity creates high apparent rock stiffness at given porosity. Recrystallized rocks with vuggy and intercrystalline porosity show a normalized pore space stiffness value of 0.2 compared to high micro-porosity limestones with a normalized pore space stiffness value of around 0.1. These results indicate that the non-linear bulk moduli - porosity models, like a model of constant pore stiffness K_{por}, is superior to linear models in characterizing specific carbonate pore types. Furthermore, low pore space stiffness K_{por} derived from measured porosity and velocity indicates low permeability rocks in a porosity-permeability transform at given porosity. These findings point towards the potential for a combined pore structure - porosity inversion in carbonate rocks, which could result in better reservoir prediction and development.

Chapter 3

PREDICTION OF SONIC VELOCITY FROM THIN SECTIONS

Abstract

The elastic moduli of a rock are affected by three main factors: pore fluid, rock framework and pore space. In carbonate rocks, the latter two factors are a function of the depositional environment and the diagenetic history. Cementation, recrystallisation and dissolution processes can change the mineralogy and texture of the original framework and thereby alter the original grain-to-grain contacts and/or occlude pore space. Dissolution processes can enlarge interparticle pore space or dissolve grains entirely, thereby increasing porosity. These diagenetic alterations and associated changes in the rock frame and pore structure result in a wide velocity range at a given porosity.

It is a challenge to describe carbonate rocks, with their complex pore structures and wide range of pore sizes and pore shapes in terms of their elastic behavior. Hamilton et al. (1956) were the first to observe a positive correlation between pore size and velocity in carbonate sediments. More recently, qualitative rock physics studies on cores from Great Bahama Bank showed how porosity and pore type are closely related to the elastic behavior of the rock and its sonic velocity (Eberli et al., 2003). Samples containing moldic and intraparticle porosity revealed a faster velocity than samples containing micro-moldic porosity and micro-porosity. In recent years, several theoretical rock physics models, in addition to the experimental work, have dealt specifically with the problems surrounding elastic behavior in carbonates. These models take into account the effects of porosity and pore-structure variations on elastic properties (Brie, 2001; Kumar at al., 2005; Sun et al., 2006). However, there is still a lack in linking geometrical model parameters, such as aspect ratio or the frame flexibility factor, to observable pore structure in the rock.

A better calibration of rock-physics model parameters to pore types is required to improve interpretation of seismic inversions and AVO effects. Here we introduce an approach that calibrates the rock-physics model input parameters with pore-size

fractions derived from quantitative digital image analysis of thin sections. Specifically, the measured amounts of micro-porosity and macro-porosity, in addition to the geometry of the macro-pores, are incorporated into the differential effective-medium model to compute the velocities of 250 carbonate samples under dry and water-saturated conditions. These pore-size fractions also play a major role in the flow dynamics and are, thus, a link to the permeability. Our model prediction matches the velocity-porosity trends seen in laboratory measurements very well. This corroborates our hypothesis that compliant micro-pores have a strong softening effect on the sonic velocity of porous carbonates, whereas the amount of macro-pores is positively correlated with increasing velocity deviation from Wyllie's time average velocity.

Porosity and pore-space description

The first step towards integrating realistic pore-geometry parameters into rock-physics modeling of carbonates is to obtain a quantitative description of the pore space. Thin section analysis is a widely available technique for capturing a 2-D description of the pore space. Carbonates characteristically have large variations in shape and size of pores within a single sample, variations that can be captured by quantitative analysis of thin-section photographs (Anselmetti et al., 1998; Weger et al., in press).

Digital image analysis (DIA) was performed on thin sections obtained from an end piece of the core-plug sample that is used in the experimental acoustic-velocity analysis. To visually separate the rock from the pore space, the rock's pore space was saturated with blue epoxy. A full thin-section digital image at a resolution of 6 to 7 microns per pixel consists of several digital images that have been stitched together. The full color image is segmented into a black and white binary image, with the white features representing the pore space. The imaged pore space is macro-porosity and represent pores, in the case of optical light microscopy (OLM), that are through-going pores in a straight line from top to bottom of the thin section (pores > 30 microns). Subtracting the amount of this macro-porosity from the total plug porosity determines the micro-porosity. SEM mosaics covering the entire thin section allow more detailed quantitative description of the pore space (Rossebø et al., 2005), as the SEM analyzes only the top few microns of the thin section, and, as such, SEM image resolution is very close to detected pore resolution. Figure 1 shows DIA of the pore space on a limited dataset (26 samples) using both OLM and scatter electron microscopy (SEM) images with the same image resolution of 6.4 microns. The difference between SEM and OLM porosity estimates is caused by the pore fraction between 6 and 30 microns. Micro-porosity is hereby defined as porosity in pores that are below the resolution limit of the specific image acquiring technique being used. The difference between plug porosity and SEM porosity is due to the fraction of the pore space smaller than 6 microns.

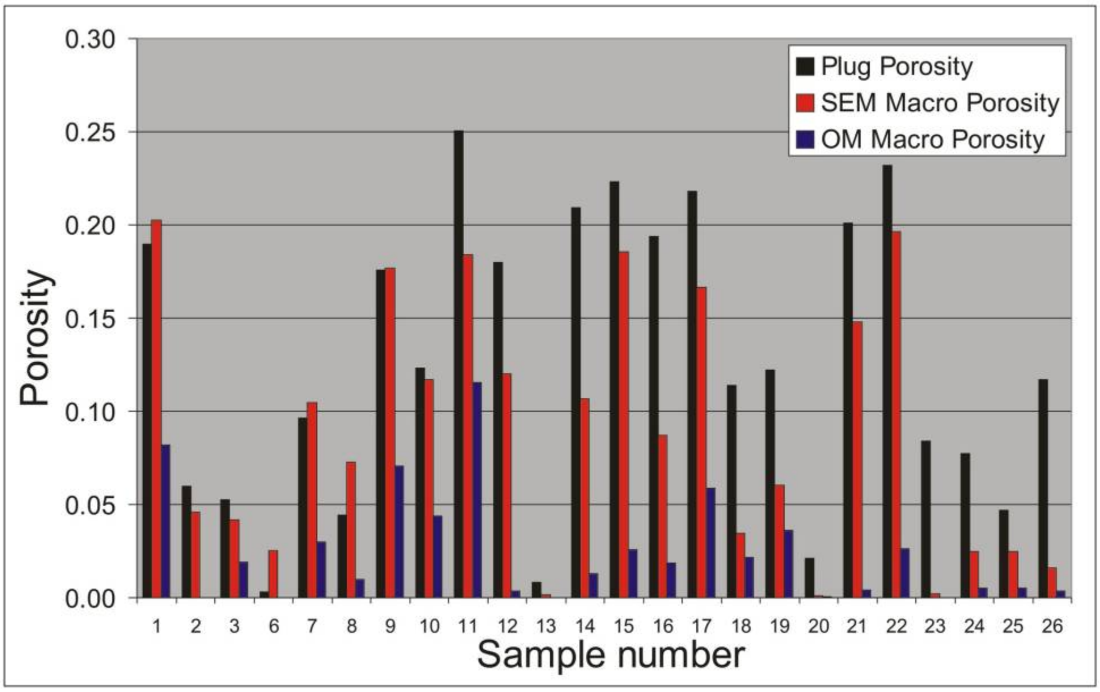

Fig. 1: Total porosity compared to macro-porosity measured on images acquired by optical light microscopy (OLM) and scatter electron microscopy (SEM) at similar pixel resolution.

Effect of micro-porosity on velocity

Color coding the samples with the quantitative amounts of micro-porosity reveals trends in a velocity-porosity plot (Figure 2). We observe two end-member classes: samples that have a high amount of micro-porosity (>80) and those with a low amount of micro-porosity (<50%) (Figure 2).

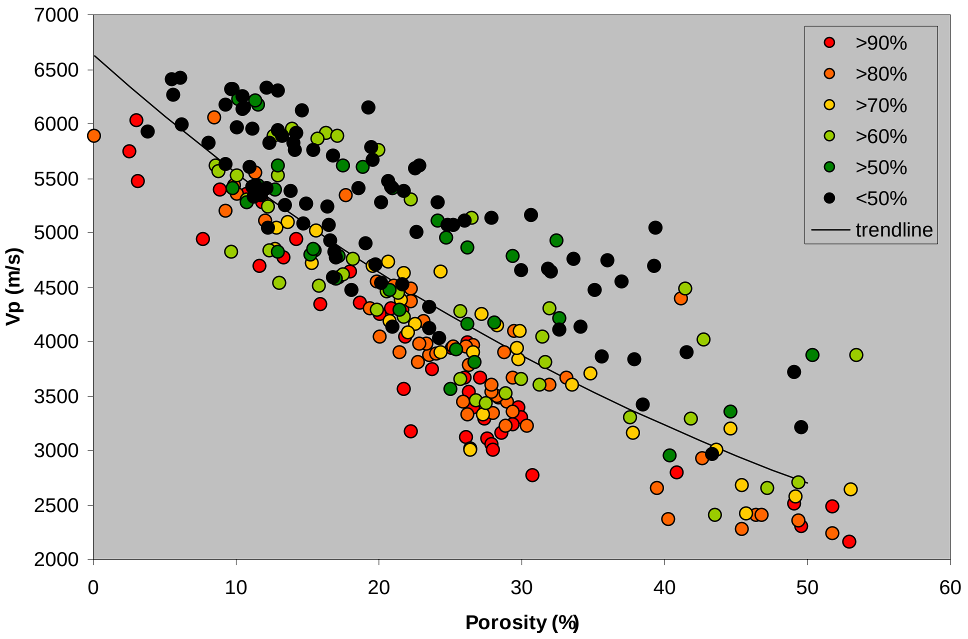

Vp = 4550 m/s
Porosity = 38%
A

Vp = 2700 m/s
Porosity = 49%
B

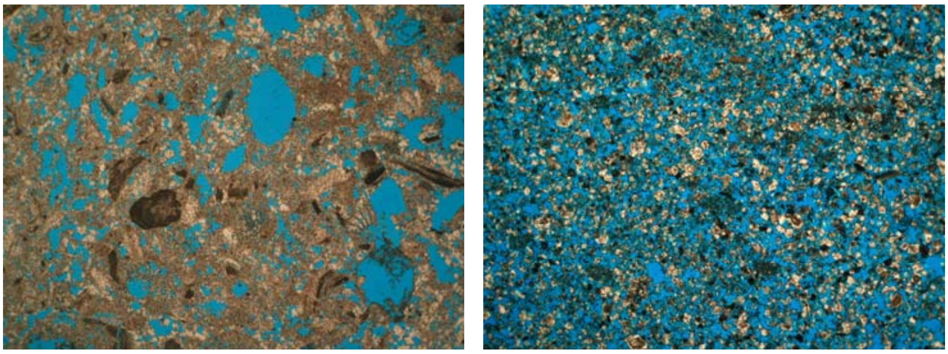

Figure 2: Plot of porosity versus P-wave velocity with color indicating the percentage of the total porosity due to micro-pores. The exponential trendline results in a correlation coefficient of r^2= 0.67. A and B. Color images of two dolomites whose velocities are a function of the porosity and the pore structure. Dolostones dominated by large vuggy pore types show faster P-wave velocity than sucrosic dolostones dominated by intercrystalline micro-porosity.

Samples that have >80% percent micro-porosity display the lowest velocities at a given porosity. This trend indicates that the small pores are “soft” compliant pores and therefore cause slow velocities. Furthermore, micro-porosity often produces low velocities independent of the mineral grain moduli stiffness. For example, samples with a high amount of micro-porosity (>80%) in fine-grained dolomite euhedral rhombs and slow velocities (~2500m/s) are sucrosic dolostones (Figure 2). Likewise, a globerina packstone that has high micro-porosity within a micritic calcitic matrix with few intraparticle macro-pores exhibits a slow velocity (~3000m/s).

Carbonates with high amounts of micro-porosity are scattered closely around the Wyllie's time-average velocity, whereas increasing amount of macro-porosity appears to cause larger velocity scatter at a given porosity. Samples with intercrystalline, vuggy and macro-moldic porosity show strong positive velocity deviations from Wylie's time average velocity.

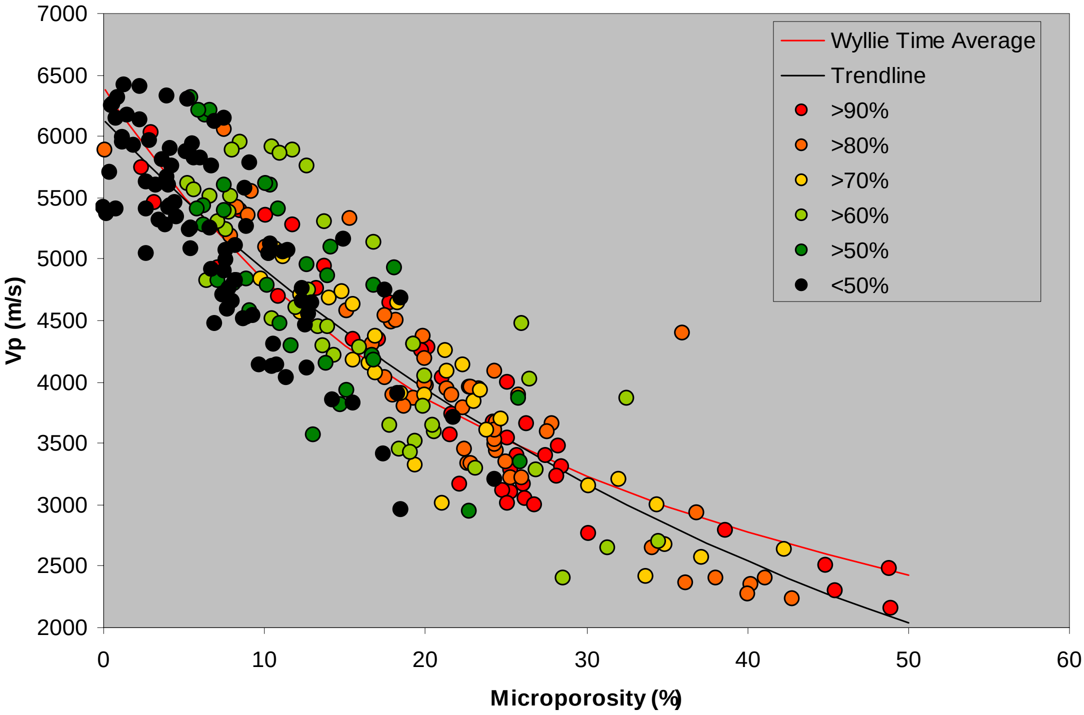

Figure 3: Velocity versus micro-porosity plot, exluding all porosity in macro-pores. The exponential regression trendline results in a correlation coefficient of $r^2 = 0.83$.

Pore types with high amounts of macro-porosity (>50%) form a cluster in a velocity-porosity diagram (Figure 2) and display the highest velocities at a given porosity. For example, samples with the highest amount of macro-porosity (>50%) are, in our dataset, recrystallized dolomites with vuggy and intercystalline porosity (Figure 2). Peloidal grainstones with a strong calcitic frame also display fast velocities and fall into the class of high percentage of macro-porosity (>50%). Macro-pores are formed and preserved by dissolution of the original grain and cementation of the interparticle pore space.

Using micro-porosity calculated from digital images of thin sections, instead of total plug porosity, the velocity uncertainty is significantly reduced (Figure 3). The correlation coefficient increases from 0.67 (porosity-velocity transform) to 0.83 (micro-porosity-velocity transform), derived from an exponential best-fit curve.

Dealing with micro-pores in elastic modeling

The next challenge is to incorporate our observation in the prediction and the modeling of the elastic properties of our carbonate samples. Over the last decade, different studies have documented the highly complex relationship between the elastic behaviour of carbonates and the complexity of their pore systems (porosity and pore shape), framework texture, mineralogy and diagenetic history (Eberli et al, 2003). However, the direct prediction of these elastic properties from the pore and/or grain texture is still highly uncertain, because the parameters in elastic modeling are difficult to quantify; only a few attempts have been made to do so (Rossebø et al., 2005; Agersborg, 2007). We present a direct forward velocity modeling procedure for predicting elastic properties in carbonates; we start from a detailed pore-geometry analysis from thin sections and mineralogy from X-ray diffraction analysis, taking into account the respective amounts of macro-pores and micro-pores. We then compare our model results to the ultrasonic measurements in the laboratory.

The differential effective medium model (DEM) is a reliable rock-physics model that accounts for both the varying mineralogy and the complex pore networks; the latter are quantified using pore-geometry spectra obtained from both OLM and SEM images of thin sections. In addition, DEM allows us to directly calculate both wet and dry properties of carbonate rocks without using Gassmann fluid substitution. Because, in our experimental work, micro-porosity impacts elastic properties, we consider the carbonate rock to be a dual-porosity system and assign a different stiffness (defined as aspect ratio in the DEM model) to the micro-pore fraction than to the macro-pores. The macro-pore fraction is obtained from the digital image analysis, and its stiffness can be set to a fixed stiff value or to a spectrum of stiffnesses based on measured macro-pore roundness (Figure 4).

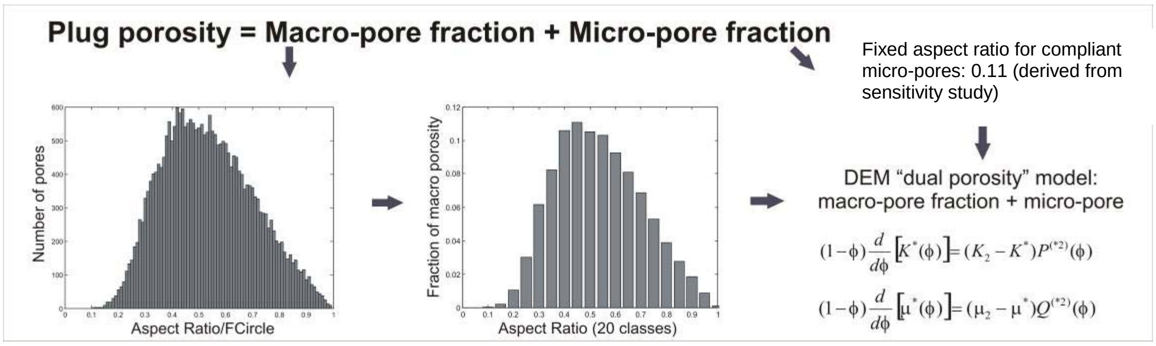

Figure 4: A workflow to estimate elastic properties directly from pore structure information observed from thin sections uses a dual porosity approach as input for the differential effective medium (DEM). The aspect ratios of all individual macro-pores from a thin section image are derived and are assigned to classes that represent the fraction of the macro pore space with a certain measured aspect ratio. These classes are directly implemented in the DEM model. Alternatively a fixed aspect ratio can be assigned to the entire macro-pore space. In addition, we introduce the micro-pore fraction with a fixed (soft) aspect ratio separately in the DEM model. As such we create a dual input in the DEM to model velocities in carbonates directly from thin sections.

Figure 4 shows how the aspect ratio is measured over the entire macro-pore space, and how a different stiffness according to the fraction of aspect ratio is assigned. For the entire sample dataset the aspect ratio spectrum of the macro-pores shows only subtle changes for different pore types, centered around a mean aspect ratio of ~ 0.5. This narrow range of mean pore aspect ratios is in agreement with other carbonate image analysis study results (Colpaert, 2007). When the spectra are not available, one fixed aspect ratio for macro-pores can be used. This aspect ratio is put into the DEM together with a fixed soft stiffness (low aspect ratio) for the micro-pores. Micro-pores are assumed to be soft, based on our experimental work and is not based on direct microscopic examination of the aspect ratio. Effective elastic properties are then obtained from a dual porosity DEM (micro- and macro-pores), directly based on pore-shape information and mineralogy. Our approach uses the DEM model as an analogue to the average effect of the different pore shapes and different size fractions, as observed in many individual carbonate samples, on the elastic properties of the rock.

The soft part of the carbonate rock is often described in the literature as "micro-cracks" (e.g., Agersborg, 2007); however the micro-porosity is often partly hidden in this term. Differentiating between physically observable cracks and connected micro-pores is especially important in terms of stiffness and dynamic fluid flow properties of these carbonate rocks. Ideally, we would consider carbonate rocks to be "multiple pore space” rocks (cracks, micro-pore, meso-macro-pores, open fractures, etc.), although geologically controllable parameterization might become very difficult.

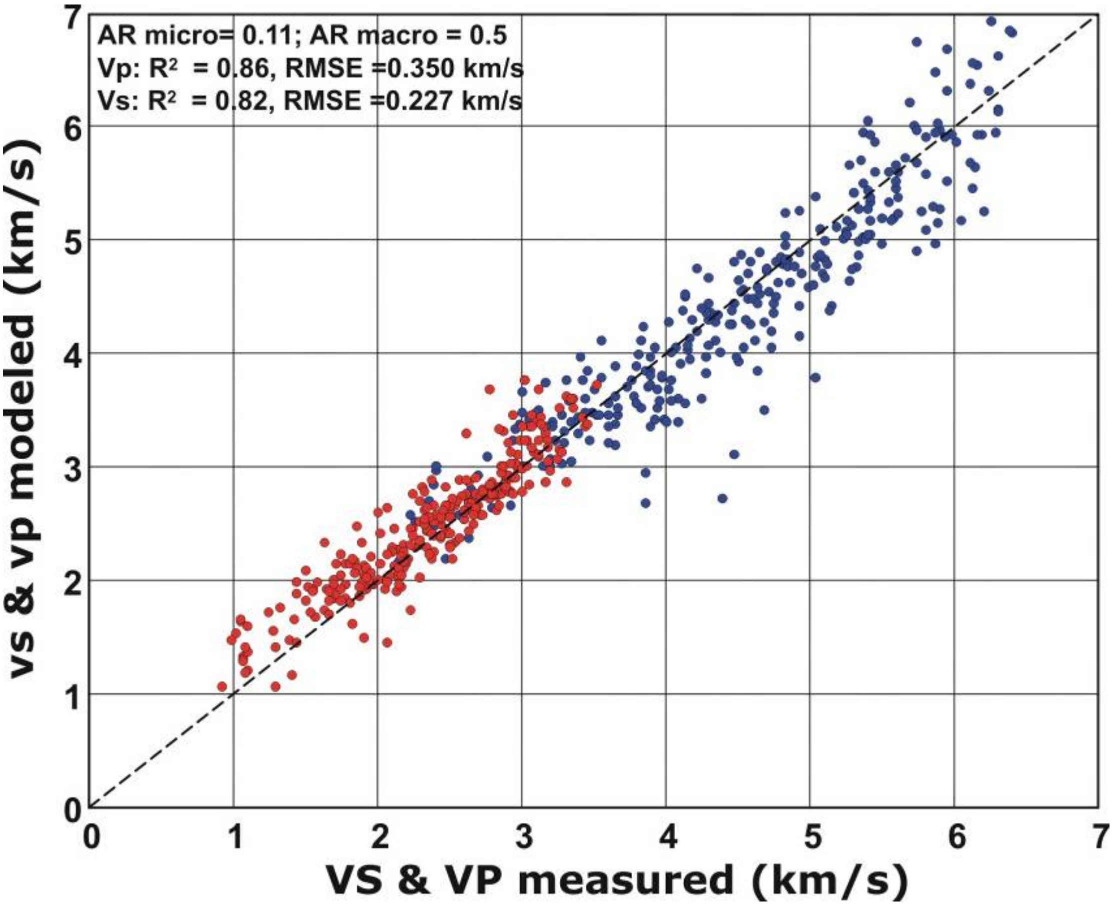

Figure 5: Measured S-wave (red dots) velocity (Vs) and P-wave (blue dots) velocity (Vp) versus calculated velocities from pore structure observations.

Our dataset of around 250 samples was used to test our method both for dry and brine-saturated conditions. When fine-tuning the model parameters, we achieved generally a good match between modelled velocities from thin sections and measured ultrasonic velocities. Good correlation coefficients and Root Mean Square Error (RMSE) values for both P-wave and S-wave velocities demonstrate the reliability of the modeling (Figure 5). Our modeling results clearly demonstrate that the softening effect of the micro-pores can not be ignored in modeling and that carbonates should be approached as a dual-porosity system. As such, we give clear evidence that not only pore shape but equally important the pore size, and in particular the amount of micro-pores, induce important variations in elastic properties. The low to medium velocity samples display the best fit between measured and modelled velocities

(Figure 5). Larger uncertainties are observed with the lowest porosity (highest velocity) samples, due to the dominance of solid properties over pore-space properties and due to the effects of fluid distribution in small isolated pores or cracks. But overall, our relatively simple forward model based solely on thin section and plug porosity information gives a good estimate of velocity variations.

Micro-porosity: Link between velocity and permeability

The velocities of carbonate rocks often display a low correlation with porosity and permeability. Most carbonate pore-type classifications that account for the scatter in a diagram of porosity versus permeability are the result of qualitative descriptions of pore size, pore type and patchiness (Archie, 1952; Lucia, 1995; Lønøy, 2006). Our approach, which quantifies pore types based on the stiffness of the rock at a given porosity, produces an “acoustically derived pore type”. We propose that the “acoustically derived pore type” be calibrated as a first approximation to the amount of micro-porosity in the sample. Once the model has been calibrated, the ”acoustically derived pore type” can be used as a link between rock properties; e.g., velocity and permeability.

Macro-pores contribute much to porosity, but they have little effect on sonic velocity, as demonstrated in Figure 6a and 6b. Subtracting the visible macro-porosity on thin sections from the total measured plug porosity and plotting the remaining micro-porosity against velocity demonstrates this fact (Figure 6b).

Whereas micro-pores are strongly related to the rock’s velocity, micro-pores are relative ineffective for fluid flow (Figure 6c). A plot of porosity versus permeability shows a low correlation (r^2 = 0.25) between porosity and permeability in carbonate rocks (Figure 6c). The permeability shows a large scatter of up to 4 orders of magnitude at porosity of 10% and also at high porosities. Incorporating micro-porosity in our analysis, we recognize that samples with pore structure associated with high micro-porosity (black dots) are restricted to low permeability at a given porosity (Figure 6d). Excluding micro-porosity from the correlation with permeability reduces permeability uncertainty by two and a half orders of magnitude (Figure 6d), when compared to the total porosity versus permeability trend.

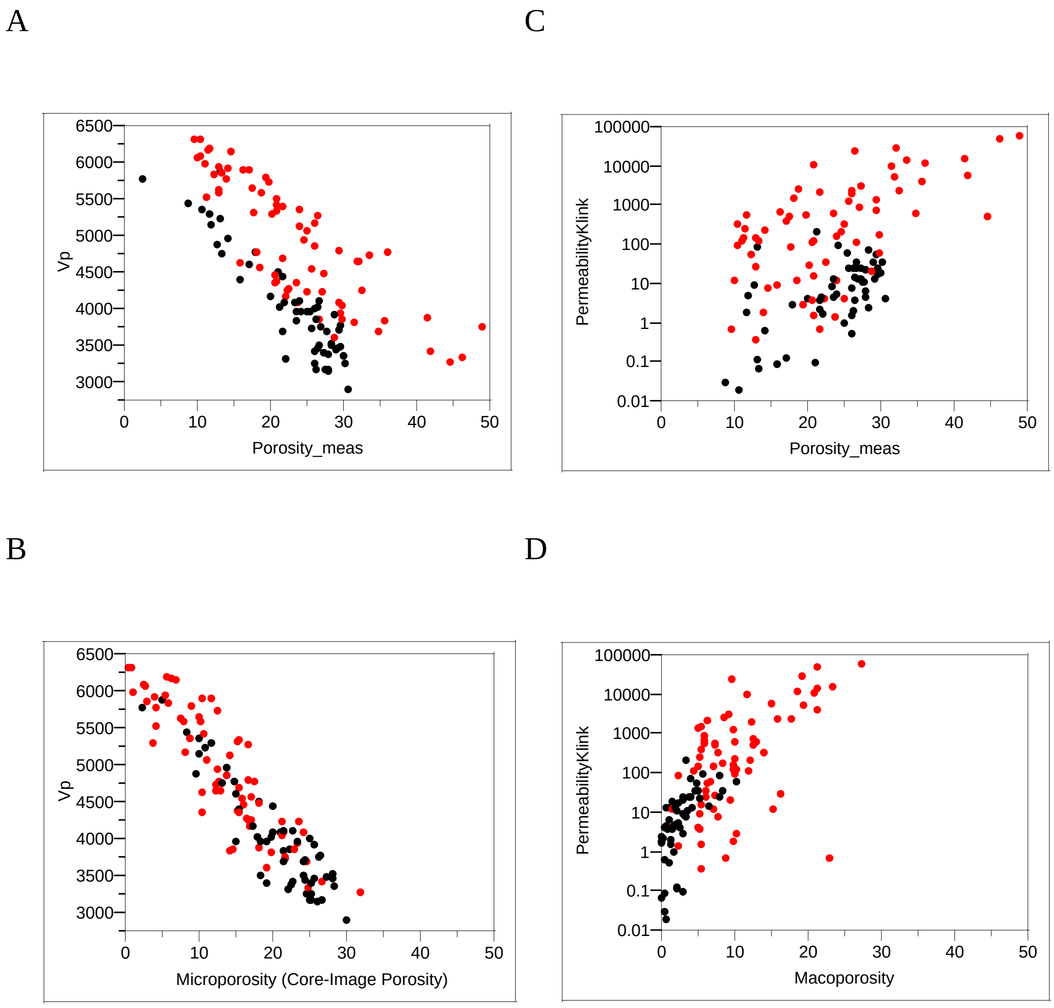

Figure 6: A: Porosity versus P-wave velocity. B: micro-porosity versus velocity. Samples with micro-porosity (black dots) shows smaller scatter in porosity-velocity plot than samples with less micro-porosity (red dots). Using micro-porosity instead of total porosity shifts the samples towards lower porosity and improves the porosity-velocity correlation. C: Porosity versus permeability. Samples with pore structure associated with micro-porosity (black dots) are restricted to permeabilities below 100mD, while samples with low amount of micro-porosity (red dots) have higher permeability. Bottom: Macro-porosity versus permeability reduces the uncertainty in a porosity-permeability transform by 2 orders of magnitude when compared to the total porosity-permeability transform (bottom).

Our approach of relating velocity to porosity and permeability requires the ability to separate total porosity into micro-porosity and macro-porosity. An improved estimate of porosity can be achieved by calculating the rock stiffness that quantifies the deviation of sonic velocity at a given porosity and relates back to the ”apparent” micro-porosity fraction (Figure 7). As seen in the previous paragraph, the scatter in a velocity – porosity diagram can be parameterized to derive the “apparent” micro-porosity, using a dual porosity DEM model. Using "apparent" micro-porosity and porosity derived from an inverse DEM modeling process has the potential of relating velocity to permeability.

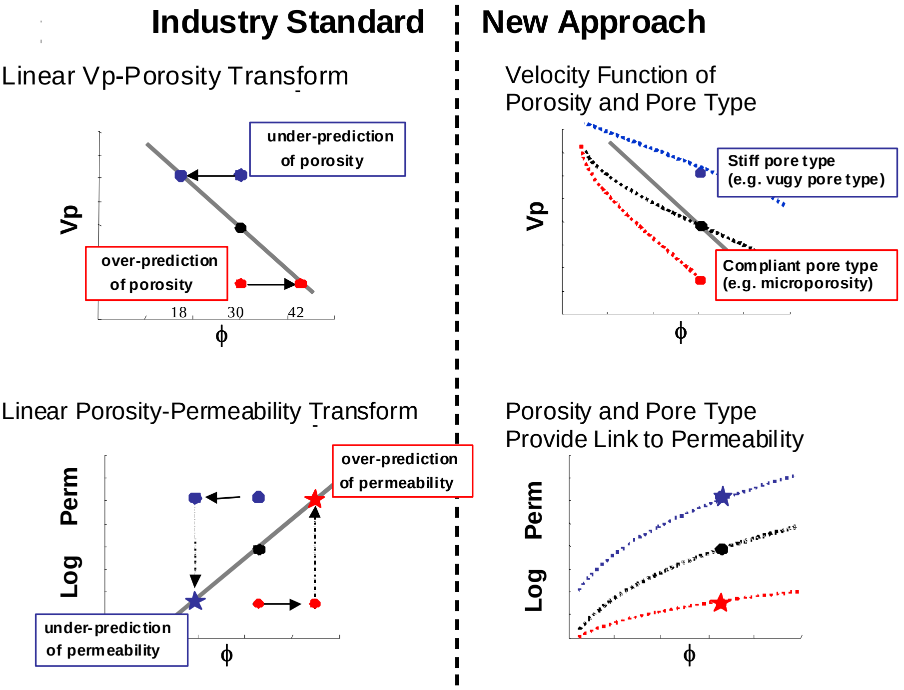

Fig. 7: Simple schematic diagrams showing (left) the traditional workflow of straight-line property transforms and associated potential prediction pitfalls (right) the new approach in which the pore structure information provided by the scatter in the velocity-porosity relationship is parameterized, using a rock-physics model. The pore structure and the porosity provide the link for a cross-property relationship between velocity and permeability.

Conclusion

Our empirical data show that compliant micro-pores have a strong softening effect on a carbonate rock and thus are influential in lowering its sonic velocity. By subtracting the macro-porosity from total porosity the scatter in a velocity – porosity relationship can be reduced, indicating that the fraction of stiff macro-pores versus soft micro-pores is responsible for the variation of velocity at any given porosity. Consequently, a rock-physics model that captures the presence of both macro- and micro-porosity, as well as their respective stiffness, is needed to better estimate velocity and permeability (Figure 7). In our model, the respective percentages are directly derived

=from quantitative pore geometry analysis from thin sections of the modelled plug. We use a differential effective medium (DEM) model with a dual-porosity approach and incorporate macro- and micro-porosity values derived from quantitative image analysis. A good match was obtained between observed and modelled elastic properties. This improved our understanding of how the effective stiffness in carbonates rocks is influenced by a combination of the elastic behaviour of the individual pore fractions characterizing the rock sample, depending on their size and shape (Figure 7).

Micro-porosity in combination with macro-porosity parameters also reduces uncertainties in permeability predictions. Samples with high amounts of micro-porosity follow the Wyllie's time-average velocity, and they tend to display low permeability at a given porosity. Thus inverse modeling which produces estimates of the amount of micro-porosity from the basic acoustic properties of density and velocity has the potential to improve reservoir-quality predictions for carbonate reservoirs with complex pore systems.

Chapter 4

CHANGES IN DYNAMIC SHEAR MODULI OF CARBONATE ROCKS WITH FLUID SUBSTITUTION

Abstract

In order to assess saturation effects on acoustic properties in carbonates, we measured ultrasonic velocity on 38 limestone samples with porosity ranging from 5% to 30% under dry and water-saturated conditions. Complete saturation of the pore space with water causes both, an increase and a decrease in compressional and shear wave velocity, and significant changes in the shear moduli.

Compressional velocities of most water-saturated samples are up to 500 m/s higher than the velocities of the dry samples. Some show no change, and a few even show a decrease in velocity. Shear wave velocity (Vs) generally decreases but nine samples show an increase of Vs by up to 230 m/s. Water saturation decreases the shear modulus by up to 2 GPa in some samples and increases it by up to 3 GPa in others. The average increase in the shear modulus with water saturation is 1.23 GPa, the average decrease is 0.75 GPa. The Vp/Vs ratio shows an overall increase with water saturation. In particular, rocks displaying shear weakening have distinctly higher Vp/Vs ratios. Grainstone samples with high amounts of microporosity and interparticle macro-pores preferentially show shear weakening, whereas recrystallized limestones are prone to increase shear strengths with water saturation.

The observed shear weakening indicates that a rock-fluid interaction occurs with water saturation, which violates one of the assumptions in Gassmann’s theory. We find a positive correlation between changes in shear modulus and the inability of Gassmann’s theory to predict velocities of water-saturated samples at high frequencies. Velocities of water-saturated samples predicted by the Gassmann’s equation often exceed the measured values by as much as 400 m/s for samples exhibiting shear weakening. In samples showing shear strengthening Gassmann-predicted velocity values are as much as 600 m/s lower than the measured values. In 66% of our samples Gassmann-predicted velocities show a misfit to the measured water-saturated p-wave velocities. This discrepancy between measured and Gassmann

predicted velocity is not solely caused by the velocity dispersion but also by rock-fluid interaction that is related to the pore structure of carbonates. Thus, a pore type analysis should be conducted to assess shear moduli changes and the resultant uncertainty for AVO analyses and velocity prediction using Gassmann's theory.

Introduction

Most laboratory research on saturation effects had been carried out on sandstones despite the fact that about half of the world's oil and gas reserves are in carbonates. We conducted saturation experiments in carbonates with the intention to fill this gap. Laboratory experiments show that the sonic velocity of carbonates under constant pressure and full water saturation is mainly controlled by a combination of porosity and pore type (e.g., Wyllie et. al., 1958; Anselmetti and Eberli, 1993; Anselmetti et. al.,1997; Eberli et al, 2003; Wang, 1997). The variation of the velocity at a given porosity can be largely attributed to variations in pore types and pore size (e.g. Weger et. al., 2004; Baechle et. al., 2004).

Few studies evaluated the effect of water-saturation on velocity in carbonate rocks. Wyllie et al. (1963) first noticed that in rocks under water-saturated conditions, shear velocity decrease more than expected just from the increase in density alone. In contrast, Ravavich et al. (1984) concluded that the porosity is the dominant factor and neither the petrographic fabric nor the type of pore-fluid has a statistically relevant influence on the velocity. Several laboratory studies using high-frequency acoustic signals have been conducted specifically to assess the validity of Gassmann's equation for the estimation of p-wave velocities in carbonates (Wang 2000. Marion and Jizba, 1997, Nolen-Hoeksema et al., 1995; Rasolofosaon and Zinszner, 2003). As expected, most studies find that Gassmann-predicted velocities either fit or underestimate the laboratory measurements. The difference between the measured and the Gassmann-predicted velocity is generally explained by high frequency dispersion effects. Wang et al. (2000) reports Gassmann-predicted velocities in low porosity carbonates that are higher than velocities from laboratory measurements.

Japsen et al. (2002) and Assefa et al. (2003) measured effects of water saturation on shear velocity of low porosity chalk (34 samples) and oolitic grainstones and packstones (39 samples), respectively. Their data display consistent lower shear moduli for wet samples. On average, the shear strength is reduced by 0.5 GPa in chalk (Japsen et al., 2002) and 2 GPa in oolitic grainstone and packstone (Assefa et al., 2003). Their data are the first indications that the shear modulus is not constant under different saturations. A constant shear modulus is, however, a consequence of Gassmann's derivation (Berryman, 1999). A constant shear modulus is not explicitly implied in Gassmann's theory, but implicitly derived by the numerous Gassmann assumptions for a porous system. A change in the shear modulus implies that estimating velocities of saturated samples using Gassmann's equation might be inaccurate. Adam et al. (2006) addresses this issue using different frequencies for carbonates with compliant pores or microcracks with laboratory experiments in the seismic frequency domain. They observe shear weakening in three samples using seismic frequencies. In addition, they show that shear moduli under seismic frequencies are consistently lower than shear moduli measured at ultrasonic frequencies.

In this paper, we present results of laboratory experiments designed to further investigate the effect of saturation on carbonates, using samples with a wide range of porosities and pore types. Our results corroborate earlier findings of changes in shear moduli with changing saturation as we observe significant shear strengthening and shear weakening. We propose that these changes are related to the pore structure variations in our samples.

Experimental setup

We selected 38 limestone samples from Cretaceous and Miocene reservoirs with porosities from 5% to over 30%. The rock textures include wackestone, packstone and grainstone according to the Dunham classification (Dunham, 1962). The macro-pore types include interparticle, vuggy and moldic to intraframe porosity.

Measuring the velocity under dry and water-saturated conditions on a single sample with variable confining pressure is challenging, because the sample might be altered during pressurization. To overcome this experimental dilemma we adopted the following procedure. We selected macroscopically homogeneous samples and cut them in half, creating two almost identical twins. Samples with porosity differences of more than 2% between the two halves were not used for this experiment. One half of each sample was measured first under dry conditions, using variable hydrostatic confining pressures in a series of small steps from 2 MPa up to a maximum of 80 MPa and back down to 2 MPa. The data are plotted at 40MPa effective pressure in the figures throughout the paper, which is around the reservoir pressure of the field. The pore pressure was kept constant at 1 atmosphere. The samples were dried at 60° Celsius for three days in an oven, then placed in a jar that also had water absorbing crystals to protect them from the Miami humidity. Thus, the dry samples are considered room-dry with some insignificant moisture content. To completely saturate the samples, they were saturated with degassed, distilled water for at least 12 hrs under vacuum conditions (~ 2.5 MPa). In the following paragraphs, saturation will always refer to changes from dry conditions to fully water-saturated conditions.

A sample was judged to be unaltered after dry measurements if, upon completion of the pressure cycle, no hysteresis effect was detected and no decrease in the velocity during the increasing pressure cycle was observed. Consequently the samples were water-saturated and measured under fully water-saturated conditions. Otherwise, the 2nd half of the sample was used for the measurements under water-saturated conditions. During the measurement the pore fluid pressure was kept constant at 2 MPa. Velocities were measured under the same effective pressure steps as in the dry sequence. Ultrasonic velocities were measured at a center frequency of ~1 MHz, using a pulse transmission technique (Birch, 1960). A single compressional wave and two independently orthogonally polarized shear waves were simultaneously measured using Geoverde© transducer arrangements.

The precision of our experimental velocity measurement is within 3%. This precision is represented in the size of the data dots (60 m/s) in the figures that show velocity versus porosity relationships. Due to the square root relationship between velocity and moduli, the precision to determine s-wave velocity increases from 3% in velocity, to a precision of 6% when calculating the shear moduli of the samples using the following equation:

$$\mu = V_S^{\,2}((1-\phi)\rho_{Grain} + \phi\rho_{Fluid}) \tag{1}$$

For example, samples with a porosity between 25% to 30% and an average s-wave velocity that follows the correlations line in Figure 1b have an absolute shear modulus between ±0.2 GPa and ±0.3 GPa.

Effect of porosity and pore structure on velocity

In our sample set, the ultrasonic compressional wave velocity (Vp) ranges from 3000 to 6000 m/s (Fig. 1a) and the ultrasonic shear wave velocity (Vs) from 1800 to 3300 m/s (Fig. 1b). In general, velocities show an inverse correlation with porosity, but the scatter in velocity of samples with the same porosity can be as high as 1500 m/s for Vp and 650 m/s for Vs (Fig. 1). Data points in the ultrasonic p-wave velocity-porosity plot appear to have a similar degree of deviation from the best fit least r-square linear regression trend line as in the ultrasonic shear velocity-porosity plot (Figs. 1a and 1b). Most samples, which display a positive deviation in the Vp-porosity space, show also a positive deviation in the Vs-porosity space, and vice versa for a negative deviation (Fig. 2). The velocity scatter is quantified as the deviation from a linear best fit line in m/s. At a given Vp, the Vs deviation can be as high as 200 m/s and at a given Vs we observe up to 500 m/s in Vp deviation. When plotting the deviation of Vs against the deviation of Vp (Fig. 2), the dry samples reveal a slightly better correlation of the scatter (r^2=0.88) than the saturated samples (r^2=0.80). In Figure 2, the average s-wave/p-wave velocity deviation shows a higher ratio of saturated samples (0.53) in comparison to the lower dry velocity deviation ratio (0.43).

The scatter in velocity at a given porosity and pressure cannot be explained by mineralogy because the limestone samples are mono-mineralic (calcite). The large scatter is mainly caused by variations in pore type, corroborating results by Anselmetti and Eberli (1993). In our study, samples with a velocity significantly higher than the trendline are limited to rocks with dominant intraparticle, moldic and vuggy pore types. For example, rocks dominanted by intraparticle porosity have velocities which are at the most 1500 m/s faster than a rock dominated by interparticle porosity. This increased velocity at

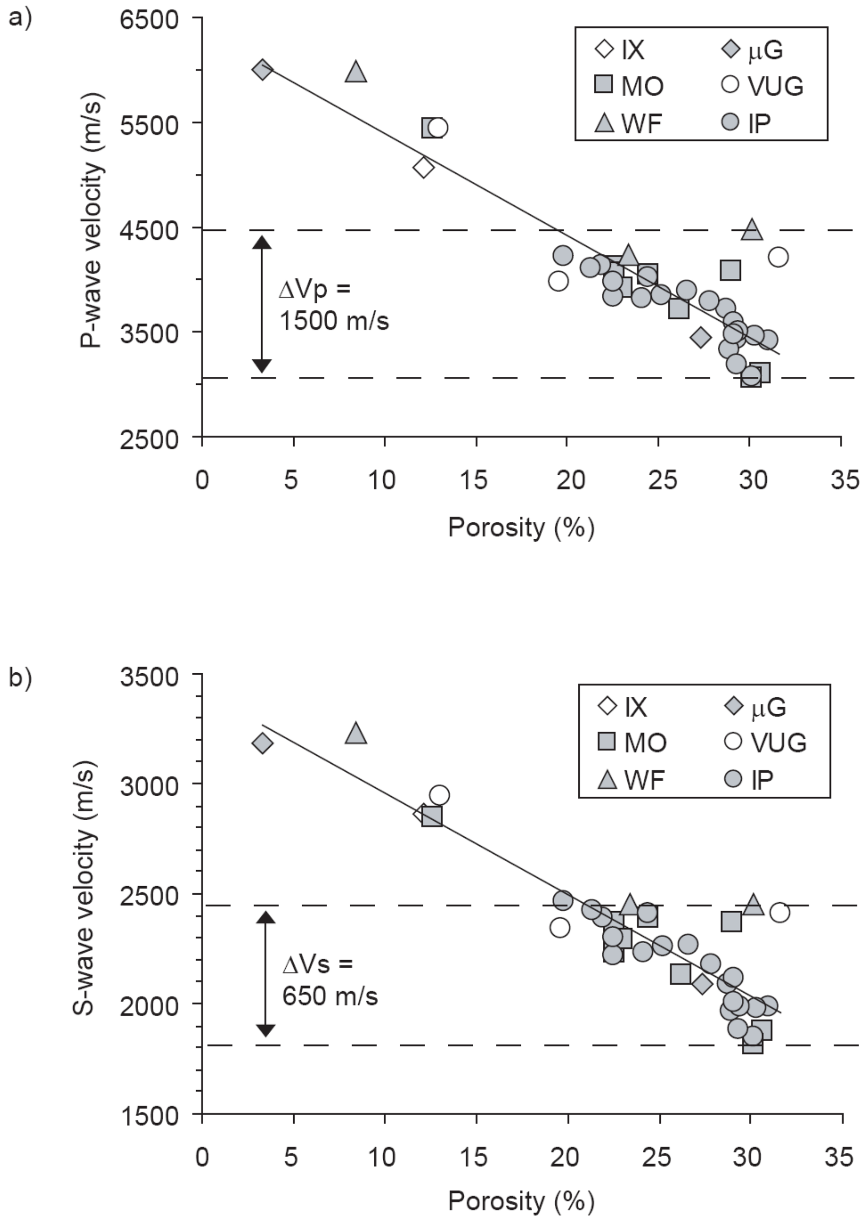

Figure 1: Plot of dry p-wave velocities (a) and s-wave velocities (b) versus porosity at 40 MPa effective pressure. Samples with intraparticle, moldic and vuggy porosity show a positive deviation from the linear best fit regression trendline (µG = intragrain microporosity, IX = intercrystalline, IP = interparticle, WF = intrafossil, VUG = vuggy, MO = moldic).

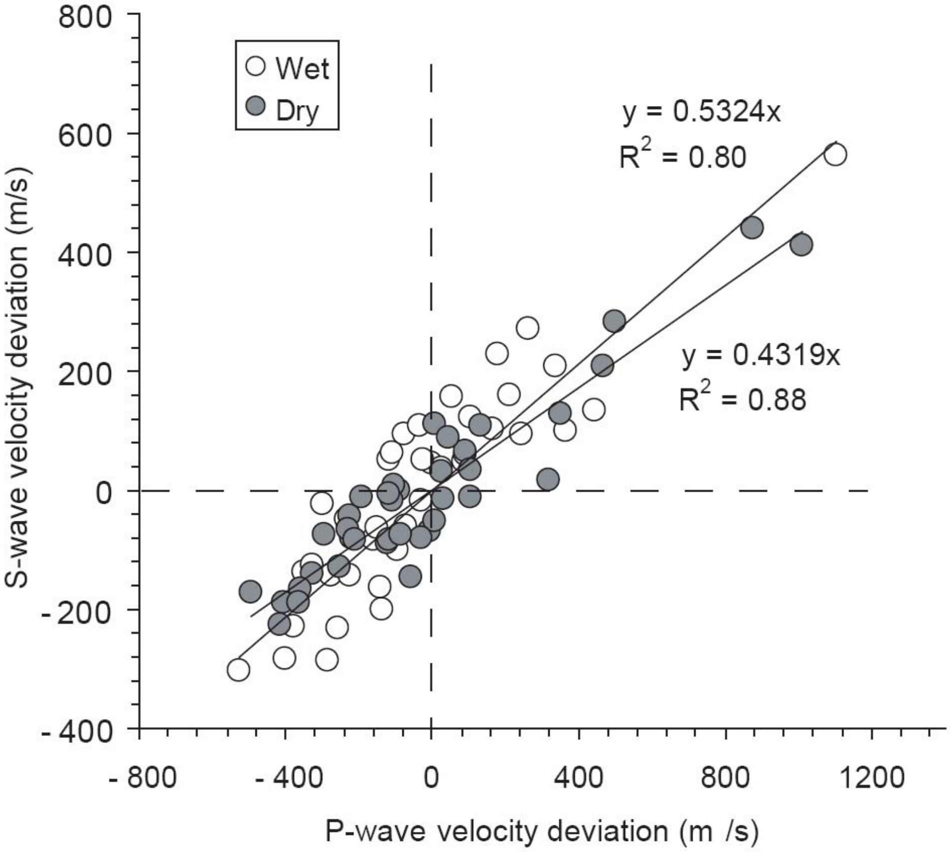

Figure 2: Plot of p-wave velocity versus s-wave velocity deviation from a best fit linear regression trendline. The dry velocity deviation of V_P and V_S has a slightly better linear best-fit line ($R^2 = 0.88$) than the deviation observed under water-saturated conditions ($R^2 = 0.80$).

the same porosity is explained by the strong frame in rocks with moldic and intraframe porosity and by the high percentage of ineffective macroporosity in rocks with vuggy pores (Baechle et al. 2004). In contrast, rocks with interparticle and intercrystralline porosity have relatively low velocities. The very good correlation of p- and s-wave velocity deviation in Figure 2 indicates that most of the scatter in both velocity-porosity plots is not caused by random error, but indeed caused by pore structure differences. Pore structures in carbonates create variable velocity at a given porosity for the following reasons: (1) stiff grain contacts affect compressibility and rigidity to a similar degree either caused by cementing grains or by a stiff biogenetic origin of the frame (coral), (2) dissolution creating a texture with single vugs being comparable in length to the ultrasonic wavelength, with the waves traveling through the matrix porosity and most of the vugs but bypassing some of the largest macropores (3) a combination of both previous causes.

Effect of water saturation on velocity

Gas-water substitution causes a decrease in pore space compressibility, which in turn increases the rock’s bulk modulus. This effect should lead to an increase in Vp without significantly affecting Vs. If just the density is increased but pore space compressibility is not affected by water filling the pores, both Vp and Vs would be reduced. In such a case, the Vp/Vs ratio would not change. Table 1 summarizes the expected effects of gas to water substitution on elastic properties in porous media.

In our dataset, most of the compressional wave velocities of the water-saturated samples are up to 500 m/s higher than the velocities of the dry samples, some show no change, and a few display a reduced velocity (Fig. 3a). The shear wave velocity decreases in most of the samples but 9 samples show an increase of Vs by up to 230 m/s, or if expressed as a relative increase of up to 10% (Fig. 3b). The magnitude of decrease (up to 15 %) in Vs with saturation is often more than can be explained solely by the density effect (Fig. 3c). For example, in a rock with 30% porosity a maximum decrease of 8% Vs can be achieved by the increased density with saturation.

The effect of pressure on the velocity of the wet and dry samples varies within our dataset. Two representative samples have been selected to show the saturation effect with increase in pressure. A recrystallized grainstone with intercrystalline and vuggy-moldic porosity shows strong effects of water saturation on Vp with a distinct higher velocity under water-saturated conditions compared to the velocity under dry conditions, especially in the low-pressure regime (Fig. 4a). In the high-pressure regime, the velocity-pressure curve of the water-saturated samples converge with the velocity-pressure curve of the dry samples (Fig. 4a). The differential pressure of 40MPa is comparable with the rock’s reservoir pressure conditions. In contrast, a peloidal, echinoid-dominated grainstone-packstone with interparticle porosity and a high amount of microporosity shows no difference in Vp between dry and wet measurements over the entire pressure range from 2 to 40 MPa (Fig. 4b).

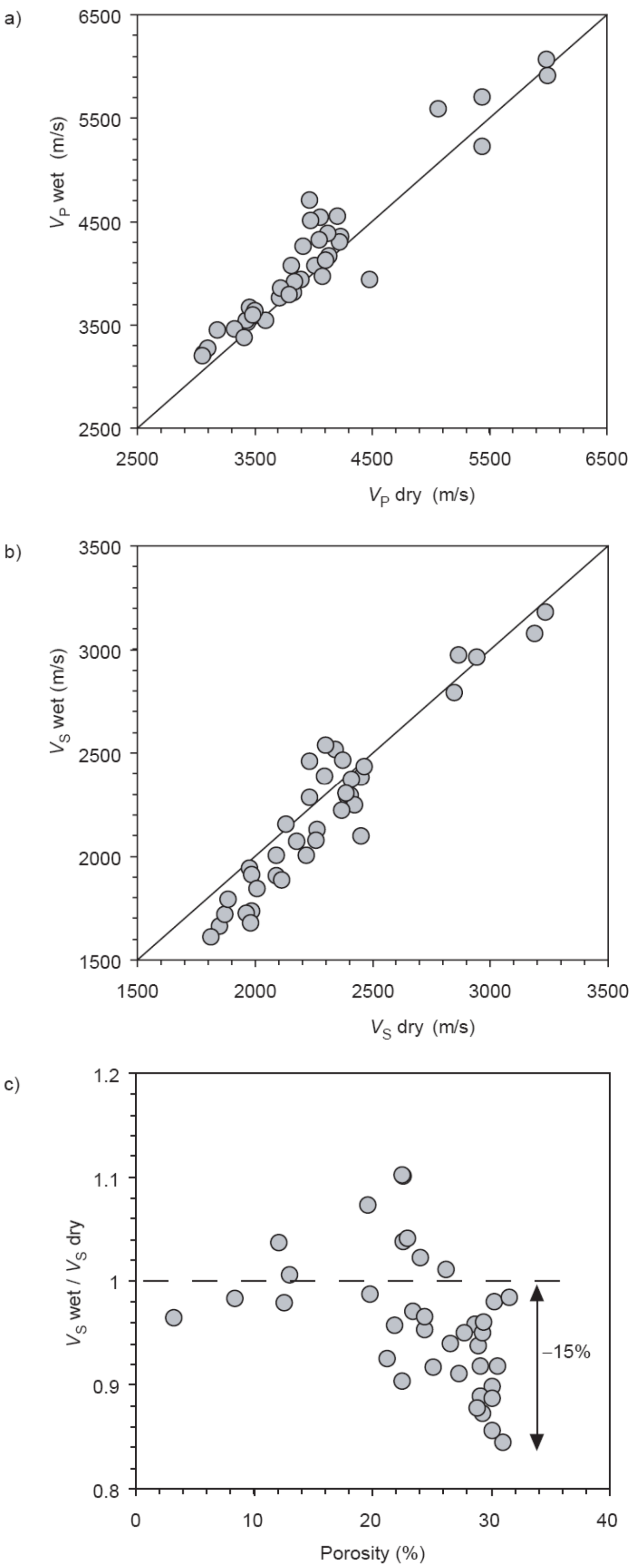

Figure 3: Crossplots of V_P and V_S under fully water-saturated and dry conditions at 40 MPa effective pressure. (a) In many samples the water saturation either decreases or increases p-wave velocity of up to 500 (m/s). In some samples, the “apparent” effect on the p-wave velocity is absent. (b) Most samples show a decrease in the s-wave velocity from dry to completely water-saturated conditions. Few samples show an increase in the s-wave velocity but, in most cases, the s-wave velocity is decreasing by up to 15% if the sample is saturated with water (c).

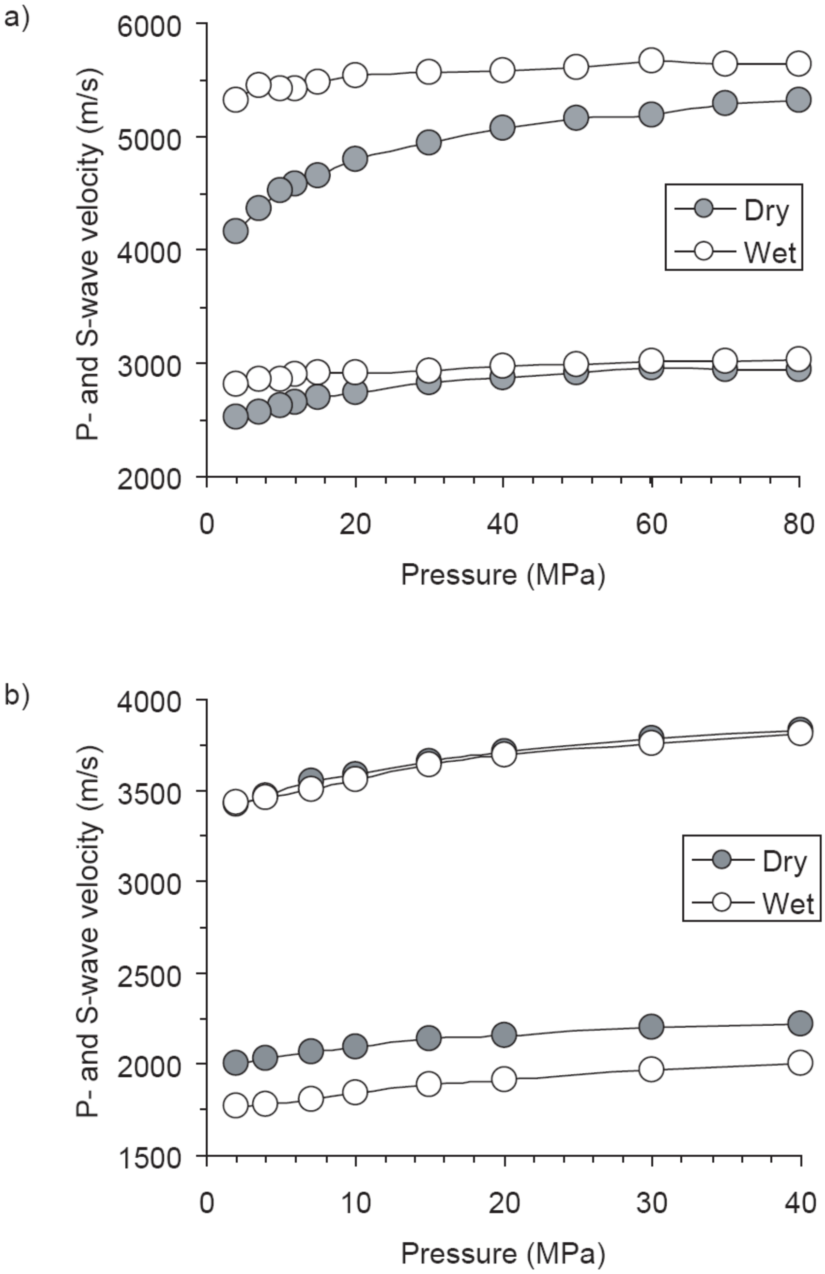

Figure 4: Examples of the different effects of water saturation on the compressional wave velocity. a) A large increase of V_P after water saturation is observed in this recrystallized limestone with dominantly intercrystalline and moldic porosity (12.1% porosity). Such an increase is expected from the Gassmann theory. b) An insignificant increase of V_P after water saturation is observed in this peloidal, skeletal grainstone-packstone with dominantly interparticle porosity (22.5% porosity).

The decrease or increase of Vp due to water saturation can theoretically be explained by Gassmann's equation incorporating two effects at low frequencies: the pore stiffness will increase when the saturating fluid is less compressible than gas and the bulk density will increase with water saturation. Depending on which of the two effects dominates after water saturation, the p-wave velocity will increase, decrease or will not change at all. In addition to these two effects, in laboratory measurements frequency-controlled velocity dispersion is potentially introduced by several mechanisms such as scattering, friction, Biot macroscopic flow, and local flow phenomenon (Winkler and Murphy, 1995). At high frequencies, the velocities of samples measured under dry and saturated conditions

diverge at lower pressures. This divergence could be caused by the opening of thin pores at low pressures. Velocity dispersion effects stiffen the rock at lower pressures more than the expected stiffness increase from water saturation alone. At higher pressures, the additional velocity dispersion effect is reduced due to closure of low aspect ratio pores at grain-to-grain contacts (Mavko and Jizba, 1991). This effect is observed in the re-crystallized sample (Fig. 4a).

Effect of saturation on Vp/Vs ratio

After saturation of the rock, the Vp and Vs either decrease or increase compared to the velocity of the dry rock. A plot of Vp versus Vs shows a general trend of decreased shear wave velocities and increased p-wave velocities with saturation (Fig. 5). This separation helps to discriminate dry and saturated rocks. At lower velocities (Vp < 4000m/s) the dry and wet samples show a better separation than at higher velocities. The dry and wet shear and p-wave relationship follow least square polynomial best-fit curves with a correlation coefficient of 0.98 (Fig. 5):

$$Vs_{wet} = -0.00009Vp_{wet}^2 + 1.3277Vp_{wet} - 1759.6 \qquad (2)$$

$$Vs_{dry} = -0.00002Vp_{dry}^2 + 0.6646Vp_{dry} \qquad (3)$$

If the dry Vp-Vs regression line is not forced to an intercept at zero, Vp and Vs show also a good correlation coefficient of 0.98 with a linear best-fit.

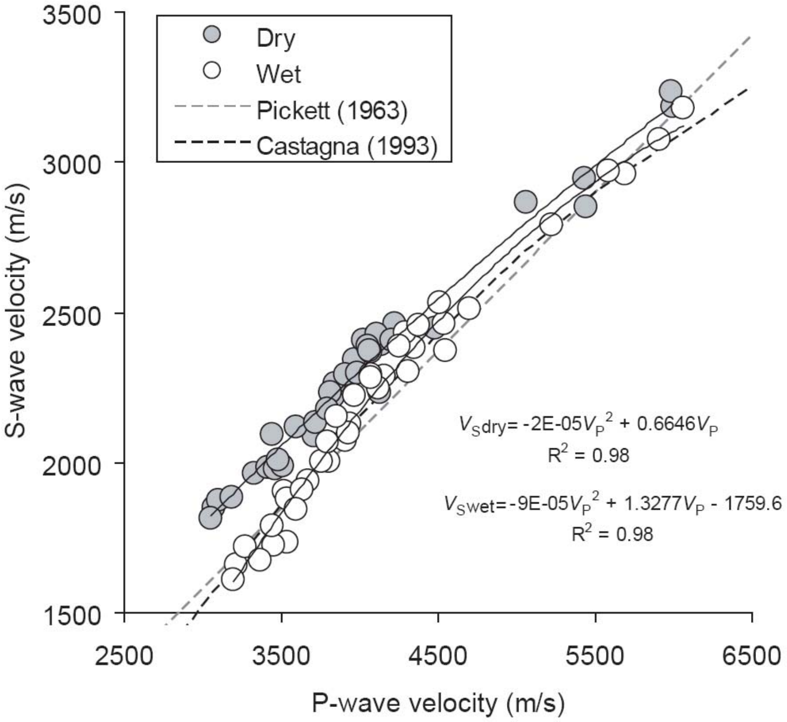

Figure 5: V_P versus V_S for dry and saturated samples at 40 MPa effective pressure. The p-wave velocity increases but the s-wave velocity decreases after water saturation. The compressional and shear velocity under saturated and dry condition show a good correlation with minimal scatter. The s-wave velocities are highly related by a least squares polynomial best-fit to the p-wave velocities. The dashed lines are empirical relations for limestones (Castagna et al., 1993; Pickett, 1963) and fit our saturated dataset very well.

The Vp/Vs ratio exhibits a range of values from 1.65 to 1.9 under dry conditions and 1.75 to 2.05 under wet conditions (Fig. 6). The dry Vp/Vs ratio shows an inverse correlation with porosity while the wet samples display an increasing scatter in Vp/Vs with increasing porosities (Fig. 6). In particular, samples with interparticle porosity show a strong increase in the Vp/Vs ratio under water-saturated conditions. The bulk of the dry Vp/Vs ratios show a small deviation (+/- 0.05) from the average value of 1.72. In contrast, the saturated Vp/Vs ratios show larger deviations from the average value of 1.86.

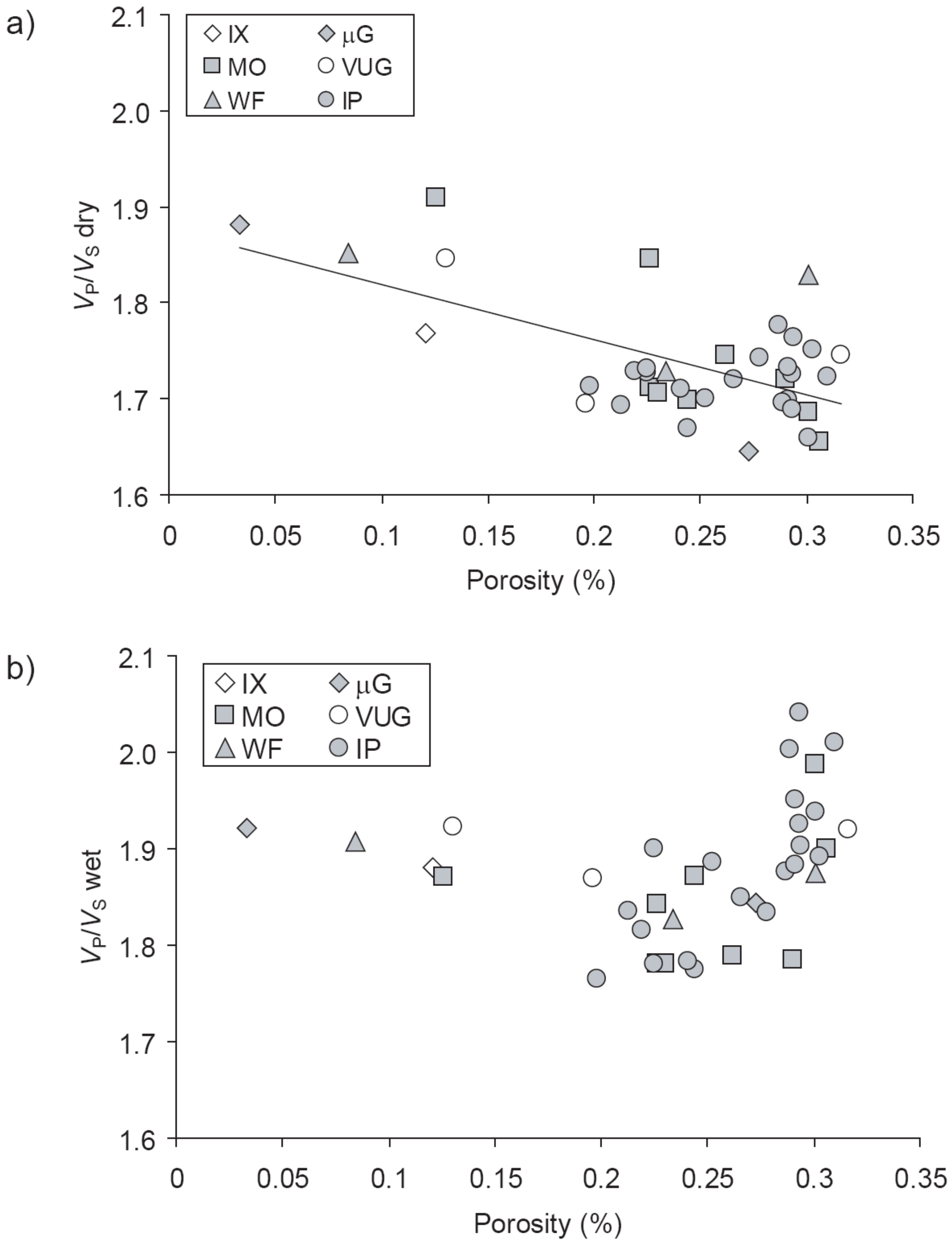

Figure 6: Plot of V_P/V_S at 40 MPa effective pressure versus porosity under dry and water-saturated conditions. (a) The bulk of the dry V_P/V_S ratios show a small deviation (+/- 0.05) from the average value of 1.72. The line represents the inverse correlation of V_P/V_S ratio and porosity. (b) In contrast, saturated V_P/V_S ratios show no clear correlation with porosity but samples with interparticle pore types display a strong increase in the V_P/V_S ratio compared to their dry counterparts (μG = intragrain microporosity, IX = intercrystalline, IP = interparticle, WF = intrafossil, VUG = vuggy, MO = moldic).

The higher Vp/Vs ratios under water-saturated conditions occur mainly in grainstone samples (Fig. 7). The median Vp/Vs ratio of water-saturated pure grainstone samples is significantly higher than the median Vp/Vs ratio in saturated grain-packstone, packstone or wackestone-packstone (Fig. 7). In contrast, the median Vp/Vs ratios of dry grainstones and packstones are similar (Fig. 7).

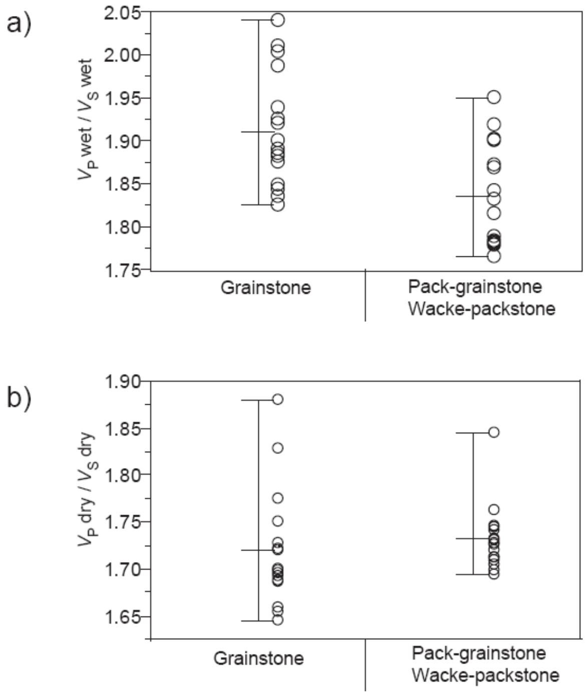

Figure 7: Comparison of the V_P/V_S ratios under dry and water-saturated in grainstones and wackestones - packstones. (a) The median V_P/V_S ratio of pure grainstone samples is significantly higher than the median V_P/V_S ratio in packstones or wackestones under water-saturated conditions. (b) The median V_P/V_S ratio is similar in grainstones vs packstones and wackestones under dry conditions.

Hence, the Vp/Vs ratio of water-saturated samples has the potential of being an indicator for the influence of distinct rock and pore types. Our finding of high Vp/Vs ratio’s in grainstones corroborates Tsuneyama et al. (2003), who also observed higher Vp/Vs ratios in grainstone facies with interparticle porosity.

The wet versus dry relationship of Vp and Vs gives evidence that in carbonates a discrimination of fluid saturation based on p- and s-wave velocities is still possible, although only a small overlap exists (Fig. 5). Castangna’s et al. (1993) non-linear empirical relationship between saturated Vp and Vs as well as Pickett’s (1963) linear empirical saturated Vp-Vs relationship for limestones fit our dataset under saturated conditions over the entire velocity range. We conclude therefore that our dataset is a representative dataset for common carbonate rocks.

Effect of saturation on dynamic moduli

All but two samples display an increase in bulk modulus with water saturation of up to 14 GPa (Fig. 8a). A change also occurs in the shear modulus from dry (μ_d) to water-saturated conditions (μ_w) (Fig. 8b). Compared to the dry shear modulus, the shear modulus decreases with water saturation in some samples up to 3.8 GPa and increases in other samples up to 1.7 GPa. The root mean square error (RMSE) between the measured dry and wet shear modulus is 1.42GPa. Seven samples, representing 8% of our samples, do not show significant changes in the shear modulus with water saturation since the observed shear modulus changes are within the 6% precision. In this paper, a reduction in dynamic shear rigidity after water saturation is defined as shear weakening, whereas increase in the dynamic shear rigidity after water saturation is defined as shear strengthening.

As mentioned earlier, the majority of the samples show a decrease in Vs under fully water-saturated conditions. Only 9 samples show a Vs increase (Fig. 9). The fractional change of Vs caused by water saturation correlates with fractional changes in the shear moduli (r^2=0.93) (Fig. 9). The mean (arithmetic average) shear modulus increase of the entire dataset is +3.45%, going from dry and fully water-saturated measurement conditions, with a standard deviation of 12.49%. The μ_w/μ_d ratio varies from -0.8 to 1.35, documenting how significantly the shear modulus changes with water saturation. This variation indicates that both, shear strengthening and shear weakening, occur in carbonates as a result of saturation.

For the following statistical analysis the dataset is separated into two groups; one group with samples that show “net” shear strengthening and the other in which the samples show “net” shear weakening with water saturation (Fig. 9). The shear modulus of the samples, which show shear strengthening, increases on average by 1.23GPa (STDDEV: 1.17GPa) or 10.82% (STDDEV: 10.22%). The decrease in the shear modulus with water saturation is on average -0.75GPa (STDDEV: 0.49GPa) or -7.84% (STDDEV: 4.68%).

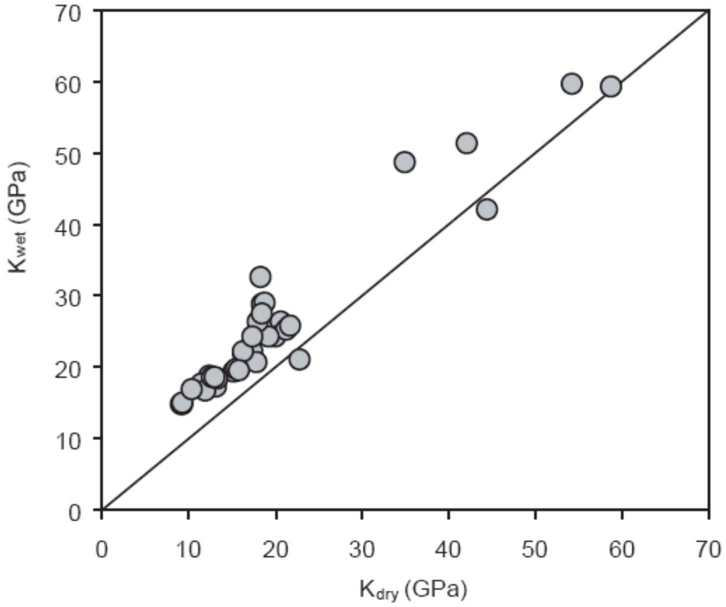

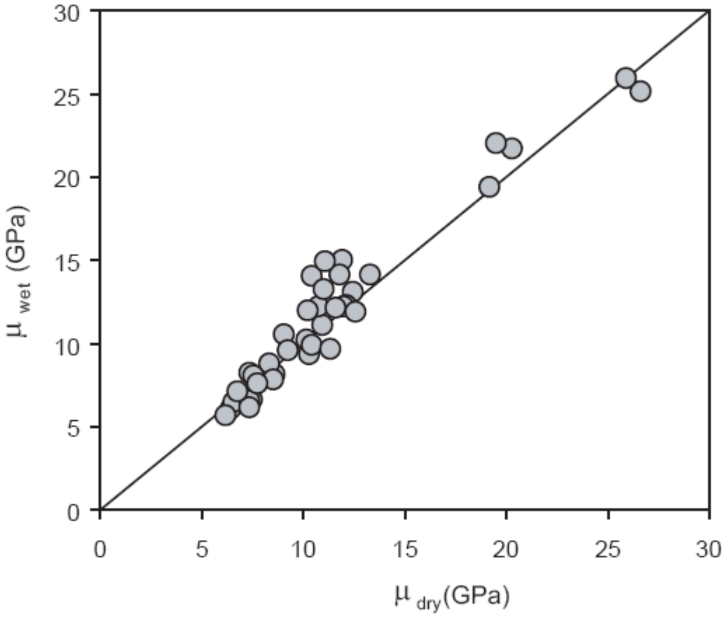

Figure 8: (a) Bulk modulus (K) of dry versus wet samples; Most samples show an increase in the bulk modulus under water-saturated conditions of up to 14 GPa. (b) With saturation the shear modulus decreases in some samples up to 3.8 GPa and increases in others up to 1.7 GPa.

Saturated samples, which show shear weakening, display consistently higher Vp/Vs ratios than their dry counterparts (Fig. 10). The Vp/Vs ratio of samples which show shear weakening increases by an average value of 0.2 when saturated, whereas the ratio in the rest of the samples show an average increase of only 0.1. Four samples that show unusual high saturated Vp/Vs ratio’s of 2 and higher, are displaying shear weakening.

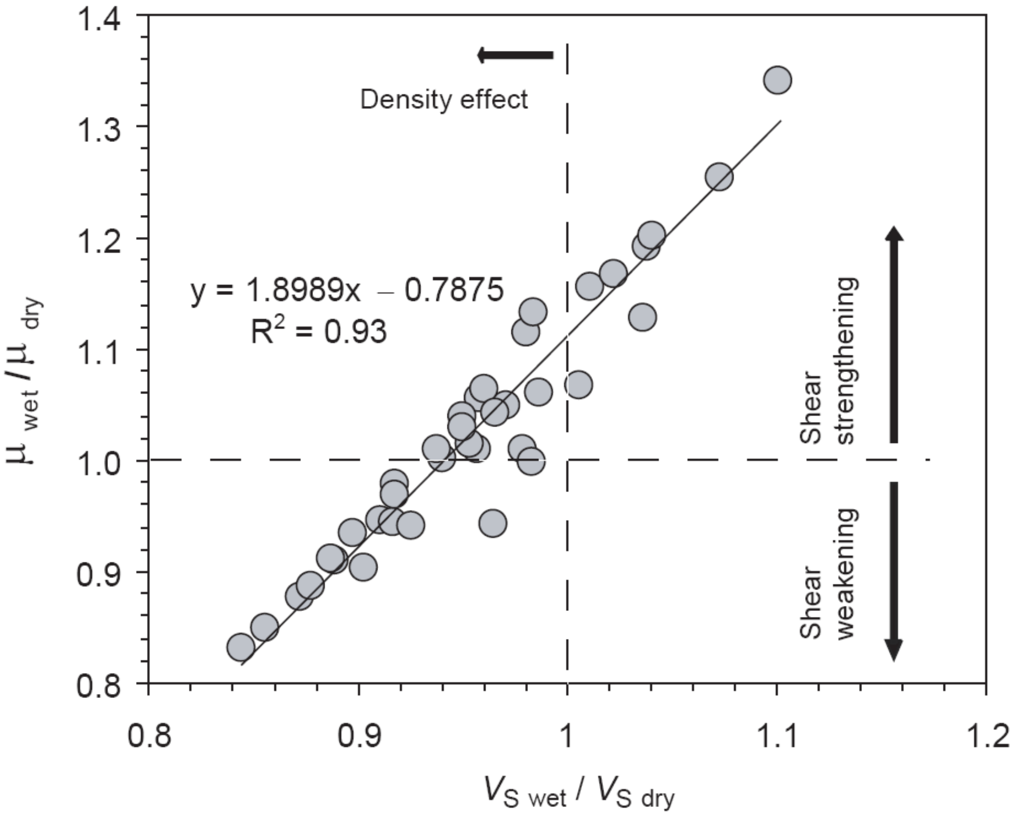

Figure 9: Plot of the fractional change in the shear modulus versus the fractional change in the shear velocity with saturation at 40MPa effective pressure. A decreasing shear modulus (shear weakening) is always related to a decrease in shear velocity, while an increase in the shear modulus (shear strengthening) competes with the density effect and thus both, a net decrease and a net increase, in velocity is observed in samples with shear strengthening.

Anselmetti et al. (1997) speculated that the larger scatter in Vp/Vs ratio at higher porosities is caused by the higher sensitivity of the shear wave to fabric weakening. Here we quantify the fabric weakening by calculating the shear modulus changes. Extreme high Vp/Vs ratios are caused by the lowering of the shear modulus beyond the density effect caused by water saturation (Figure 10). The high Vp/Vs ratios in the samples that show shear weakening indicate that the shear weakening affects Vs more than it affects Vp. This finding is in agreement with the conclusion of a sensitivity analysis performed by Wang (2000). He found that the Vp/Vs ratio is more sensitive to changes in the shear modulus than the bulk modulus, or any other input parameter for the Gassmann equation.

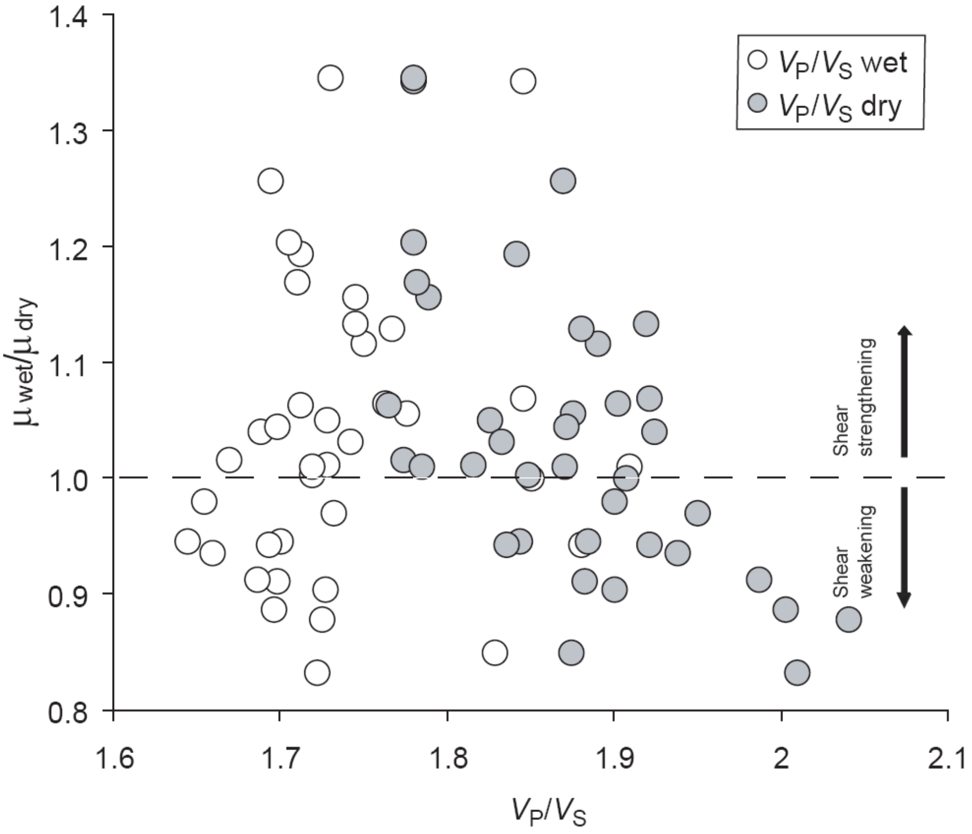

Figure 10: The ratio of wet to dry shear bulk modulus (μ_w/μ_d) versus the V_P/V_S ratio of both the wet and dry samples at 40 MPa effective pressure. The samples with shear weakening are prone to a large increase in V_P/V_S ratio under water saturation.

Is shear weakening permanent?

In order to explore whether shear weakening has altered permanently the frame properties with water saturation, six samples were re-measured in the dry state after a cycle of velocity measurements in dry state and subsequent fully water saturated. None of the four samples, which show shear weakening with water saturation, have permanent shear weakening of the rock frame (Table 2). In the two samples with the highest reduction in shear moduli with water saturation, the shear moduli return to the original strength after drying. This reversibility of shear weakening indicates no permanent changes in the rock’s microstructure during pressure loading or water saturation.

Gassmann’s equation and assumptions

Gassmann’s fluid substitution theory is based on the fact that rocks, in which the pore space is filled with a fluid that is less compressible than gas, become more resistant to compression (Gassmann, 1951). This bulk modulus (K_{Gass}) of a rock saturated with a fluid is calculated using the following equation:

$$K_{Gass} = K_d + \frac{(1 - K_d / K_g)^2}{\frac{\phi}{K_f} + \frac{1-\phi}{K_g} - \frac{K_d}{K_g^{\,2}}} \qquad (3)$$

Where,

K_f is the bulk modulus of the fluid, K_g is the grain modulus, K_d is the dry bulk modulus and ϕ is the porosity.

Several basic explicit and implicit assumptions must be valid for Gasssmann’s derivation of the bulk modulus after fluid substitution (Table 3). Assumption (1; Table 3) that the rock is macroscopically isotropic and homogeneous is supported by laboratory measurements of carbonates (Wang, 2002) at high frequencies. Thus the anisotropic form of Gassmann’s equation by Brown and Korringa (1975) is not used in this study.

Assumption (2; Table 3) means that the rock frame is made of a mono-mineral material. In order to comply with this assumption we analyzed the mineralogy using XRD, grain density data, and the petrographic thin section to guarantee a purely calcitic mineralogy.

Assumption (3; Table 3) says that the pore pressure is in equilibrium between pores. This is generally valid if the permeability is high, the viscosity of the fluid is sufficiently low, and the pores are not isolated from the pore network. This assumption is dependant on the wavelength, hence the frequency of the measurement. At zero wave frequencies, rocks meet this assumption (Wang, 2000). At low seismic frequencies, the pore pressure might not always be in equilibrium and therefore velocity dispersion might occur. Tight carbonates and rocks with low aspect ratio pores potentially behave dispersive at seismic frequencies (Batzle et al., 2006; Wang, 2000). At ultrasonic frequencies, rocks with nearly round pores show a small or negligible velocity dispersion (Wang, 2000).

Assumption (4; Table 3) is guaranteed by our experimental setup that does not allow pore fluid to escape. Assumption (5; Table 3) dismisses any chemical interaction between the fluid and the rock frame. The rock frame properties are not altered by the different fluid types, with the exception of the additional stiffening of the rock frame by the water. Under this assumption and the knowledge that the shear modulus of all fluids is zero, μ should not change during saturation in an isotopic, homogeneous rock:

$$\mu_{dry} = \mu_{wet} \qquad (5)$$

Thus, Gassmann's theory results in an independence of the rock's shear modulus from the pore fluid type (Berryman, 1999).

The two parameters bulk modulus (K_{Gass}) and shear modulus in equations (1) and (6) can be derived from dry Vp, dry Vs and density measurements. Using Gassmann's theory, the velocity of the rock saturated with fluid can be calculated with the following equation:

$$Vp_{Gass} = \sqrt{\frac{K_{Gass} + (4/3)\mu}{\rho}} \qquad (6)$$

In the following we will call this calculated velocity "Gassmann-predicted velocity" (Vp_{Gass}).

Implication of shear moduli changes for Gassmann applicability

Gassmann's theory was established for static measurement conditions, and thus it is not necessarily valid for ultrasonic measurements (Wang, 2001). Dispersive mechanisms due to micro-cracks and grain-to-grain contacts can cause ultrasonic velocity dispersion (Mavko, 2000). This velocity dispersion causes the measured ultrasonic velocity to be higher than the Gassmann-predicted velocity. The difference between Gassmann-predicted velocities and measured ultrasonic velocities is often attributed to these frequency effects between high and low frequency velocity values (Mavko, 2000). However, the difference between Gassmann-predicted velocities that is valid for low frequencies and velocities measured with high frequencies is commonly less than 3-5% (Marion and Jizba, 1997; Winkler, 1986).

One result of the Gassmann derivation is a constant shear modulus with different pore fluids (Berryman, 1999). However, in our ultrasonic experiments the shear modulus is not constant under changing pore fluids. It is possible (but unlikely) that the observed change in the shear modulus with changing pore fluids from gas to water-saturated is solely caused by the combined effect of velocity dispersion and anisotropy. The observed decrease in the shear modulus, however, can not be explained by the high frequency velocity dispersion, because it moves the shear modulus in the opposite direction. In fact, the observed shear weakening with water saturation is likely to be even larger at seismic frequencies, because the high frequency velocity dispersion is counteracting the weakening.

Adam et al. (2006) document shear modulus weakening due to brine saturation at seismic frequencies in an experimental study. A shear weakening at seismic frequencies would imply an inaccurate prediction of the saturated velocity using the Gassmann equation via the measured dry bulk modulus and dry shear modulus. In our dataset, we observe a positive correlation between changes in shear moduli and the failure of the Gassmann theory to predict the saturated p-wave velocities (Fig. 11). The Gassmann-predicted velocities are either higher or lower than the measured velocity of the saturated samples. Since the velocity dispersion is not limited to high frequencies, the Gassmann-predicted velocities might also be inaccurate under lower frequency conditions Such misfits of measured and predicted bulk moduli using the Gassmann theory at low seismic frequency have been reported by Adam et al. (2006).

Effect of shear modulus variation on compressional wave velocity

Figure 11a shows the change in the shear modulus versus the difference between the Gassmann-predicted and the measured p-wave velocity of the saturated samples. The Gassmann-predicted velocities both overestimate the p-wave velocities of the saturated samples by 400 m/s and underestimate the velocities of the saturated samples as much as

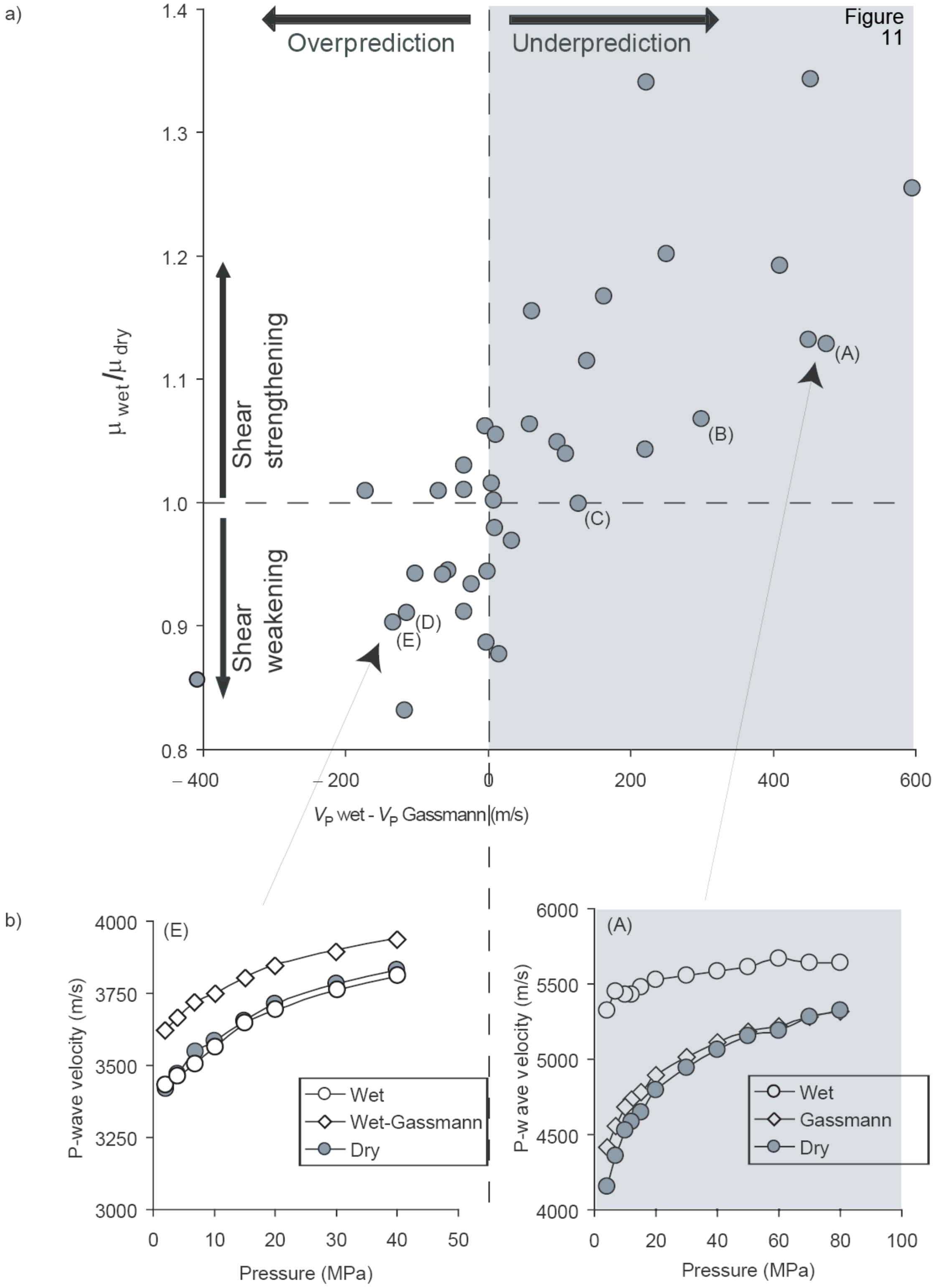
a)
Figure 11
Overprediction
Underprediction
Shear strengthening
Shear weakening
μ wet /μ dry
1.4
1.3
1.2
1.1
1.0
0.9
0.8
– 400
– 200
0
200
400
600
V_P wet - V_P Gassmann (m/s)
(A)
(B)
(C)
(D)
(E)
b)
(E)
4000
3750
3500
3250
3000
P-wave velocity (m/s)
0
10
20
30
40
50
Pressure (MPa)
Wet
Wet-Gassmann
Dry
(A)
6000
5500
5000
4500
4000
P-w ave velocity (m/s)
0
20
40
60
80
100
Pressure (MPa)
Wet
Gassmann
Dry

Fig. 11

Figure 11A (previous page): Plot of μ_w/μ_d versus $V_{P\ wet}$ - $V_{P\ Gassmann}$ at 40MPa displaying the changing shear moduli (μ_w/μ_d) effect on velocity prediction of saturated rocks using the Gassmann equation. The Gassmann-predicted velocity underestimates the measured velocity of the fully saturated samples in samples which display shear strengthening (μ_w/μ_d >1), while Gassmann overestimates the velocity in samples with shear weakening (μ_w/μ_d <1). Samples (A) to (E) are described in Figure 12. Figure 11b: Overestimation and underestimation of velocity of the saturated sample using the Gassmann equation is observed over the entire pressure range as illustrated in the velocity-pressure plots of sample (A) and (E).

600 m/s. In samples with shear strengthening the Gassmann-predicted velocity is too low whereas in samples with shear weakening the Gassmann-predicted velocity is too high. The good correlation of the change in shear moduli and the Gassmann-predicted velocity misfit (r^2=0.62) in Figure 11 indicates that the difference between the Gassmann-predicted velocity and the measured Vp of the saturated samples is caused predominantly by the change in the shear strength.

We observe, however, that in 13 samples with large changes in shear modulus, from -12% to +5% the Gassmann-predicted velocity is very close (within 50 m/s) to the measured Vp of the saturated samples. Those 13 samples have Gassmann-predicted velocities which are within the 3% measurement precision. Consequently, 34% of our Gassmann-predicted velocities fit the measured water-saturated velocities within the error range of our measurements. 8 samples show essential no change in the shear modulus with saturation (+/- 2%). In these 8 samples the Gassmann-predicted Vp is 172m/s above the measured velocity or up to 127m/s below the measured velocity. Consequently, in these samples no significant Gassmann-overprediction is associated with the shear strenghtening (upper left quarter in Fig. 11a), nor any significant Gassmann-underprediction with the shear weakening (lower right quarter in Fig. 11a).

The role of rock texture and pore types on shear modulus variation

Khazanehdri and Sothcott (2003) observe in sandstones an increased shear weakening with increasing surface area. They take this correlation as a proof that the rock microstructure is an important factor influencing the shear modulus. Carbonates characteristically display a large variability in pore types that influence sonic velocity (e.g. Eberli et al., 2003). These pore types are also expected to play a certain role in the shear weakening and strengthening. Thin section analyses of each sample reveal indeed a relationship between pore types and shear modulus changes. Samples of interparticle and intercrystalline porosity show extreme high shear modulus variation, whereas an intraframe coral sample shows no change. To illustrate the results five end member samples are selected and marked by letters (A-E) in succession from shear strengthening to shear weakening (Fig. 11a and 12). Samples (A) and (B) are intercrystalline end member pore types that show shear strengthening. Shear strengthening is, however, not limited to rocks with intercrystalline pore types, but also include rocks with grainstone and packstone textures and with dominantly interparticle and moldic pore types. Sample (D) and (E) are grainstones with high amount of microporosity, which are prone to show shear weakening and Gassmann overprediction (Fig. 11a).

Figure 11b displays the difference of two samples between the Gassmann-predicted velocities and the measured velocities over the entire range of confining pressures from 4 MPa up to the maximal pressure reading of 40 and 80 MPa, respectively. Sample (A) is a recrystallized grainstone with intercrystalline and vuggy-moldic porosity, which under saturation has a distinct higher velocity in the low-pressure regime and a convergence with the Gassmann-predicted velocity at higher pressures (Fig. 11b). In contrast, a peloidal and echinoid-dominated grainstone to packstone with interparticle porosity and a high amount of microporosity shows Gassmann-overprediction over the entire pressure regime (sample E on Fig. 11b).

Figure 12 displays thin section images of samples (A) to (E) and some of their physical properties. No clay was detected in the thin sections of these samples, indicating that all fine grained-particles are carbonate mud. The samples are selected to represent the variations of pore types common in carbonate rocks. They also show a wide range of shear modulus variation with saturation and the resulting variation in the Gassmann velocity prediction (Fig. 11a). Both recrystallized limestones (A) and (B) display shear strengthening although they differ in crystal size. The average crystal size in sample (A) is 100 µm and in sample (B) 500 µm. An intraframe coral sample (C) shows no change in shear modulus with saturation. The grainstone samples (D) and (E) show shear weakening. Both have a high amount of microporosity and variable grains sizes (0.1 mm to 2mm (D), 0.05 mm to 0.5 mm (E)).

Based on our data set, we speculate that samples with interparticle and intercrystalline porosity show high shear modulus variations with saturation. Recrystallized limestones with flat grain-to-grain contacts have exclusively shear strengthening (Fig. 12A and 12B). However, several packstones to grainstones with mixed interparticle to moldic pore types are also showing shear strengthening. Samples with shear weakening are dominated by grainstones with high amount of microporosity and small grain-to-grain contacts (Fig. 12D and 12E).

In sandstone models, grain contacts are the key element controlling the velocity dispersion and an important factor controlling the modulus reduction when saturated with water (Murphy et. al., 1986; Wulff and Burkhardt, 1997). Grain-to-grain contacts seem also to be important in the measured carbonates. The amount of porosity is important for density effects on velocity, while the grain-to-grain (or crystal/crystal) contacts are important for stiffening and weakening effects with fluid changes. For example, flat intercrystalline pores between crystal faces in recrystallized carbonates are associated with shear strengthening (Fig. 13). In the recrystallized sample displayed in Figure 13B individual crystals are as small as 10 µm in diameter and have low aspect ratio pores along crystal faces. In contrast, a grainstone which shows shear weakening after saturation, displays predominantly point contacts between grains/crystals that are as small as 5 µm in diameter. The pores have a medium to high aspect ratio (Fig. 13A).

In summary samples showing shear weakening are characterized by a decrease in the shear moduli with saturation and generally a Gassmann overprediction of velocity. The shear modulus in carbonate rocks appears to change according to the dominant pore type. Grainstones with high amount of microporosity are more likely to have an overpredicted velocity using Gassmann equation by approx. 3.5% (one sample by 10%), whereas in intercrystalline recrystallized rocks the velocity of the saturated samples tends to be underpredicted by up to 13%. Pore types play therefore a critical role in predicting velocity changes with saturation at ultrasonic frequencies. Assuming that the pore type also influences larger rock volumes and is present when using lower frequency acoustic

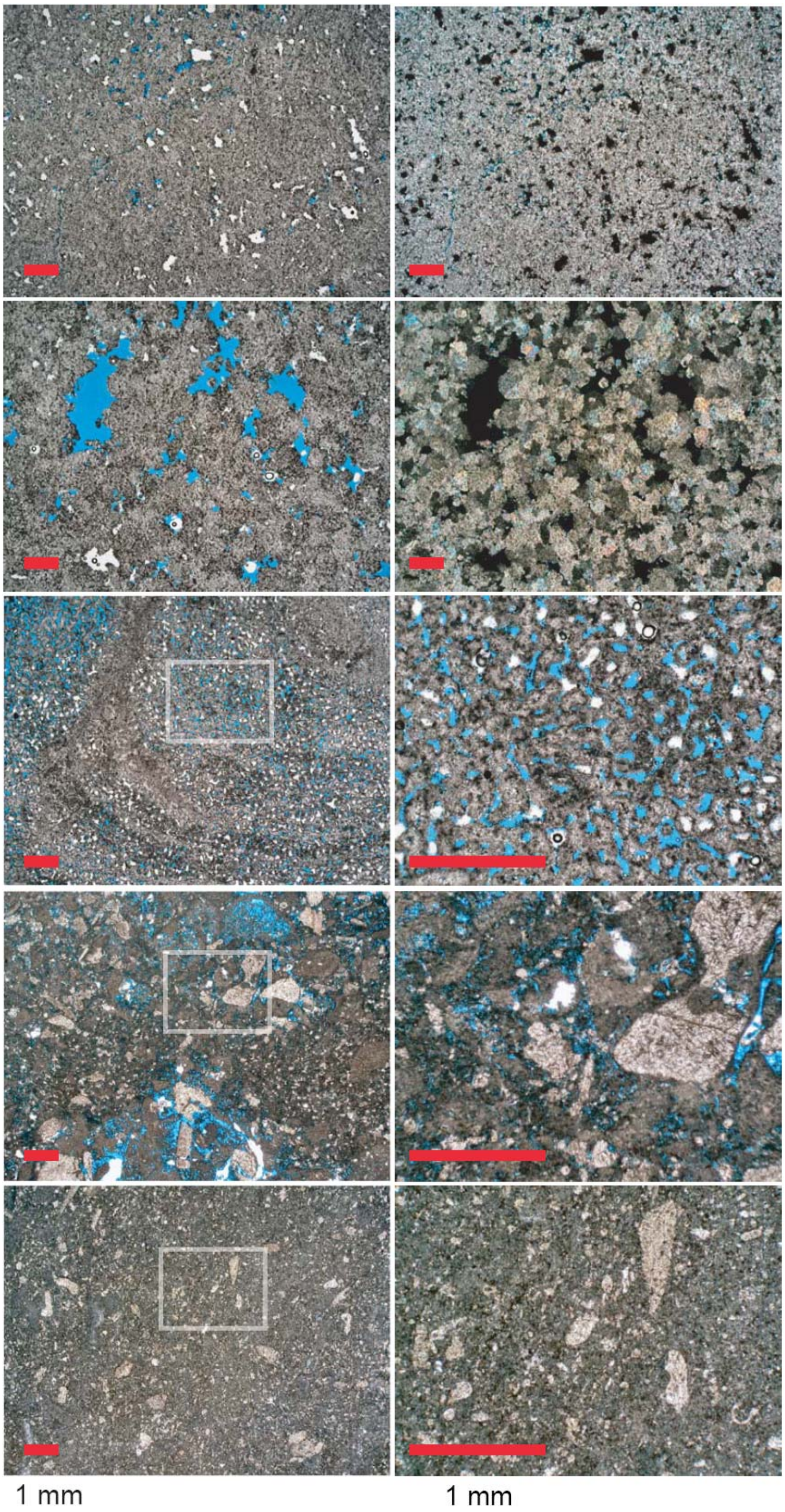

(a)
$\mu_{wet/dry}$: 1.128
ϕ: 0.12 (%)
V_{Pdry}: 5066 (m/s)
Perm: 150 (mD)
Miocene recrystalized limestone, intercrystaline pore type with minor molds and vugs

(b)
$\mu_{wet/dry}$: 1.067
ϕ: 0.13 (%)
V_{Pdry}: 5438 (m/s)
Perm: 150 (mD)
Miocene recrystalized limestone, vuggy pore type, with minor intercrystaline porosity

(c)
$\mu_{wet/dry}$: 0.999
ϕ: 0.08 (%)
V_{Pdry}: 5987 (m/s)
Perm: 3.7 (mD)
Miocene coral framestone with intraparticle porosity

(d)
$\mu_{wet/dry}$: 0.91
ϕ: 0.29 (%)
V_{Pdry}: 3594 (m/s)
Perm: 71.54 (mD)
Cretaceous peloidal, foraminiferal, and echinoidal grainstone with interparticle porosity

(e)
$\mu_{wet/dry}$: 0.903
ϕ: 0.23 (%)
V_{Pdry}: 3831 (m/s)
Perm: 2.31 (mD)
Cretaceous peloidal, foraminiferal, and echinoidal grainstone with interparticle porosity

Fig. 12

Figure 12 (previous page): Physical properties, textural and pore type description, and thin section images of samples (a) to (e) arranged by decreasing shear strength with water saturation. Sample (a) and (b) are re-crystallized limestone samples which show shear strengthening with different calcite crystals. The left image is acquired in plain light, the right image in crossed polarized light. Sample (c) shows no change in shear strength after saturation. Samples (d) to (e) show shear weakening. Left images of samples c, d, and e are taken at a magnification of 1 x. The white rectangle marks the position of the higher magnification image of the right side. Scale bars are 1 mm.

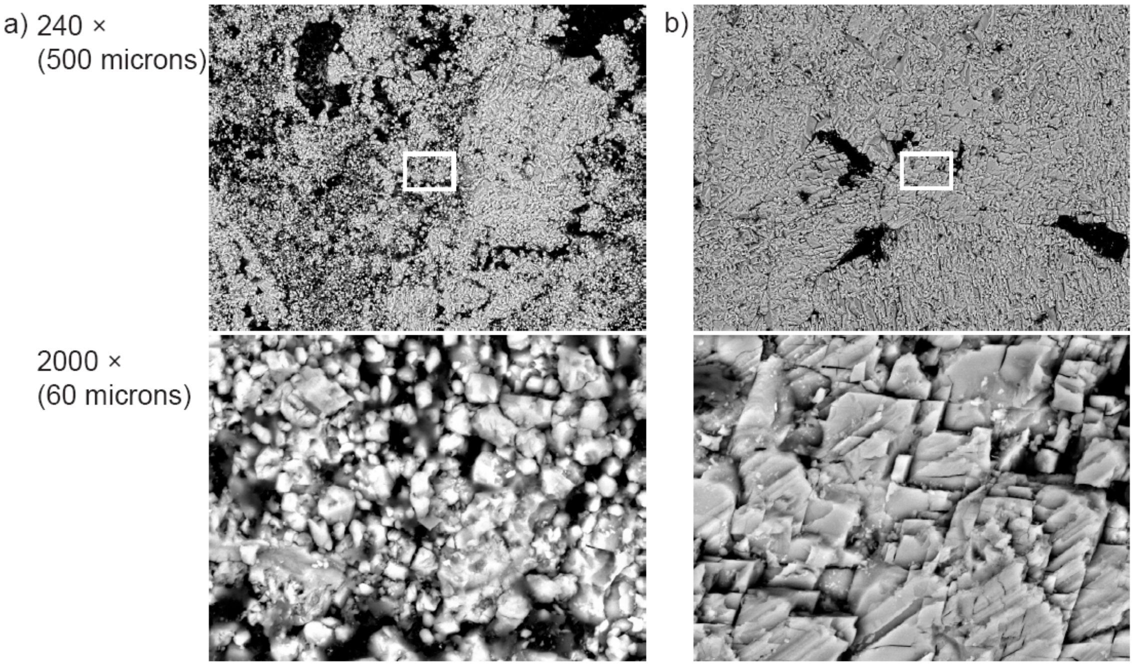

$\mu_{wet/dry} = 0.969$

Zoom into packstone portion of a Miocene skeletal grainstone-packstone, illustrating the nature of grain contacts in the interparticle mud

$\mu_{wet/dry} = 1.067$

Miocene recrystalized limestone, dominant vuggy pore type, with minor intercrystaline porosity

Figure 13: ESEM images of two samples at two different magnifications that have been acquired before pressure loading. The packstone portion of a Miocene skeletal grainstone-packstone (a) that shows shear weakening after saturation has predominantly point contacts between grains, with high aspect area pores. The recrystallized Miocene limestone sample (b) that shows shear strengthening has larger grain-grain contacts, with flat, low aspect ratio pores.

sources, Gassmann fluid-substitution might carry a large uncertainty in fluid monitoring studies at log scale or in 4D seismic surveys.

Effect of pressure loading and anisotropy on shear modulus

Fluid saturation causes significant changes in the shear modulus but with increasing pressure those changes decrease non-linearly. We observe both, decreasing shear weakening and decreasing shear strengthening with increasing pressure (Fig. 14). In addition, with increasing pressure the misfit of Gassmann-predicted velocities is reduced (Fig. 14). In most of our samples, p-wave velocity increases logarithmically with pressure. A fine-grained peloidal-skeletal grainstone (sample 101) dominated by microporosity shows a logarithmic increase of velocity with pressure with a slope of the regression trend of 2.6 (Fig. 15). A recrystallized limestone (sample 27) with vuggy-intercrystalline porosity shows a strong increase in velocity with pressure and a slope of the regression trend of 9.1 (Fig. 15). The slope of the logarithmic regression curve is an indicator of the pressure sensitivity; the stronger the pressure sensitivity, the steeper the slope of the regression curve. A positive correlation exists between the slope of the pressure curve and changes in the shear moduli with water saturation (Fig. 16). The more pressure sensitive a sample is (steeper slope), the more shear strengthening we observe. The pressure dependence of the shear variability (Fig. 14) supports the idea of the shear weakening being related to the type of grain contacts present in the sample. Gaps between grains will close at elevated pressures. Consequently, the forces associated with the pore fluid diminish. Surface free energy, for example, weakens the rock by a process in which water molecules absorb onto the surface of the grains, hereby weakening the grain contacts (Tutuncu and Sharma, 1992; Murphy et. al., 1984). This process could be responsible for the observed shear weakening, because increasing pressure would increase the size of individual grain-to-grain contacts and create new contacts that reduce the overall surface area. As a result, both, free surface energy and shear weakening, are reduced. Local flow due to velocity dispersion is one mechanism that has the potential to increase the shear strength at high frequencies. Mavko and Jizba (1991) showed that the shear and bulk dispersion are proportional to each other. This velocity dispersion effect is caused by the high frequency of the acoustic signal, where high aspect ratio pores between grain-grain contacts are isolated for flow and the overall rock frame appears stiffer than at low frequencies. With increasing pressure the closing of grain-grain contacts reduces this effect, as observed in those samples from our dataset that show shear strengthening (Fig. 14c and 14d). The positive correlation in our samples between shear strengthening with water saturation and pressure sensitivity of Vp (Fig 16) indicate that rocks with compliant pores (steep slopes) show shear strengthening. This fact suggests that not all compliant pores are closed at elevated high pressures of 40 MPa. Considering that the shear variation is masked by additional stiffening effects at high frequencies and low pressures, the net shear weakening effect is more pronounced at lower frequencies. Khazanehdari and Sothcott (2003) show that the wet shear velocity below ultrasonic frequencies shows no significant frequency strengthening effect compared to the dry measurement. As illustrated in Figure 16, samples with small pressure effects on velocity (slopes < 4) are prone to exhibit either (a) no changes in the shear modulus or (b) shear weakening with water saturation.

Macroscopically no anisotropy is observed in our plug samples. The change in velocity of the two independently orthogonally polarized shear waves is used as an indicator of anisotropy within the sample. The difference of the shear wave velocity is for most samples within ±2%, i.e. within the measurement precision. Only 8 samples show a difference of ±4%. This small shear anisotropy does not correlate with the observed changes in the shear modulus with water saturation and appears to be random. Hence in our dataset, anisotropy is considered to be an insignificant factor affecting shear modulus changes.

Causes for shear weakening

Changes in shear modulus have been attributed to several mechanisms including viscous coupling, reduction in free surface energy and velocity dispersion due to local flow (Khazanehdari and Sothcott, 2003). Atkinson (1984) shows in his extensive review that

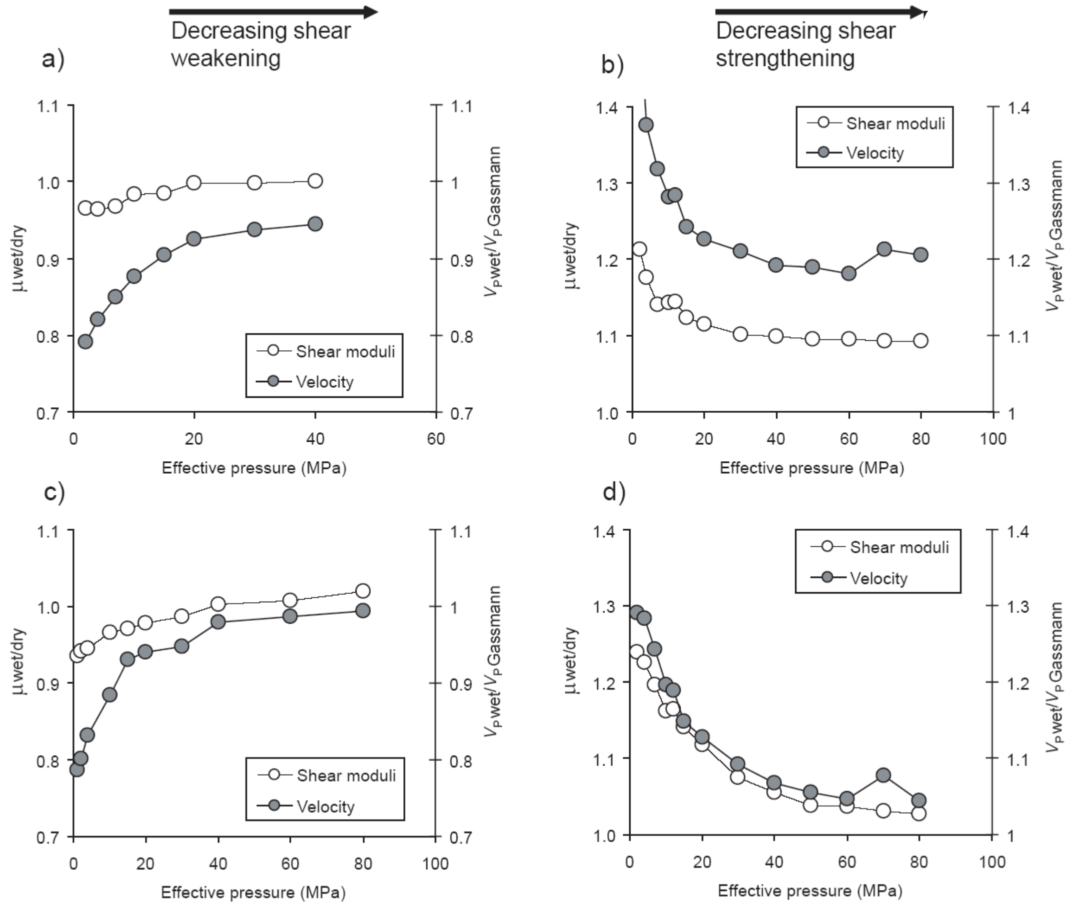

Figure 14: Changes in the shear modulus with saturation (μ_w/μ_d-ratio's) at different effective pressures (white dots) compared to the difference between measured and Gassmann-predicted velocities (grey dots). Shear strengthening and shear weakening is highest at low pressures. With increasing pressure the values decreases and reach a plateau of constant values at around 40 MPa. (a) Fine grained peloidal grainstone with some skeletal fragments with moldic pore type and a small amount of intra-frame and microporosity. (b) Highly micritised foraminiferal peloidal grainstone with interparticle macroporosity, intermediate-high microporosity and few molds. (c) Recrystallized limestone with large crystal size and vuggy macroporosity with a low amount of microporosity, and minor intercrystalline porosity. (d) Skeletal grainstone-packstone with a recrystallized matrix. The dominant macropore type is moldic,a few intercrystalline pores, and an intermediate amount of microporosity.

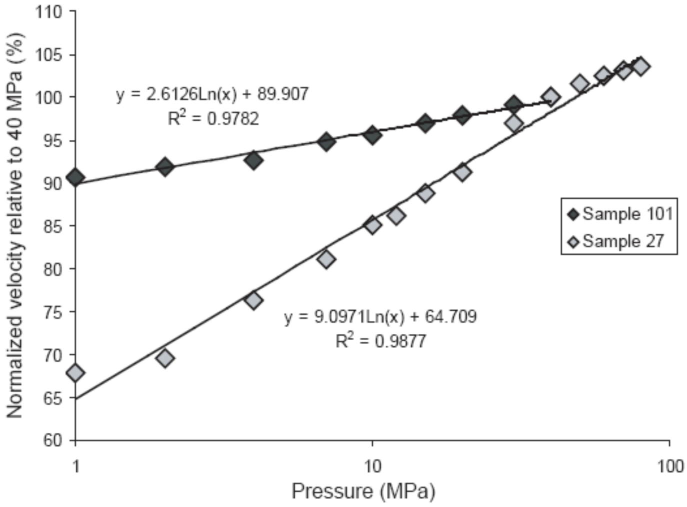

Fig. 15: Plot of normalized p-wave velocity versus differential pressure of two samples. The samples show a good correlation of the best fit least square logarithmic regression curve.

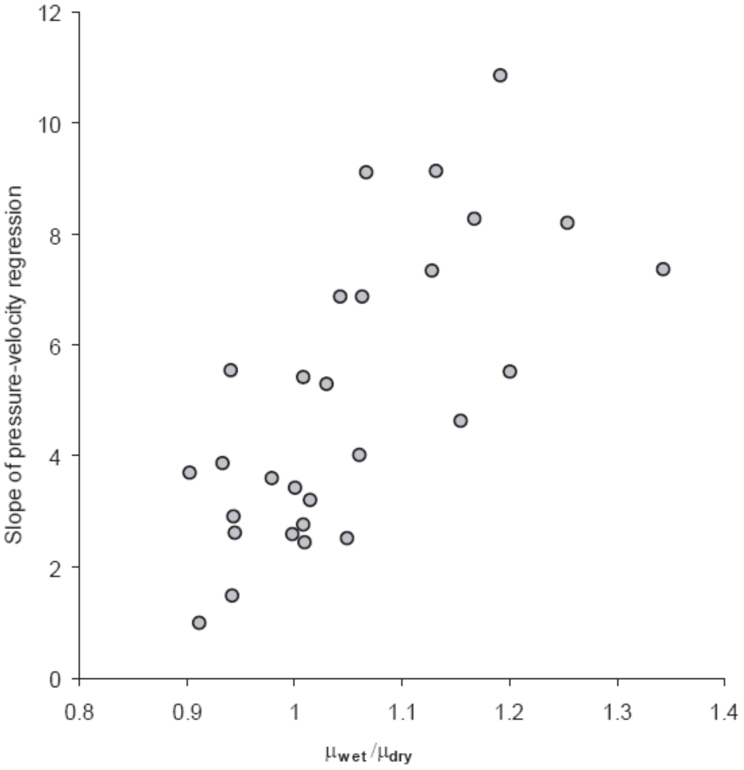

Fig. 16: Slope of the logarithmic pressure-velocity regression curve versus the ratio of the wet / dry shear moduli (excludes samples with small correlation coefficient $r^2 < 0.95$ of the pressure-velocity regression analysis). The steeper the slope, the stronger is the increase of the shear moduli with saturation.

water is most effective in weakening rocks. Murphy et al. (1986) emphasizes that the weakening effect is caused by the reduction in surface energy of the minerals when in contact with water, indicating that shear weakening occurs as a result of rock-fluid interaction. In the case of water, the fluid can bond to the solid surface of the mineral, break the solid – solid bonds and hereby reduce activation energy (Murphy et al., 1986). The weakening effect of water on sandstones at elevated pressures in static experiments shows that the yield strength, when the onset of shear-enhanced compaction occurs (void collapse), is lower under water-saturated conditions (Baud et al., 2000, Zhu and Wong, 1997). Baud et al. (2000) explain shear weakening by the fact that specific surface energy is lowered by water. Zhu and Wong (1997) observe that the void collapse results from intragranular cracking that originates at grain contacts.

Studies about the mechanisms of water weakening in carbonate rocks focused mostly on chalks because water injection weakens North Sea chalk reservoirs (Guilbot and Smith, 2002). Risnes and Flaageng (1999) and Gutierrez et al. (2000) suggest that with water injection, a collapse of the initial menisci bounding of the grains occurs. Capillary forces are unlikely to be the only weakening mechanism because chalk saturated with methanol, which is miscible with water and should therefore also reduce the capillary forces, shows no weakening (Risnes and Flaageng, 1999). Gutierrez et al. (2000) conclude that water weakening of chalk is “a combination of capillary pressure, which accounts for the instantaneous volume change and reduction in apparent cohesion, and chemical dissolution/grain surface modification, which accounts for the reduction in frictional strength and some of the volumetric change”. Dissolution and the thereby induced changes in surface properties most likely take place at the grain contacts. As in our data, Risnes and Flaageng (1999) observed a reversible weakening effect in their dataset. They propose a two element model for rock-water interaction mechanisms where “repulsion forces of electrostatic origin generated by the fluid film in the contact area between the grains and attractive forces due to the capillary effects when the chalk is not fully saturated with the wetting fluid”.

Very little is known about water weakening effects in shallow-water carbonates. In the field of rock mechanics, carbonate rocks have been primarily be investigated under dry condition (Vajdova et al., 2004). Recently, Carles and Lapoint (2004) performed laboratory compressibility tests of shallow-water carbonate samples under oil and water-saturated conditions. They found that, unlike the oil saturated samples, the brine saturated sample exhibit additional and irreversible deformation during pressure loading, such as broken micritic bonding, disrupted microsparite rims, and fractured crystals. As little as 5% water saturation was sufficient to cause weakening of the rocks (Carles and Lapoint, 2004). Furthermore, they describe a positive correlation between compressibility and porosity, the higher the porosity the higher the compressibility during pressurization. Triaxial sliding experiments show that the frictional strength of calcite dropped 15% after water saturation (Morrow et al., 2000), indicating rock-water interaction causing shear weakening effect. In this study, we conclude that pore structure is an additional factor influencing the rocks ability to be affected by shear weakening.

Conclusion

Ultrasonic compressional and shear wave velocities of 38 limestone samples with a wide range of pore types under dry and fully water-saturated conditions document the effect of changes in pore fluids on acoustic properties of carbonates. The high frequency (1 MHz) laboratory fluid substitution experiments are carried out under differential pressure ranging from 2 MPa to a maximum of 80 MPa. In these carbonates, water saturation causes increasing and decreasing velocities, shear moduli, in addition to bulk modulus dispersion effects, stiffening of the bulk modulus, and effects on velocity due to the increase in density.

The most unexpected result of these laboratory experiments in regards to velocity is the wide range of Vs change in the saturated samples. In most samples Vs decreases under saturated conditions but 25% of the measured samples show an increase of Vs by up to 230 m/s. Likewise, water saturation significantly decreases shear modulus in carbonates up to 2 GPa or increases it up to 3 GPa. The average increase in shear modulus with water saturation is 1.23 GPa, the average decrease is 0.75 GPa. The shear modulus changes are pressure dependent, with a decrease in shear variations with increasing pressure. We observe shear weakening and shear strengthening, which affect indirectly the velocity of the compressional wave. In saturated samples that show shear weakening we observe highest Vp/Vs ratios, although all saturated samples have a distinctly higher Vp/Vs ratio than the unsaturated samples. In summary, a constant shear modulus with fluid changes, a consequence of Gassmann's derivation, is not observed in most of our samples and probably not valid for most carbonate rocks.

Consequently, in 66% of our samples we observe a misfit between Gassmann-predicted p-wave velocity and measured p-wave velocity. We observe a positive correlation between inaccurate Gassmann predicted p-wave velocity and shear modulus changes at high frequencies. The change in shear modulus is the main cause for the difference between measured velocities and Gassmann-predicted velocities. The factors, which are causing the change of the shear modulus are not well understood but are generally assumed to be related to rock-fluid interactions whose amount is related to the pore structure and the grain-grain contact. Preliminary results from our data set suggest connection to the pore types and grain-to-grain contact geometry. For example, samples with a high amount of micorporosity tend to show a shear weakening with saturation while samples with predominantly intercrystalline porosity show shear strenghtening. It is a well-established fact that pore type variations can cause variations of compressibility at any given porosity. Our findings indicate that it might also have a control on shear modulus variation.

The main implications of this study are: 1) The observed shear modulus variation reduces the applicability of the Gassmann theory for velocity prediction in carbonates at high frequencies. These results also merit a critical evaluation of Gassmann's applicability in the lower frequency realm. 2) Velocity dispersion mechanisms are assumed to strengthen the shear modulus in saturated samples, whereas rock-fluid interaction at grain contacts is assumed to weaken the rock frame properties. The weakening of the shear modulus with water at low frequencies is likely to be even larger than observed at high frequencies, because frequency velocity dispersion potentially counteracts some of the weakening (under the assumption that velocity dispersion is limited to high frequencies).

Table 1: Effects of water saturation on V_P, V_S and V_P/V_S caused by four mechanisms in carbonates (V_{Gass} = Gassmann-derived water-saturated velocity, K = bulk modulus, μ = shear modulus, ⇑ = increase, ⇓ = decrease). (A) and (B) are theoretical mechanisms, whereas (C) and (D) are experimental observations.

Effects of gas–to-water substitution	Modulus	V_P	V_S	V_P/V_S	V_P/V_{Gass}
(A) Compressibility decrease	K⇑	⇑	-	⇑	-
(B) Bulk-density increase	-	⇓	⇓	-	-
(C) Shear strengthening	μ⇑ , K⇑	⇑	⇑	⇑	⇑
(D) Shear weakening	μ⇓ , K⇑	⇓⇑	⇓	⇑	⇓

Table 2: Table showing changes in shear modulus with changing saturation conditions from dry conditions (first run) to fully water-saturated conditions (second run) and a third run in dry conditions. Sample a, c, d, and e show shear weakening with water saturation.

Sample	Pressure (MPa)	Shear modulus dry-1st run (GPa)	Shear modulus sat-2nd run (GPa)	Shear modulus dry-3rd run (GPa)	Dry-bulk density (g/cm^3)	Porosity (%)
a	10	7.46	7.29	8.42	2.01	24.16
b	10	6.16	6.24	6.68	1.91	29.96
c	10	7.35	7.22	7.56	1.94	28.68
d	10	9.51	8.58	9.51	2.05	24.56
e	10	6.61	6.24	6.68	1.93	28.93
f	10	8.35	8.38	8.51	1.96	27.91

Table 3: Gassmann's assumptions.

1. The rock is macroscopically isotropic and homogeneous,

2. The rock is monomineralic (no mixtures of different minerals).

3. The pore space is interconnected.

4. The rock-fluid system is closed (undrained).

5. The pore fluid does not chemically interact with the frame.

References

Adam, L., M. Batzle, and I. Brevik, 2006, Gassmann's fluid substitution and shear modulus variability in carbonates at laboratory seismic and ultrasonic frequencies: Geophysics, v.71, p.173-183.

Agersborg, R., T.A. Johansen, and M. Jakobsen, 2005, The T-matrix approach for carbonate rocks: SEG Technical Program Expanded Abstracts, p.1597-1600.

Aharonov, E., D.H. Rothman, and A.H. Thompson, 1997, Transport properties in sedimentary rocks; role of micro-scale geometry: Geology, v.25, p.547-550.

Anguy, Y., S. Belin, D. Bernard, B. Fitz, and J.B. Ferm, 1998, Modeling physical properties of sandstone reservoirs by blending 2D image analysis data with 3D capillary pressure data: Phys. Chem. Earth (A), v.24, p.581-586.

Anselmetti, F.S. and G.P. Eberli, 1993, Controls on sonic velocity in carbonates: Pure and Applied Geophysics, v.141, p.287-323.

Anselmetti, F.S. and G.P. Eberli, 1997, Sonic velocity in carbonate sediments and rocks. In: Carbonate Seismology, v.6 (eds. I. Palaz & K.J. Marfurt), p.53-74, Society of Exploration Geophysicists.

Anselmetti, F.S., G.A. von Salis, K.J. Cunningham, and G.P. Eberli, 1997, Acoustic properties of Neogene carbonates and siliciclastics from the subsurface of the Florida Keys: Implications for seismic reflectivity: Marine Geology, v.144, p.9-31.

Anselmetti, F.S., S. Luthi, and G.P. Eberli, 1998, Quantitative characterization of carbonate pore systems by digital image analysis: AAPG Bulletin, v.82, p.1815-1836, 16 Figs.

Anselmetti, F.S. and G.P. Eberli, 1999, The Velocity-Deviation Log: a tool to predict pore type and permeability trends in carbonate drill holes from sonic and porosity or density logs: AAPG Bulletin v.83, p.450-466.

Aplin, G.F. and A.K. Sapru, 2001, Characterization of carbonate reservoir heterogeneity using probe permeability images, petrography and borehole image logs data: Society of Core Analysts, SCA-2001-41, International Symposium Proceedings, CD-ROM, 3 p.

Archie, G.E., 1952, Classification of carbonate reservoir rocks and petrophysical considerations: AAPG Bulletin, v.36, p.278.

Assefa, S., C. McCann, and J. Sothcott, 2003, Velocities of compressional and shear waves in limestones: Geophysical Prospecting, v.51, p.1-13.

Atkinson, B.K.A., 1984, Sub-critical crack growth in geological materials: Journal of Geophysical Research, v.89, p.4077-4114.

Baechle, G.T., R. Weger, G.P. Eberli, and Massaferro, J.-L. 2004, The role of macroporosity and microporosity in constraining uncertainties and in relating velocity to permeability in carbonate rocks: SEG Technical Program Expanded Abstracts, v.23, 1662-1665.

Batzle, M.L., D.-H. Han, and R. Hofmann, 2006, Fluid mobility and frequency-dependant seismic velocity – Direct measurements: Geophysics, v.71, p.N1-N9.

Baud, P., W. Zhu and T. F. Wong, 2000, Failure mode and weakening effect of water on sandstone: Journal of Geophysical Research, v.105, p.16.371-16.389.

Berge, P. A., J.G. Berryman, and B.P. Bonner, 1993, Influence of microstructure on rock elastic properties: Geophysical Research Letters, v.20, p.2619-2622.

Berge, P.A., B.P. Bonner, and J.G. Berryman, 1995, Ultrasonic velocity-porosity relationships for sandstones analogs made from fused glass beads: Geophysics, v.60, p.108-119.

Berryman, J.G., 1980, Long-wavelength propagation in composite elastic media: Journal of the Acoustic Society of America, v.68, p.1809-1831.

Berryman, J.G., 1999, Origin of Gassmann's equations: Geophysics, v.64, p.1627-1629.

Birch, F., 1960, The velocity of compressional waves in rocks to 10 kbars, part 1: Journal of Geophysical Research, v.65, p.1083-1102.

Blair, S. C., P.A. Berge, and J.G. Berryman, 1996, Using two-point correlation functions to characterize microgeometry and estimate permeabilities of sandstones and porous glass: Journal of Geophysical Research, v.101, p.359-375.

Brie, A., D.L. Johnson, and R.D Nurmi, 1985, Effect of spherical pores on sonic and resistivity measurements: SPWLA twenty-sixth annual logging symposium, June 17-20, 1985.

Brown, R. and J. Korringa, 1975, On the dependence of the elastic properties of a porous rock on the compressibility of the pore fluid: Geophysics, v.40, p.606-616.

Cantrell, D.L. and Hagerty, R.M. 1999, Microporosity in Arab Formation Carbonates, Saudi Arabia: GeoArabia, v.4, p.129-154.

Carles, P. and P. Lapointe, 2004, Water-weakening of under stress carbonates: new insights on pore volume compressibility measurements, SCA Annual International Symposium, v.27, p.1-12.

Castagna, J.P., M.L. Batzle, and T.K. Kan, 1993, Rock physics – The link between rock properties and AVO response, in J. P. Castagna and M. M. Backus, eds., Offset-dependent reflectivity – Theory and practice of AVO Analysis: SEG, p.135-171.

Cerepi, A., C. Durand, and E. Brosse, 2002, Pore microgeometry analysis in low resistivity sandstone reservoirs: Journal of Petroleum Science and Engineering, v.35, p.205-232.

Choquette, P.W. and Pray, L.C. 1970, Geologic nomenclature and classification of porosity in sedimentary carbonates: AAPG Bulletin, v.54, p.207.

Colpaert, A., 2007, Geophysical characterization of Carboniferous-Permian carbonate platforms in the Barent Sea based on 3D-seismic data analysis and rock physics modelling, PhD thesis at University of Tromsø, Norway.

Crabtree, S.J., Jr., R. Ehrlich, and C. Prince, 1984, Evaluation of strategies for segmentation of blue-dyed pores in thin sections of reservoir rocks: Computer Vision, Graphics and Image Processing, v.28, p.1-18.

Dunham, R.J., 1962, Classification of carbonate rocks according to their depositional texture, i.n W. E. Ham, ed., Classification of carbonate rocks: AAPG Memoir No. 1, p.108-121.

Eberli, G.P., G.T. Baechle, F.S. Anselmetti, and M.L. Incze, 2003, Factors controlling elastic properties in carbonate sediments and rocks: The Leading Edge, v.22, p.654-660.

Ehrenberg, S.N., G.P. Eberli, and G.T. Baechle, 2006, Porosity-permeability relationships in Miocene carbonate platforms and slopes seaward of the Great Barrier Reef, Australia (ODP Leg 194, Marion Plateau). Sedimentology v.53, p.1289-1318.

Ehrlich, R., S. J. Crabtree, K.O. Horkowitz, and J.P. Horkowitz, 1991, Petrography and reservoir physics I: objective classification of reservoir porosity: AAPG Bulletin, v.75, p.1547-1562.

Ehrlich, R., S. J. Crabtree, S.K. Kennedy, and R.L. Cannon, 1984, Petrographic image analysis I; analyses of reservoir pore complexes: Journal of Sedimentary Petrology, v.54, p.1365–1376.

Enos, P. and L.H. Sawatsky, 1981, Pore networks in Holocene carbonate sediments: Journal of Sedimentary Research, v.51, p.961-985.

Eshelby, J.D., 1957, The determination of the elastic field of an ellipsoidal inclusion, and related problems: Proc. Roy. Soc., A241, p.376-396.

Etris, E.L., D.S. Brumfield, R. Ehrlich, and S.J. Crabtree, Jr., 1988, Relations between pores, throats and permeability; a petrographic/physical analysis of some carbonate grainstones and packstones: Carbonates and Evaporites, v.3, p.17-32.

Fabricius, I. L., G.T. Baechle, G. P., Eberli, and R. Weger, 2007, Estimating permeability of carbonate rocks from porosity and vP/vS: Geophysics v.72, no. 5, p.E185–E191.

Fens. T.W.F., 2000, Petrophysical Properties from Small Rock Samples Using Image Analysis Techniques. Delft Univ. Press, Netherlands.

Ferm, J. B., R. Ehrlich, and G.A. Crawford, 1993, Petrographic image analysis and petrophysics: analysis of crystalline carbonates from the Permian Basin, west Texas: Carbonates & Evaporites, v.8, p.90-108.

Gassmann, F., 1951, Über die Elastizität poröser Medien: Vierteljahresschrift der Naturforschenden Gesellschaft in Zürich, v.96, p.1-23.

Guilbot, J. and B. Smith, 2002, 4-D constrained depth conversion for reservoir compaction estimation: Application to Ekofisk Field: The Leading Edge, p.302-308.

Gutierrez, M., L.E. Oino, and K. Hoeg, 2000, The effect of fluid content on the mechanical behaviour of fractures in chalk: Rock Mechanics and Rock Engineering, v.33, p.93-117.

Hamilton, E. L., G. Shumway, H.W. Menard, and C.J. Shipek, 1956, Acoustic and other physical properties of shallow-water sediments ogg San Diego: Journal of the Acoustical Society of America, v. 28, p. 1-15.

Ioannidis, M.A., M.J. Kwiecien and I. Chatzis, 1996, Statistical analysis of the porous microstructure as a method for estimating reservoir permeability: Journal of Petroleum Science and Engineering, v.16, p.251-261.

Japsen, P., C. Hoier, K. B. Rasmussen, I.L. Fabricius, G. Mavko, and J.M. Pedersen, 2002, Effect of fluid substitution on ultrasonic velocities in chalk plugs, South Arne Field, North Sea: 72nd Annual International Meeting SEG, Expanded Abstracts, v.21, p.1881-1884.

Katz, A.J. and A.H. Thompson, 1985, Fractal Sandstone Pores: Implications for Conductivity and Pore Formation: Physical Review Letters, v.54, p.1325-1328.

Keehm, Y., 2003, Computational rock physics; transport properties in porous media and applications: Doctoral Dissertation thesis, Stanford University, Stanford, CA, United States (USA).

Kenter, J.A.M., B.W. Foucke, and M. Reinders., 1997, Effects of differential cementation on the sonic velocities of upper Cretaceous skeletal grainstones (Southeastern Netherlands). Journal of Sedimentary Research, v.67, p.178-185.

Kenter, J.A.M., M. Ivanov, E.L. Winterer, W.W. Sager, J.V. Firth, H.M. Arnaud, P.E. Baker, F. Baudin, T.J. Bralower, P.R. Castillo, P.A. Cooper, P.G. Flood, X. Golovchenko, Y. Iryu, M.K. Ivanov, H.C. Jenkyns, J.A.M. Kenter, I.O. Murdmaa, J. Mutterlose, Y. Nogi, C.K. Paull, E.L. Polgreen, U. Roehl, W.V. Sliter, A. Strasser, N.H.M. Swinburne, J.A. Tarduno, and R.J. van Waasbergen, 1995, Parameters controlling acoustic properties of carbonate and volcaniclastic sediments at sites 866 and 869, in E.L. Winterer, ed., Proc., scientific results, ODP, Leg 143, northwest Pacific atolls and guyots, ODP, Texas A&M University, College Station, p.287-303.

Khazanehdari, J. and J. Sothcott, 2003, Variation in dynamic elastic shear modulus of sandstone upon fluid saturation and substitution: Geophysics, v.68, p.472-481.

Kumar, M. and D.-h. Han, 2005, Pore shape effect on elastic properties of carbonate rocks: SEG Technical Program Expanded Abstracts, p.1477-1480.

Kuster, G. T. and M. N. Toksoz, 1974, Velocity and attenuation of seismic waves in two-phase media; Part I, Theoretical formulations: Geophysics, v.39, p.587-606.

Lønøy, A., 2006, Making sense of carbonate pore system: AAPG Bulletin, v.90, p.1381-1405.

Lucia, F. J., 1983, Petrophysical parameters estimated from visual descriptions of carbonate rocks; a field classification of carbonate pore space: JPT. Journal of Petroleum Technology, v.35, p.629-637.

Lucia, F.J., 1995, Rock-Fabric/Petrophysical classification of carbonate pore space for reservoir characterization: AAPG Bulletin, v.79, p.1275-1300.

Lucia, F.J., 1999, Carbonate Reservoir Characterization: Springer-Verlag, Berlin, Heidelberg, New York.

Marion, D., and D. Jizba, 1997, Acoustic properties of carbonate rocks: use of quantitative interpretation of sonic and seismic measurements. In: I. Palaz and K. J. Marfurt, eds., Carbonate seismology: SEG, p.75-93.

Mavko, G. and Mukerji, T. 1995, Seismic pore space compressibility and Gassmann's relation: Geophysics, v.60, p.1743-1749.

Mavko, G., 2002, Seismic fluid detection, reservoir delineation, and monitoring: The rock physics basis: 72nd Annual International Meeting SEG, short course.

Mavko, G. and D. Jizba, 1991, Estimating grain-scale fluid effects on velocity dispersion in rocks: Geophysics, v.56, p.1940-1949.

Mavko, G. and T. Mukerji, 1998, Bounds on low-frequency seismic velocities in partially saturated rocks: Geophysics, v.63, p.918.

Melim, L.A., F.S. Anselmetti, and G.P. Eberli, 2001, The importance of pore type on permeability of Neogene carbonates, Great Bahama Bank. In: R.N.G. Ginsburg, ed., Ground truthing seismic stratigraphy of a prograding carbonate platform margin, Neogene, Great Bahama Bank—integrated analysis of sedimentology, stratigraphy, diagenesis and petrophysics: SEPM Concepts in Sedimentology and Paleontology.

Morrow, C.A., D.E. Moore, and D.A. Locker, 2000, The effect of mineral bond strength and absorbed water on fault gouge frictional strength: Geophysical Research Letters, v.27, p.815-818.

Movers, T.T. and D.A. Budd, 1996, Quantification of porosity and permeability reduction due to calcite cementation using computer-assisted petrographic image analysis techniques: AAPG Bulletin, v.80, p.309-322.

Mukerji, T., J. Berryman, G. Mavko, and P. Berge, 1995, Differential Effective Medium Modeling of Rock Elastic Moduli with Critical Porosity Constraints: Geophysical Research Letters, v.22, p.555-558.

Murphy, W.F., K.W. Winkler, and R.L. Kleinberg, 1984, Frame modulus reduction in sedimentary rocks: the effect of adsorption on grain contacts: Geophysical Research Letters, v.11, p.805-808.

Murphy, W.F., K.W. Winkler, and R.L. Kleinberg, 1986, Acoustic relaxation in sedimentary rocks: Dependence on grain contacts and fluid saturation: Geophysics, v.51, p.757-766.

Nelson, P.H., 1994, Permeability/porosity relationships in sedimentary rocks: Log Analyst, v.35, p.38–62.

Nolen-Hoeksema, R.C., Z. Wang, J.M. Harris, and R.T. Langan, 1995, High-resolution crosswell imaging of a west Texas carbonate reservoir: Part 5 – Core analysis: Geophysics, v.60, p.712-726.

Pickett, G.R., 1963, Acoustic character logs and their applications in formation evaluation: Journal of Petroleum Technology, p.659-667.

Pittman, E.D. 1971, Microporosity in carbonate rocks: AAPG Bulletin, v.55, p.1873-1881.

Rafavich, F., C.H.S.C. Kendall, and T.P. Todd, 1984, The relationship between acoustic properties and the petrographic character of carbonate rocks: Geophysics, v.49, p.1622-1636.

Rasolofosaon, P. and B. Zinszner, 2003, Petroacoustic characterization of reservoir rocks for seismic monitoring studies: Oil and Gas Science and Technology – Review IFP, v.58, p.615-635.

Risnes, R. and O. Flaageng, 1999, Sub-critical crack-growth in geological materials: Oil & Gas Science and Technology – Review IFP, v.54, p.751-758.

Rossebø, Ø.H., I. Brevik, G.R. Ahmadi, and L. Adam, 2005, Modeling of acoustic properties in carbonate rocks: SEG Technical Program Expanded Abstracts, p.1505-1508.

Saleh, A. A. and J. P. Castagna, 2004, Revisiting the Wyllie time average equation in the case of near-spherical pores: Geophysics, v.69, p.45-55.

Schlueter, E.M., R.W. Zimmerman, P.A. Witherspoon, N.G.W. Cook, 1997, The fractal dimension of pores in sedimentary rocks and its influence on permeability: Engineering Geology, v.48, p.199-215.

Schlumberger, 1972, Log interpretation – principles, New York, Schlumberger Limited, v.1, 113 p.

Schlumberger, 1974, Log interpretation - applications: New York, Schlumberger Limited, v. 2, 116 p.

Solymar, M. and I.L. Fabricius, 1999, Image analysis and estimation of porosity and permeability of Arnager Greensand, Upper Cretaceous, Denmark: Physics and Chemistry of the Earth, Part A: Solid Earth and Geodesy, v.24, p.587-591.

Sun, Y.F., K. Berteussen, S. Vega, G.P. Eberli, G.T. Baechle, R.J. Weger, J.L. Massaferro, G.L. Bracco Gartner and P.D. Wagner, 2006, Effects of pore structure on 4D seismic signals in carbonate reservoirs, SEG, Expanded Abstracts, v.25, p.3260-3264.

Sun, Y.F., 2004, Pore structure effects on elastic wave propagation in rocks: AVO modelling: Journal of Geophysics and Engineering, v.1, p.268.

Sun, Y.F., J.-L. Massaferro, G. P. Eberli, and C. Teng, 2001, Quantifying the Effects of Pore Structure and Fluid Saturation on Acoustic Wave Velocity in Carbonates: Theoretical and Computational Acoustics, p.335-347.

Tsuneyama, F., I. Takahasi, A. Nishida, and H. Okamura, 2003, VP/VS ratio as a rock frame indicator for a carbonate reservoir: First Break, v.21, p.22-27.

Tutuncu, A.N. and M.M. Sharma, 1992, The influence of fluids on grain contact stiffness and frame moduli in sedimentary rocks: Geophysics, v.57, p.1571-1582.

Vajdova, V., P. Baud, and T.-f. Wong, 2004, Compaction, dilatancy, and failure in porous carbonate rocks: Journal of Geophysical Research, v.109, p.B05204.

Van der Berg, E.H., A.G.C.A. Meesters, J.A.M. Kenter, and W. Schlager, 2002, Automated separation of touching grains in digital images of thin sections: Computers & Geosciences, v.28, p.179-190.

Walsh, J.B., Brace, W.F.V., and England, A.W., 1965, Effect of porosity on compressibility of glass: Journal of American Ceramic Society, p.605-608.

Wang, Z., 1991, Fundamentals of seismic rock physics: Geophysics, v.66, p.398-412.

Wang, Z., 1997, Seismic properties of carbonate rocks. In: I. Palaz and K. J. Marfurt, eds., Carbonate seismology: SEG, p.29-52.

Wang, Z., 2000, The Gassmann equation revisited: Comparing laboratory data with Gassmann's prediction, in Z. Wang and A. Nur, eds., Seismic and acoustic velocities in reservoir rocks, v 3, Recent developments: SEG, p.8-23.

Wang, Z., 2001, Fundamentals of seismic rock physics: Geophysics, v.66, p.398-412.

Wang, Z., 2002, Seismic anisotropy in sedimentary rocks, part 2: Laboratory data: Geophysics, v.67, p.1423-1440.

Weger, R., 2007, Quantitative pore/rock type parameters in carbonates and their relation to velocity deviation in carbonates. In: Department of Geology and Geophysics, p.232, University of Miami.

Weger, R.J., G.T. Baechle, J.L. Massaferro, and G.P. Eberli, 2004, Effects of pore structure on sonic velocity in carbonates: SEG Technical Program Expanded Abstracts, v.23, p.1774-1777.

Weger, R.J., G.P. Eberli, G.T.Baechle, and J.L. Massaferro, in press, Quantification of pore structure and its effect on sonic velocity and permeability in Carbonates: AAPG Bulletin.

Winkler, K.W., 1986, Estimates of velocity dispersion between seismic and ultrasonic frequencies: Geophysics, v.51, p.183-189.

Winkler, K.W., and W.F. Murphy, 1995, Acoustic velocity and attenuation in porous rocks, in T.J. Ahrens, ed., Rock physics & phase relations: A Handbook of Physical Constants, AGU Reference Shelf 3.

Wulff, A.M. and H. Burkhardt, 1997, Mechanisms affecting ultrasonic wave propagation in fluid-containing sandstones under high hydrostatic pressure: Journal of Geophysical Research – Solid Earth, v.102, p.3043-3050.

Wyllie, M.R.J., A.R. Gregory, and G.H.F. Gardner, 1958, An experimental investigation of factors affecting elastic wave velocities in porous media: Geophysics, v.23, p.459-493.

Wyllie, M.R.J., A.R. Gregory, and L.W. Gardner, 1956, Elastic wave velocities in heterogeneous and porous media: Geophysics, v.21, p.41-70.

Wyllie, M.R.J., G.H.F. Gardner, and A.R. Gregory, 1963, Discussion: Addendum to 'Studies of elastic wave attenuation in porous media' by M.R J. Wyllie, G.H.F. Gardner, and A.R. Gregory (Geophysics, 1962, 569-589): Geophysics, v.28, p.1074.

Xavier J., 2002, Architecture and seismic expression of Miocene carbonate barrier-lagoon systems (Ermenek Platform, Turkey and Zhujiang Platform, South China Sea): Ph.D. Geology, University of Miami, Coral Gables, Florida.

Zhu, W. and T. F. Wong, 1997, Shear-enhanced compaction in sandstone under nominally dry and water-saturated conditions: International Journal of Rock Mechanics and Mining Sciences & Geomechanics Abstracts, p.372.

Zimmerman, R.W., W.H. Somerton, and M.S. King (1986), Compressibility of Porous Rocks: Journal of Geophysical Research, 91(B12), 12,765–12,777.

Zimmerman, R.W., 1991, Compressibility of sandstones: New York, Elsevier, 173 p.